

MSc thesis in Applied Earth Sciences

# Modelling of Polymer Flooding based on Operator-Based Linearization Approach

**Jinjie Mao**

**2021**

# Modelling of Polymer Flooding Based on Operator-Based Linearization Approach

by

Jinjie Mao

to obtain the degree of Master of Science

at the Delft University of Technology,

to be defended publicly on Tuesday July 27, 2021 at 11:00 AM.

Student number: 5126789  
Project duration: November 17, 2020 – July 27, 2021  
Thesis Supervisors: Dr. Denis V Voskov, TU Delft  
Xiaocong Lyu, MSc., TU Delft  
Thesis committee: Prof. Dr. Ir. P. L. J. Zitha, TU Delft  
Dr. P. E. Boukany, TU Delft  
Dr. Mohsen Mirzaie Yegane TU Delft

An electronic version of this thesis is available at <http://repository.tudelft.nl/>.

*Science is not only compatible with spirituality;  
it is a profound source of spirituality.*

Carl Sagan

# CONTENTS

<b>List of Figures</b>	<b>v</b>
<b>List of Tables</b>	<b>xi</b>
<b>Abstract</b>	<b>xii</b>
<b>Acknowledgements</b>	<b>xiii</b>
<b>1 Introduction</b>	<b>1</b>
1.1 Research Motivation and Background . . . . .	1
1.2 Research Aims and Chapter Outline . . . . .	2
<b>2 Literature Review</b>	<b>4</b>
2.1 Polymer Flooding in EOR Applications. . . . .	4
2.1.1 Displacement Mechanism of Polymer Flooding . . . . .	4
2.1.2 Field Application of Polymer Flooding . . . . .	5
2.2 Numerical Simulation of Polymer Flooding . . . . .	6
2.3 Polymer Chemistry . . . . .	8
2.3.1 Polymer Types. . . . .	8
2.3.2 Property Comparison Between HPAM and Xanthan. . . . .	10
2.4 Polymer Rheology in porous media . . . . .	11
2.4.1 Flow Behaviour of Non-Newtonian Fluid . . . . .	11
2.4.2 Bulk Rheology of HPAM . . . . .	12
2.4.3 Effective Shear Rate . . . . .	13
2.4.4 Zero-shear Viscosity (First Stage) . . . . .	14
2.4.5 Shear-thinning Model (Second stage) . . . . .	20
2.4.6 Shear-thickening Model (Third stage) . . . . .	21
2.4.7 Integrated Viscosity Model Combining Three Stages . . . . .	23
2.5 Polymer Retention in Porous Media . . . . .	23
2.5.1 Retention Mechanism . . . . .	23
2.5.2 Adsorption of HPAM. . . . .	26
2.5.3 Types of Isotherm Absorption and Calculation of Polymer Retention . . . . .	27
2.5.4 Effect of Polymer Retention on Porosity . . . . .	29
2.5.5 Effect of Polymer Retention on Permeability . . . . .	30

<b>3</b>	<b>Methodology</b>	<b>33</b>
3.1	DARTS Simulator . . . . .	33
3.2	Basic Conservation Equations . . . . .	34
3.3	Operator-Based Linearization approach . . . . .	36
3.4	Mathematical Description of Polymer Recovery Mechanism . . . . .	37
3.4.1	Polymer Module. . . . .	37
3.4.2	Fluid & Rock Properties . . . . .	42
3.4.3	Well Module . . . . .	44
<b>4</b>	<b>Results</b>	<b>45</b>
4.1	Two-phase Flow in Tertiary System . . . . .	45
4.2	Shear-thinning. . . . .	46
4.2.1	Effect of Injected Polymer Concentration . . . . .	47
4.2.2	Effect of Plugging Location . . . . .	48
4.2.3	Effect of Time Duration . . . . .	49
4.3	Polymer retention. . . . .	50
4.3.1	Effect of Injected Polymer Concentration . . . . .	50
4.3.2	Effect of Time Duration . . . . .	53
4.3.3	Effect of Upper Bound of Polymer Retention. . . . .	53
<b>5</b>	<b>Validation</b>	<b>56</b>
5.1	Validation with UTCHEM Results . . . . .	56
5.1.1	Comparison of DARTS and UTCHEM . . . . .	56
5.1.2	Validation of HPAM Rheology Model in Porous Media . . . . .	58
5.2	Validation with Buckley-Leverett Solution . . . . .	60
<b>6</b>	<b>Coreflood Simulation</b>	<b>64</b>
6.1	3D CT Coreflood and reservoir construction . . . . .	64
6.2	Modelling of Two-Phase Flow in Tertiary System. . . . .	66
6.3	The Effect of Injected Polymer Concentration on Porosity . . . . .	67
<b>7</b>	<b>Conclusion and Recommendations</b>	<b>69</b>
7.1	Conclusion. . . . .	69
7.2	Recommendation . . . . .	70
	<b>Bibliography</b>	<b>71</b>

# LIST OF FIGURES

1.1	Technical Roadmap . . . . .	2
2.1	Mobility control: (a) Sweeping surface by waterflooding with unfavourable mobility ratio ( $M > 1$ ); (b) Polymer augmented sweeping efficiency with favourable mobility ratio ( $M \leq 1$ ) [1]. . . . .	5
2.2	The comparison with respect to simulator performance between UTCHEM, STARS and ECLIPSE. . . . .	8
2.3	The comparison with respect to physics database between UTCHEM, STARS and ECLIPSE [2]. . . . .	8
2.4	Molecular structure of: (a) polyacrylamide; (b) partially hydrolysed polyacrylamide	9
2.5	Multiple classifications of non-Newtonian fluids and Newtonian fluids . . . . .	11
2.6	Schematic fluids behaviour of shear stress (left) and viscosity (right) as a function of shear rate . . . . .	12
2.7	Illustrations of HPAM relative viscosity changing with shear rate under the effect different polymer concentrations [3] . . . . .	13
2.8	Schematic illustration of the three stages of viscoelastic fluid flow in porous media [3] . . . . .	13
2.9	(a) Shear viscosity of polymer 3330S at different concentrations (1% NaCl at 25°C); (b) Shear viscosity of polymer 3330S at different salinity (2000 ppm at 25°C); (c) Shear viscosity of polymer 3330S at different hardness (2000 ppm in 1% NaCl at 25°C); (d) Shear viscosity of polymer 3330S at different temperature (2000 ppm in 1% NaCl) [4] . . . . .	16
2.10	Viscosity measurements of polymer melts taken from plate-plate rheometry used in rotary jet spinning (RJS). Four scenarios from high Mw to low Mw of polyethylene has been set up from top to bottom [5] . . . . .	18
2.11	Regression model of viscosity-shear rate relationship by Carreau-Yasuda (www.anton-paar.com) [6] . . . . .	21

2.12	Retention mechanisms in porous media [7] . . . . .	24
2.13	The schematic diagram of mechanical entrapment . . . . .	25
2.14	Types of adsorption isotherms in solid-dilute solutions system. . . . .	27
2.15	Typical shapes of Langmuir isotherm curves [8] . . . . .	28
2.16	Porosity reduction process due to polymer adsorption. The domain consists of three distinct regions with the volume changing through the adsorption, particularly the fluid volume ( $V_f$ ) which is occupies by all the mobile phases (aqueous and oleic phase in the case of two phase flow), the reactive volume ( $V_r$ ) which consist of solid phases that can adsorb, and finally the nonreactive volume ( $V_{nr}$ ). . . . .	29
2.17	Ideal breakout curves in different conditions. . . . .	30
2.18	The plot of permeability reduction factor versus adsorbed polymer concentration. . . . .	32
3.1	A outline of the OBL approach for a single time step is provided. The colored steps were newly implemented for this study. . . . .	34
3.2	Flow chart of viscosity calculation. . . . .	38
4.1	The molar fraction profiles of polymer (in green), oil (in red) and water (in blue) are plotted after 400 days and at different injected polymer concentration. The first, second and third row are at concentration of $1e^{-5}$ mol/mol, $1e^{-7}$ mol/mol and $1e^{-12}$ mol/mol. . . . .	46
4.2	The propagation of oil molar fraction (the left) and water molar fraction (the right) in binary system after 400 days. . . . .	47
4.3	Polymer concentration throughout the porous media after 400 days when a polymer with a concentration of 1664 ppm ( $1e^{-8}$ mol/mol) is introduced. . . . .	48
4.4	The zero-shear viscosity (in blue) and apparent viscosity (in red) of polymer solution after 400 days is plotted in the first row. The viscosity reduction factor and viscosity multiplier are plotted in the second and the third row respectively with the polymer being injected at the injection well. Different injected polymer concentration of a) 16441 ppm ( $1e^{-7}$ mol/mol), b) 1664 ppm ( $1e^{-8}$ mol/mol), and c)166.4 ppm ( $1e^{-9}$ mol/mol) serves as the only variable. . . . .	49

- 4.5 The zero-shear viscosity (in blue) and apparent viscosity (in red) of polymer solution after 400 days is plotted in the first row and the corresponding viscosity reduction factor and viscosity multiplier are plotted in the second and the third row respectively at injected polymer concentration of 1664 ppm ( $1e^{-8}$  mol/mol). Different plugging treatment is controlled as the only variable, which is injecting in the a) middle point (250m), b) one ten-meter-long section (250-300m), and c) two ten-meter-long section (250-300m and 350-400m). . . . . 50
- 4.6 The zero-shear viscosity (in blue) and apparent viscosity (in red) of polymer solution is plotted in the first row and the corresponding viscosity reduction factor and viscosity multiplier are plotted in the second and the third row respectively at injected polymer concentration of 1664 ppm ( $1e^{-8}$  mol/mol). Hereby plugging along a ten-meter-long section (250-300m) is selected as an sample. The only variable initiated is the timespan, lasting for a) 400 days, b) 600 days, and c) 800 days. . . . . 51
- 4.7 Polymer concentration and adsorbed polymer concentration versus distance after 400 days when a polymer with a concentration of a) 1664 ppm ( $1e^{-8}$  mol/mol), b) 16.6 ppm ( $1e^{-10}$  mol/mol), and c) 1.66 ppm ( $1e^{-12}$  mol/mol) is introduced. The upper bound of polymer retention is set to be 10, with a and b set to be 50 and 5, respectively. . . . . 52
- 4.8 The porosity after adsorption (in blue) and original porosity (in red) in compressible porous media after 400 days is plotted in the first row. The porosity reduction factor is plotted in the second row with the polymer being injected at the injection well. The upper bound of polymer retention is set to be 10, with a and b set to be 50 and 5, respectively. Different injected polymer concentration of a) 1664 ppm ( $1e^{-8}$  mol/mol), b) 16.6 ppm ( $1e^{-10}$  mol/mol), and c) 1.66 ppm ( $1e^{-12}$  mol/mol) serves as the only variable. . . . . 52
- 4.9 The porosity after adsorption (in blue) and original porosity (in red) in compressible porous media is plotted in the first row. The porosity reduction factor is plotted in the second row with the polymer being injected at the injection well at a concentration of 1664ppm ( $1e^{-8}$ mol/mol). The upper bound of polymer retention is set to be 10, with a and b set to be 50 and 5, respectively. A time period of a) 400 days, b) 600 days, and c) 800 days are only variable initiated. . . . . 54

- 4.10 The porosity after adsorption (in blue) and original porosity (in red) in compressible porous media after 400 days is plotted in the first row. The corresponding porosity reduction factor is plotted in the second row with the polymer being injected at the injection well at a concentration of 1664ppm ( $1e^{-8}$ mol/mol). The upper bound of polymer retention is adjusted under a constant  $b$  but a varying  $a$ , achieved by three groups of parameters, which is a)  $a = 5, b = 5$ ; b)  $a = 50, b = 5$ ; c)  $a = 500, b = 5$ . . . . . 55
- 4.11 The porosity after adsorption (in blue) and original porosity (in red) in compressible porous media after 400 days is plotted in the first row. The corresponding porosity reduction factor is plotted in the second row with the polymer being injected at the injection well at a concentration of 16.6ppm ( $1e^{-10}$ mol/mol). The upper bound of polymer retention remains invariable but the values of  $a$  and  $b$  change simultaneously, which can be accomplished by three sets of parameters, i.e. a)  $a = 0.01, b = 0.0001$ ; b)  $a = 1, b = 0.01$ ; c)  $a = 100, b = 1$ . . . . . 55
- 5.1 Analytical solution and numerical solution of HPAM rheology in porous media at different concentrations of 167ppm, 1667ppm and 3330ppm. The continuous curves present the unified analytical model while the discretised points present the numerical results implemented by DARTS. The two blocks in light blue, yellow and red mark the three intervals of shear rates when the pressure at injection well is 230bar, 300bar and 500bar respectively. . . . . 59
- 5.2 Analytical solution and numerical solution of HPAM rheology in porous media affected by different concentrations of 167ppm, 1667ppm and 3330ppm. The continuous curves present the unified analytical model while the discretised points present the numerical results implemented by DARTS. The three intervals of shear rates when the pressure at injection well is 215bar, 230bar and 300bar respectively. 60
- 5.3 Analytical solution and numerical solution of HPAM rheology in porous media affected by different salinity of 0.1wt%, 1wt%, 2wt% and 4wt%. The continuous curves present the unified analytical model while the discretised points present the numerical results implemented by DARTS. The three intervals of shear rates when the pressure at injection well is 215bar, 230bar and 300bar respectively. . . . . 60

- 5.4 (a) Comparison of water front by water flooding and polymer flooding. (b) Construction of water front during polymer flooding. Hereby  $S_{wwf}$  and  $f_{wwf}$  are the water saturation and fractional flow at the shock of water flooding,  $S_{wpf}$  and  $f_{wpf}$  are the water saturation and fractional flow at the shock of polymer flooding and  $S_{wOB}$  and  $f_{wOB}$  are the water saturation and fractional flow in the oil bank. . . . . 61
- 5.5 Analytical water saturation profile at  $t_d = 0.33PV$  during polymer flooding (in red) and water flooding (in blue). Where,  $x_{DOBb}$  and  $x_{DObf}$  are named to differentiate the transporting distance at the back and front of the oil bank. . . . . 62
- 5.6 Comparison of (a) analytical water saturation profile and (b) numerical water saturation profile by DARTS at  $t_d = 0.33PV$  and the numerical solution is obtained at 400 days in a 500m-length 1D reservoir ( $dt=5days$ ,  $dx=0.1$ ) during water flooding (in blue) and polymer flooding (in red). . . . . 63
- 5.7 Comparison of (a) analytical water saturation profile and (b) numerical water saturation profile by DARTS. The analytical solution is obtained at  $t_d = 0.33pv$  and the numerical solution is obtained at 400 days in a 500m-length 1D reservoir ( $dt=1days$ ,  $dx=1$ ) during water flooding (in blue) and polymer flooding (in red). . . 63
- 6.1 Porosity profile of Bentheimer sandstone at a slice and along the core a) before coarsening and b) after coarsening. . . . . 65
- 6.2 The molar fraction of polymer when injecting a)  $1 \times 10^{-8} \text{mol/mol}$  (1667ppm) and b) no polymer at  $3 \times 10^{-5}$  days. . . . . 66
- 6.3 The molar fraction of water when injecting a)  $1 \times 10^{-8} \text{mol/mol}$  (1667ppm) and b) no polymer at  $3 \times 10^{-5}$  days. . . . . 66
- 6.4 The molar fraction of oil when injecting a)  $1 \times 10^{-8} \text{mol/mol}$  (1667ppm) and b) no polymer at  $3 \times 10^{-5}$  days. . . . . 66
- 6.5 The porosity reduction factor distribution at injected polymer concentration of 1664 ppm ( $1 \times 10^{-8} \text{mol/mol}$ ) serves as the only variable. Hereby the upper bound of polymer retention is set to be 1, with a and b both set to be 5. . . . . 67
- 6.6 The porosity reduction factor distribution at injected polymer concentration of 16.6 ppm ( $1 \times 10^{-10} \text{mol/mol}$ ) serves as the only variable. Hereby the upper bound of polymer retention is set to be 1, with a and b both set to be 5. . . . . 67

- 6.7 The porosity reduction factor distribution at injected polymer concentration of 1.66 ppm ( $1 \times 10^{-12}$  mol/mol) serves as the only variable. Hereby the upper bound of polymer retention is set to be 1, with a and b both set to be 5. . . . . 67

# LIST OF TABLES

2.1	Property comparison between HPAM and xanthan . . . . .	10
2.2	Conceptual mathematical models of effective shear rate . . . . .	15
3.1	Extensions of Operator-Based Linearization adapted to polymer flooding. . . . .	41
5.1	Simulation settings for HPAM rheology validation . . . . .	57
5.2	Pros and cons of DARTS and UTCHEM algorithm. . . . .	57
5.3	Simulation settings for HPAM rheology validation. . . . .	58
5.4	Corey model parameters for water–oil two-phase relative permeability in the presence and absence of polymer. . . . .	61
6.1	Core and experimental fluid properties for experiment . . . . .	64

# ABSTRACT

In this study, we introduce the Delft Advanced Research Terra Simulator (DARTS), which employs the Operator-Based Linearization (OBL) approach to provide efficient and precise solutions for non-linear discretized equations, to simulate the polymer flooding process. This compositional simulation framework is feasible for describing complex physical phenomenon with high nonlinearity because detached functional operators have been developed to release the calculation load while maintaining a high degree of stability and accuracy. The main contributions and innovations are shown below:

1. A two-phase and three-component chemical flooding mathematical model with some reasonable assumptions was developed to investigate the enhanced-oil-recovery (EOR) mechanism of polymer flooding. A finite volume discretization scheme and a fully implicit method (FIM) are implemented to approximate the conservation equations. The OBL approach is used to reduce the complexity of the simulation framework. The correctness of the model is verified by comparison with analytical model.
2. In addition to shear thinning effect, polymer viscoelasticity has also been taken into account. This mathematical model is able to handle high shear rates during field displacement as well as low to medium shear rates in laboratory experiments.
3. A new model for porosity reduction caused by polymer adsorption is formulated. The effect of polymer concentration on the effective pore volume is incorporated in numerical simulations based on Langmuir adsorption model.

# ACKNOWLEDGEMENTS

I have eternal gratitude to Dr. Denis Voskov, my thesis supervisor, for igniting my desire to in-depth investigate numerical simulation and scheming a fascinating project that pointed to my original intention. I also appreciate him for inspiring the progress and controlling the rhythm of research which makes the whole journey intense and full of harvest. And I would feel grateful to Xiaocong Lyu, for his patience to my unmaturred thoughts and valuable instruction on technical support. I would like to thank him for spending time to inspect the physics-related mathematical equations and revise the text in the course of writing, which was essential to the completion of both the model and the thesis.

I am greatly indebted to Prof. Zitha and Dr. Mohsen Mirzaie Yegane for their insightful and cut-edge knowledge background in terms of polymer flooding. Their encouraging comments provide multiple perspectives to me and inspire me to incorporate and deal with the polymer physics more comprehensively.

I also thank my parents: Jing Tian and Hongbing Mao for their unselfish love and support over the ocean. I also would like to express the thankfulness to my kind friends whose names I can't list here one by one. Without your accompany and warm concern, these two years would be gloomy and dry as dust.

Last but not the least, I hope this paper will not be the terminal station of the academic thinking of numerical simulation with respect of reservoir modeling, which I am zealous with and willing to dedicate to in my future career.

*Jinjie Mao*  
*Delft, July 2021*

# 1

## INTRODUCTION

### 1.1. RESEARCH MOTIVATION AND BACKGROUND

**N**OWADAYS, most oilfields in the world have entered the late stage of development, with water cut rising rapidly and reaching over 80%. Only applying the secondary water injection during the production process will lead to great difficulty towards the recovery factor improvement for the petroleum fields in the declining phase as less than half of the original oil in place is recovered due to capillary trapping and reservoir heterogeneity. Subsequently, enhanced oil recovery (EOR) processes are required to recover the residual oil. Tertiary oil recovery replaces the exploitation of water-drive oil fields, greatly improving the recovery rate of old oil fields and the utilization rate of proven complex hydrocarbon resources and satisfying the needs of national economic development and oil security. In the past decade, chemical flooding (alkali/surfactant/polymer) has emerged and become one of the most attractive methods that can greatly increase oil recovery by 5% to 15% [9].

Numerical simulation, as the link between experimental research and field practice, achieve visualization and prediction of compositional flow in the porous media based on the chemical flooding mechanism and related physical and chemical changes. However, the polymer flooding increases the costs of oil recovery [10]. Fortunately, the required volumes of macromolecule is small because of the high molar weight, which allows relatively low cost spent on the recovery despite of the high advanced prices of polymer. Also there is actual field practice in Daqing being

a corroboration [11]. The economic datasheet indicates that to achieve a increment of recovery rate of 12% OOIP - original oil in place), the total cost (including depreciation) per bbl of oil displaced by polymer solution is lower than pure water flooding. In order to maximize the economic benefits of polymer flooding, it is necessary to quantitatively analyse the extent of enhanced oil recovery and the required amount of polymer. Herein, numerical simulation could exactly act as the solver of this problem, which is a final target for our research. The oil and gas are moving in complex patterns driven by heterogeneity of the porous media and the addition of multiple chemical agents increases this complexity. At present, the black oil model is relatively mature, whilst chemical flooding has poor maturity and reliability due to complicated displacement mechanisms with a variety of physical and chemical interactions. Therefore, with the popularization and application of chemical flooding technology throughout the world, it is urgent to carry out research on numerical simulation of polymer flooding.

## 1.2. RESEARCH AIMS AND CHAPTER OUTLINE

The research objective is to construct an efficient model for polymer flooding, which requires a realistic reflection of the complicated physical behaviour of polymer in porous media, including the rheology and retention phenomenon exclusive for high-molecular compounds. A schematic representation of the most important research phases is shown in Fig. 1.1.

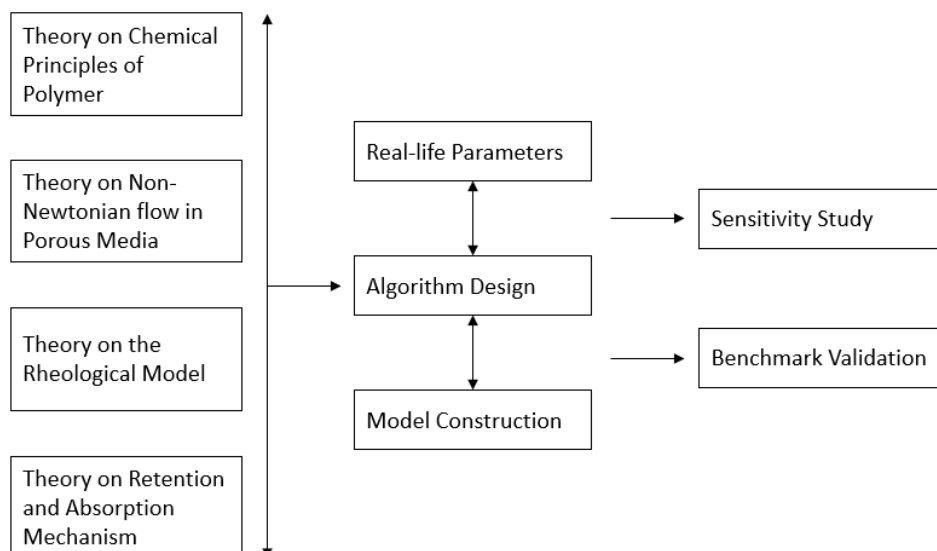


Figure 1.1: Technical Roadmap

In Chapter 2, polymer flooding is introduced in terms of the polymer chemistry and properties, current status of chemical flooding simulators and detailed background related to the polymer

rheology (i.e. pseudoplasticity and viscoelasticity) and retention.

Chapter 3 discusses an application of Delft Advanced Research Terra Simulator (DARTS) framework in this study. The modeling details are described, including system of equations for polymer mass balance, polymer rheology and retention models for fluid flow in porous media, and the fluid, rock and well modules set up in DARTS.

In Chapter 4, a sensitivity study to injected polymer concentration, time span and parameters configuration has been provided. The level of importance of various factors has been investigated in details.

In Chapter 5, model validation is provided by comparing simulation results with the analytical solutions.

In Chapter 6, precise influence brought by polymer is illustrated by running a core flooding simulation. Hereby a more realistic answer can be given as a dual verification for our numerical model.

Chapter 7 summarizes the main conclusions of the study.

# 2

## LITERATURE REVIEW

### 2.1. POLYMER FLOODING IN EOR APPLICATIONS

IN the history of enhanced oil recovery rate, polymer flooding has the second most widespread occurrence only ranking behind waterflooding. This technology effectively improves the mobility ratio, expands the swept volume, and is able to drag and carry the residual oil droplets left in the blind ends of microscopic-scale pores. The following dense research of stabilizing and upgrading water-soluble polymer presents an exponential growing trend, which brings a fruitful and promising prospect.

#### 2.1.1. DISPLACEMENT MECHANISM OF POLYMER FLOODING

A small amount of the high-molecular-weight polymer being dissolved in floodwater greatly increases the viscosity of the aqueous solution, so that the mobility ratio of the displacing fluid over displaced fluid is relatively small, which is defined as Eq. 2.1.

$$M = \frac{\lambda_{displacing}}{\lambda_{displaced}} = \frac{k_{raq}/\mu_{aq}}{k_{ro}/\mu_o} = \frac{k_{raq}\mu_o}{k_{ro}\mu_{aq}}, \quad (2.1)$$

where  $\lambda_{displacing}$  and  $\lambda_{displaced}$  indicate the mobility of displacing (i.e. aqueous phase) and displaced fluid (i.e. oleic phase) respectively,  $k_{rj}$  is the relative permeability of phase  $j$ , and  $\mu_j$  is the viscosity of phase  $j$ .

The ratio greater than one ( $M > 1$ ) is considered, unfavourable owing to the fingering of water with craggy displacement front, and a favourable mobility ratio is formulated to be no greater than 1 ( $M \leq 1$ ) to reach a stable oil bank and a desirable recovery rate [12]. (Fig. 2.1)

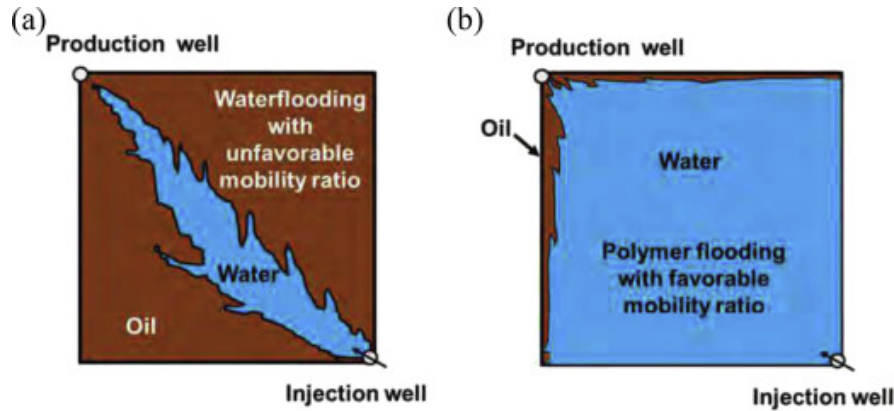


Figure 2.1: Mobility control: (a) Sweeping surface by waterflooding with unfavourable mobility ratio ( $M > 1$ ); (b) Polymer augmented sweeping efficiency with favourable mobility ratio ( $M \leq 1$ ) [1].

From the Fig. 2.1(a), viscous fingering is the main reason for the reduction of the sweep efficiency. When the oil-water front of the high permeability layer reaches the production well, which leads to premature water breakthrough, most of the injected water will pass through ineffectively and fail to enter the rest of the low-permeability zone. Ideal mobility ratio can achieve the effect of expanding the swept volume by increasing the pressure difference of imbibed solution in the porous medium with low-to-medium permeability and porosity. Once the polymer solution entered the target reservoir, the high-permeability zone would be preferred. Due to chemical adsorption and mechanical trapping, it will stay in the high-permeability layer and generate additional seepage resistance. Whereby the injection pressure through the whole well will rise under the condition of keeping the injection rate constant. Thus the purpose of increasing the pressure difference and liquid imbibition of the poor-permeability zone can be realized.

Furthermore, by the virtue of high viscoelasticity, resulting from the long chain structure of polymer, the oil droplets and film will be stretched during the flowing process, whereby the carrying capacity is largely strengthened.

### 2.1.2. FIELD APPLICATION OF POLYMER FLOODING

Applying polymer flooding enables the scope of economically accessible prospects to expand: high-viscosity polymers overcome non-uniform and invalid displacement caused by water fingering, which extends polymer flooding to high permeability and heavy oil reservoirs; polymers

prepared from formation water with low mineralization and low hardness exhibit excellent thermal stability, which extends polymer flooding to high-temperature and high-mineralized reservoirs. The current polymer flooding screening standards state that polymer flooding is applicable in crude oil production with low viscosity (less than 5000mPa·s), API gravity down to 12° and moderate temperature (less than 98.9°C), and in porous medium with extremely severe horizontal and vertical heterogeneity [13].

At present, the focus of research in various countries is on the development of polymers with good water solubility, strong thickening ability, salt tolerance, thermal and shear resistance, stability to biological and chemical factors, low retention, wide availability, and low cost. For example, hydrophobically associating water-soluble polymer (HAWP) with a small amount of 101 hydrophobic groups promoting inter-molecular association resists viscosity loss in saline [14]; cross-linked polymer made of HPAM coupled with aluminium citrate can selectively seal near-well and internal formations by switching between the bulk gel and linked polymer solution (LPS) under different polymer concentration [15].

## 2.2. NUMERICAL SIMULATION OF POLYMER FLOODING

Numerical simulation serves as an important tool that predict the future dynamic characteristics and seek the optimistic way to tap hydrocarbon resources. The most prevailing tertiary oil recovery technologies as polymer flooding is, its indoor experiments and field application is limited. First, a large investment is required in field tests because of expensive chemical agents; second, the addition of polymer results in high risk of groundwater contamination and destruction of ecosystem [16].

Considerable discrepancies exist between experimental research and field application, but can be solved by numerical simulation that bridges them intensely. Based on the reasonable description of displacing mechanism and physical and chemical phenomena, accurate simulation and prediction of the polymer flooding process can be accomplished, thereby minimizing the investment risks while maximizing the economic benefits.

In this day and age, the representative polymer flooding numerical simulators include VIP-POLYMER (Landmark), ECLIPSE100 (Schlumberger), STAR (CMG), ASP (RIPED), UTCHEM (UTA). The following characteristics are drawn from the simulators stated above [17]:

- The amount of involved components increases in the polymer flooding which brings about the need of higher-level discretization of the model and solving more complex non-linear

equations. At present, all the numerical simulation software of polymer flooding run in a much slower speed than conducting water flooding. In large-scale grid calculation, non-convergence or divergence will occur. As a result, the scale of polymer flooding operations is greatly restricted.

- When the number of added components in the polymer flooding is small, the full-implicit method is preferred which can effectively guarantee the stability of the simulation. Whereas in the case of a large number of components, the above-mentioned scheme turns to be difficult. Moreover, certain physical and chemical parameters which cannot be obtained from laboratory study will restrict the practical application of software. Therefore, trade-offs between stability and rationality of the mechanism description have to be faced.
- Numerical simulation software supporting multiple polymers has been developed, but the process of combining different polymers has yet to be verified.
- The theory of viscoelasticity reducing the remaining oil has been proposed, but it hasn't been taken into account by mainstream software. The main difficulty lies in how to incorporate the microscopic viscoelastic theory into the macroscopic grid concept.
- The commonly used numerical models do not consider the issue of non-isothermal polymer degradation. The obstacle is present in how to access to the value of polymer degradation parameters and the development of non-isothermal waterflooding model.
- The improved black oil model is still the leading choice for polymer flooding today. The advantages are simplicity and ease of use, relatively small computational time and less storage space required; the disadvantage is that it cannot express the multi-component mass changes completely caused by interphase exchange and the resulting changes in fluid properties and flowing states.
- The compositional model allows a more accurate description of various physical change and chemical reactions to be reflected in the change of composition. However the computational storage and load are large, which also leads to huge difficulty in implementation.
- The capillary-tube model is effortless, with small storage and computational burden but fails to simulate the effect of gravity, lateral exchange between tubes, etc.
- Finite element model undermines the influence of the unfavourable mobility ratio and the orientation of mesh configuration, with fewer grid nodes, and less storage and calculation demand. However, the PDE function of basic conservation law is complicated, time-consuming, and difficult to apply in the field condition.

Certainly each simulator has their own merits and demerits. Hereby attached the comparison between three most prevailing simulators and their involving physics (see Fig. 2.2 and Fig. 2.3).

	Model Framework	Solving process
<b>UTCHEM(UTA)</b>	3D, multi-phase, multi-component	IMPES
<b>STARS(CMG)</b>	3D, 3-phase, multi-components	AIM (Adaptive Implicit), AIMSOL (adaptive implicit matrix solver)
<b>ECLIPSE</b>	3D, 3-phase, 5-components (limited)	IMPES, FIM, as well as AIM and IMPSAT(implicitly solves the pressure and saturation and explicitly solves the concentration)

Figure 2.2: The comparison with respect to simulator performance between UTCHEM, STARS and ECLIPSE.

Polymer Physics	UTCHEM	CMG-STARS	ECLIPSE
Rheological behavior	☑	☑	☑
Adsorption	☑	☑	☑
Permeability Reduction	☑	☑	☑
Inaccessible Volume	☑	☑	☑
Effect of Polymer Concentration on Rheology	☑	☑	☑
Effect of Salinity on Rheology and Retention	☑	☒	☒
Effect of Hardness on Rheology and Retention	☑	☒	☒

Figure 2.3: The comparison with respect to physics database between UTCHEM, STARS and ECLIPSE [2].

## 2.3. POLYMER CHEMISTRY

### 2.3.1. POLYMER TYPES

#### Partially hydrolysed polyacrylamide (HPAM)

HPAM (partially hydrolysed polyacrylamide) is distinctly hydrophilic and readily dissolves in water to form hydrogen bonds, thus having a strong viscosity-increasing effect. At the same time, electrical repulsion occurs between the anionic carboxyl groups (COO<sup>-</sup>) along the backbone of chains (Fig. 2.4), so that the chains can be fully expanded and large volume of hydrodynamic fluid can be obtained. The flexible chain in the aqueous phase displays in a random coil conformation in the high-temperature and high-salinity solution, which plays a role of increasing viscosity but also easily to decompose into discrete elements in the meantime.

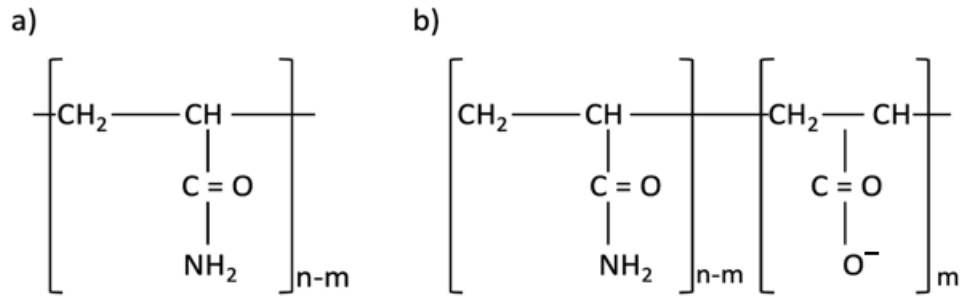


Figure 2.4: Molecular structure of: (a) polyacrylamide; (b) partially hydrolysed polyacrylamide

Both polyacrylamide and HPAM have a variety of positive aspects on resulting high viscosity of water solution, significant control of water-oil mobility ratio, little adsorption loss, as well as insensitivity to bacterial damage. The known shortcomings of HPAM are the poor mechanical shear stability, great viscosity loss in salt brine, ease of degradation while prolonged storage or at a higher temperature and the carboxyl groups prone to react with divalent ions. On top of the drawbacks stated above, it is easy to spark off clay swelling which contributes to serious sand production in long-term application.

Since then, there are two main ways to improve the performance of PAM [18]: add additives that strengthen the stability of PAM, such as formaldehyde, isopropanol, urea, thiourea, amino acids, surfactants, salicylic acid and derivatives, etc., or modify PAM by introducing new monomers on the polymer chain to promote the performance in terms of temperature, salinity and shearing resistance, including 2-acrylamide-2-methylpropane sulfonic acid (AMPS) and N-vinylpyrrolidone (NVP), sulfonated maleic acid, sulfonated styrene, etc. By means of copolymerization and reaction with activating group, cationic copolymers, amphoteric copolymers, hydrophobically associating polymers, etc. can be prepared.

### Xanthan gum

Xanthan gum is a monosporic polysaccharide produced by fermentation of *Pseudoxanthomonas* with a molecular weight of more than 1 million. Xanthan gum, which is a typical biopolymer was implemented in East Coalinga Oilfield in California, USA in 1978 with a big success, and the oil-water mobility ratio was only 1.5 [19]. Xanthan gum has superior performance with respect to suspension, viscosity-thickening and emulsifying, water solubility and pH stability. The molecular chain of xanthan is of greater rigidity than polyacrylamide, which can effectively resist mechanical deterioration and salinity resistance. However it still subjects to great constraints by relatively poor temperature tolerance, limited shear resistance and severe sensitivity to bacteria and oxygen-

enriched environment. In addition to degrading polymers, bacteria and oxides also block the imbibing channels around the injection well which raises the demand of fungicides and oxygen scavengers. It has also been reported that in order to upgrade the fermentation process, stabilizers like isopropanol and thiourea can be added into the xanthan gum solution, which is accomplished by graft copolymerization with sulfomethylated polyacrylamide.

### 2.3.2. PROPERTY COMPARISON BETWEEN HPAM AND XANTHAN

A systematic comparison between aforementioned two polymers has been tabulated in Table. 2.1.

Table 2.1: Property comparison between HPAM and xanthan

	<b>HPAM</b>	<b>Xanthan gum</b>
Rheology	Shear-thinning at low velocity but shear-thickening at moderate-to-high velocity	Shear-thinning at all kinds of velocities
Salt sensitivity	Salt-sensitive and suitable for low-salinity condition	Salt-resistant and exerts influence regardless the salinity level
Thermal stability	maintain good thermal stability until 110°C	Keep stable under the condition of less than 80°C
Degradation resistance	Bad resistance on mechanical shearing effects	More likely to experience biological and chemical degradation but more resistant to mechanical degradation [20]
Cost	Reasonable economic cost [21]	Stable price and higher than polyacrylamide polymer [22]

Although HPAM and xanthan gum have their own merits and demerits, HPAM is more frequently used in the field due to its cost-effective features, ability unaffected by biodegradability and reduced relative permeability [8]. A literature review in 2014 reported that and the projects using HPAM accounts for 92% when taking 72 field implementations of polymer flooding as a sample [23]. This paper gives the first-place attention to perform the study of flow behavior and related physics of HPAM in the reservoir.

## 2.4. POLYMER RHEOLOGY IN POROUS MEDIA

### 2.4.1. FLOW BEHAVIOUR OF NON-NEWTONIAN FLUID

From a wide perspective, two fundamental classifications of fluids have been accepted, which is (1) Newtonian, and (2) non-Newtonian fluids (Fig. 2.5). Newtonian fluids adhere to Newton's law of viscosity and hold invariable viscosity. In the other hand, the viscosity of non-Newtonian fluids does not conform to the Newton's law of viscous resistance and displays variable value.

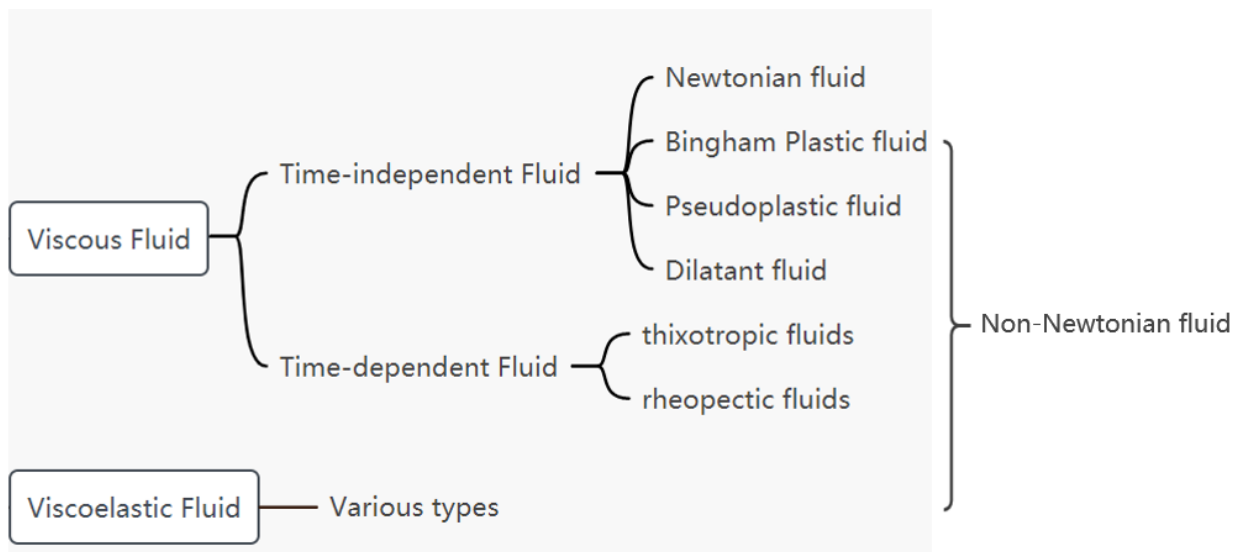


Figure 2.5: Multiple classifications of non-Newtonian fluids and Newtonian fluids

Since the non-Newtonian fluid does not satisfy Newton's law of viscosity, the shear stress and shear rate is not linear-related, but a curve with a inconsistent slope angle. According to the changing trend of the slope with the shear rate, non-Newtonian fluids can be divided into the following types: Bingham fluid, pseudoplastic fluid, dilatant fluid, etc. The rheological curves of shear stress and viscosity versus shear rate are shown in the Fig. 2.6.

Non-Newtonian fluids can be further subdivided into pure viscous fluids and viscoelastic fluids [24], as shown in Fig. 2.5. Among them, the deformation of the pure viscous fluid cannot be restored once the shear stress is removed; on the contrary, the deformation of the viscoelastic material can be partially or completely restored after the shear stress disappears. In the process of non-Newtonian fluid flow, viscous fluids exhibit single-type shear flow, while viscoelasticity reflects in the form of orienting, stretching, diffusion, and degradation of polymer molecular in addition to shear flow, which gives rise to excessive complexity of flow behaviour.

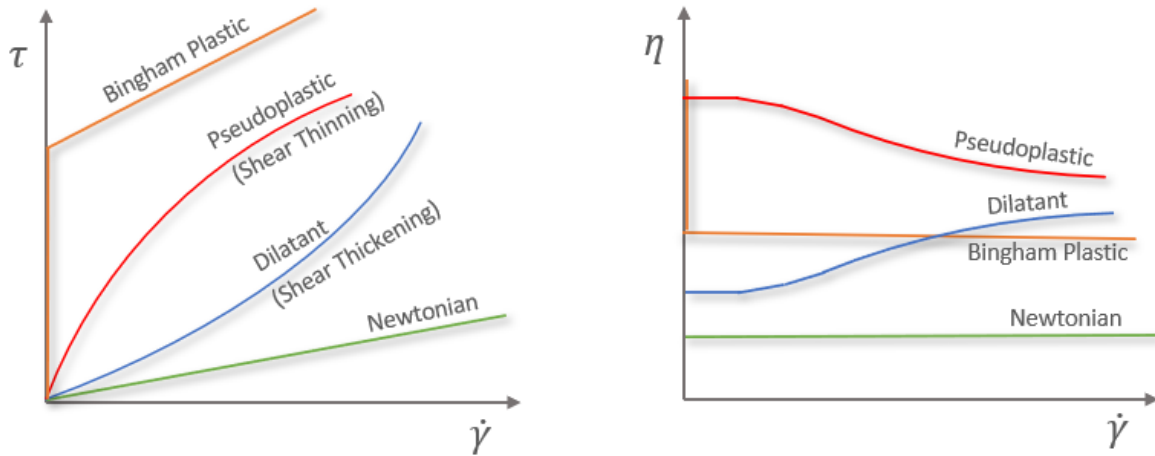


Figure 2.6: Schematic fluids behaviour of shear stress (left) and viscosity (right) as a function of shear rate

### 2.4.2. BULK RHEOLOGY OF HPAM

During the flow of polymer and foam water-solutions, suspensions of moderate concentrations and biofluids, shear-thinning behaviour is effortlessly noticed in rheometer, i.e., monotonically-decreasing apparent viscosity upon increasing shear rate [25]. However, research findings on the subject of viscoelastic polymer point to wide disparities between the bulk rheology in porous media and the bulk rheology in rheometer. Albeit the majority of polymers possess the characteristic of shear thinning, shear-thickening behaviour is obviously observed on viscoelastic polymer under moderate-to-high shear rates in porous medium. Of the xanthan and HPAM that are the major candidates for chemical flooding, the latter one are investigated to flow in a more complicated pattern with viscous and elastic behaviour coexisting.

Numerous research workers such as Hirasaki and Pope [26], Heemskerk et al. [27], and Masuda et al. [28] and the laboratory study conducted by Chauveteau [3] (Fig. 2.7) confirmed the dilatant behaviour of polymer by convincing experimental data and meticulous reasoning. Their endeavours were centred around the demonstration of the shear-thickening phenomenon of polymer solution with regard to molecular configuration and flowing state.

Based on the above results of previous research, it has come to a conclusion that the intertwined and randomly-oriented HPAM molecules go through three easily distinguishable periods in aqueous phase. In general, the bulk rheology of HPAM can be interpreted as three flowing schemes: (1) Newtonian behaviour (constant contact viscosity) at low shear rates, (2) shear thinning at intermediate shear rates, (3) shear thickening at higher shear rates (Fig. 2.8). The three flowing regimes take two critical shear rates as the boundary. The physical principles behind will

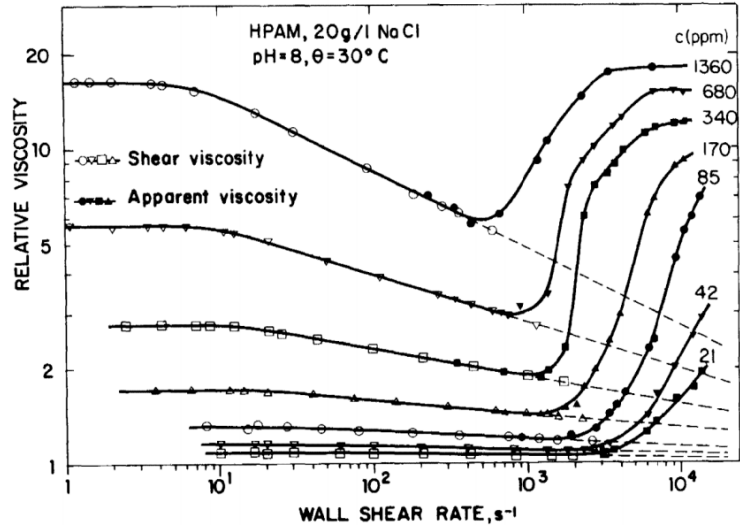


Figure 2.7: Illustrations of HPAM relative viscosity changing with shear rate under the effect different polymer concentrations [3]

be explained in detail in 2.4.4, 2.4.5 and 2.4.6.

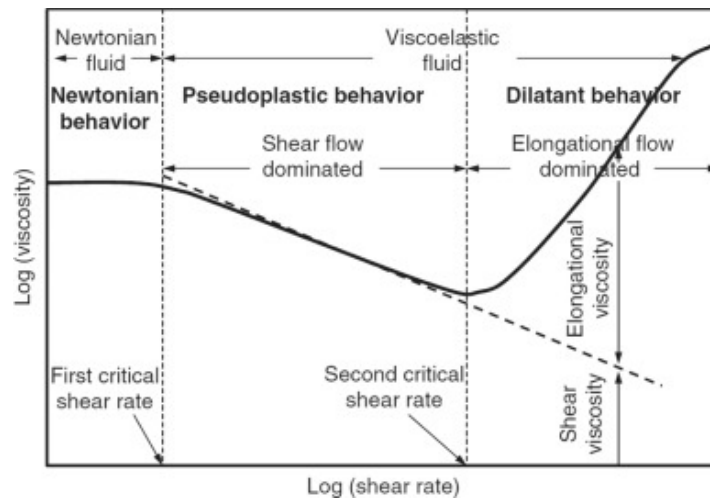


Figure 2.8: Schematic illustration of the three stages of viscoelastic fluid flow in porous media [3]

### 2.4.3. EFFECTIVE SHEAR RATE

The things that the rheological parameters of non-Newtonian fluids (e.g., viscosity, shear stress, dynamic modulus, etc.) have in common is the association with shear rate. Accordingly, the calculation of the shear rate is of great significance in the rheology evaluation of non-Newtonian fluids. For the capillary model, the effective shear rate can be defined as the rate of change of the

fluid flow velocity with respect to the radius of the circular channel in Eq. 2.2.

$$\gamma = \frac{\tau}{\mu} = \left| \frac{du}{dr} \right|, \quad (2.2)$$

where  $u$  is the Darcy velocity of fluid, cm/min, which is the ratio of superficial velocity over porosity  $\phi$ ;  $r$  denotes the average pore radius of porous media, cm, which is revised combining equivalent capillary radius of porous media and tortuosity degree,  $cm$  [29]. Scholars put forward the mathematical derivation of the shear rate of the power-law fluid based on the cylindrical capillary model, and in the meanwhile put forward the more consummate formula by empirical revision through a large quantity of experiments [30].

#### 2.4.4. ZERO-SHEAR VISCOSITY (FIRST STAGE)

At a low shear rate, the shear stress exerted on the solution is small which enables the polymer molecular coils to be approaching to and entangled with each other. In this scenario, intermolecular gravitational force is large and the molecular conformation keeps stable, thus generate a high apparent viscosity unaffected by the flow. The rheological behaviour of HPAM aqueous solution is Newtonian below the first critical shear rate, where its shear viscosity is a certain value, which is also named zero shear viscosity. Many studies have shown that zero-shear viscosity is related to factors including polymer concentration, degree of salinity and hardness, temperature, molecular weight, pH value, etc. (Fig. 2.9).

##### Concentration

Fig. 2.9(a) manifests the relationship between the apparent viscosity and the shear rate of 3330S polymer solutions with concentration being the control variable at the fixed reservoir temperature and salinity. As the higher concentration of polymer being injected, the corresponding curve moves upward which specifies that the increment the polymer concentration can not only amplify the pseudoplastic characteristics of the solution, but also enhance the viscosity of the polymer. This is due to the fact that the greater the mass concentration of polymer molecules, the more molecules and the stronger the molecular interaction in the aqueous solution. The intensified molecular motion contributes to more opportunities for the penetrating and ravelling of molecular chains or coils to happen, and therefore brings about better thickening effect to the initial viscosity under zero shear force.

Table 2.2: Conceptual mathematical models of effective shear rate

Source	Equations	Suitability and limitations
Kozeny 1927 [31] and Car- man 1937 [32]	$\gamma_{eff} = \frac{4u L_e}{\phi r L}, \quad (2.3)$ <p>where <math>u</math> is the Darcy velocity, <math>cm/s</math>; <math>\phi</math> is porosity; <math>r</math> is the average pore radius, <math>cm</math>; <math>L_e</math> and <math>L</math> are lengths of torturous tubes and porous medium respectively, <math>cm</math>.</p>	The most straightforward version of capillary tube model on the assumption of no connection, uniform size and constant pressure drop along the flowing path.
Hirasaki and Pope 1974 [26]	$\gamma_{eff} = \left(\frac{3n+1}{4n}\right)^{\frac{n}{n-1}} \frac{12u}{\sqrt{150K_p\phi_w}}, \quad (2.4)$ <p>where <math>n</math> is the bulk power law index; <math>K_p</math> is polymer permeability and <math>\phi_w</math> is the occupied percentage of total porosity by water. Whereby the tortuosity is set to be 25/12.</p>	To illustrate, it gives consideration to the permeability reduction for HPAM but is still exposed to bias when the resistance reduction factor (RRF) is large; a nice fit can be found towards xanthan laboratory results.
Cannella,Huh et al.1988 [33]	<p>Base case:</p> $\gamma_{eff} = \left(\frac{3n+1}{4n}\right)^{\frac{n}{n-1}} \frac{u}{\sqrt{K\phi}}, \quad (2.5)$ <p>Modified case:</p> $\gamma_{eff} = \left(\frac{3n+1}{4n}\right)^{\frac{n}{n-1}} \frac{u_{aq}}{\sqrt{k_{aq}S_{aq}\phi}}, \quad (2.6)$ <p>where <math>k_{aq}</math> is effective permeability of aqueous phase, <math>cm^2</math>; <math>S_{aq}</math> is aqueous saturation; <math>n</math> is the bulk power law index; <math>C</math> is correction coefficient derived from experiments; <math>u</math> and <math>u_{aq}</math> are the total Darcy velocity and aqueous phase velocity respectively, <math>cm/s</math>.</p>	This equation is deduced to correlate the propagation of xanthan gum solutions in cores through the trials on different connectivity, lithology and the oil-bearing content.
Dauben and Men- zie, 1967 [34]	$\gamma_{eff} = \frac{12\sqrt{2}u(1-\phi)}{D_p\phi}, \quad (2.7)$ <p>where <math>D_p</math> is the diameter of grains, <math>\mu m</math>.</p>	Spot on the swelling properties of polymers in porous media
Zitha, Chauveteau et al. 1995 [35]	<p>Average pore radius:</p> $r = \left(\frac{8k}{\phi}\right)^{1/2}, \quad (2.8)$ $\gamma_{eff} = \alpha \frac{4u}{r}, \quad (2.9)$ <p>where <math>k</math> is permeability, <math>cm^2</math>; <math>\alpha</math> is the shape parameter depending upon the pore arrangements, which is different between packs of large spheres having and packed beds of angular grains.</p>	Analogue experimented by packed glass beads with a flaw of almost identical pore structures. The drawback is that the shear rate is computed to be at the pore wall of at the average pore radius.

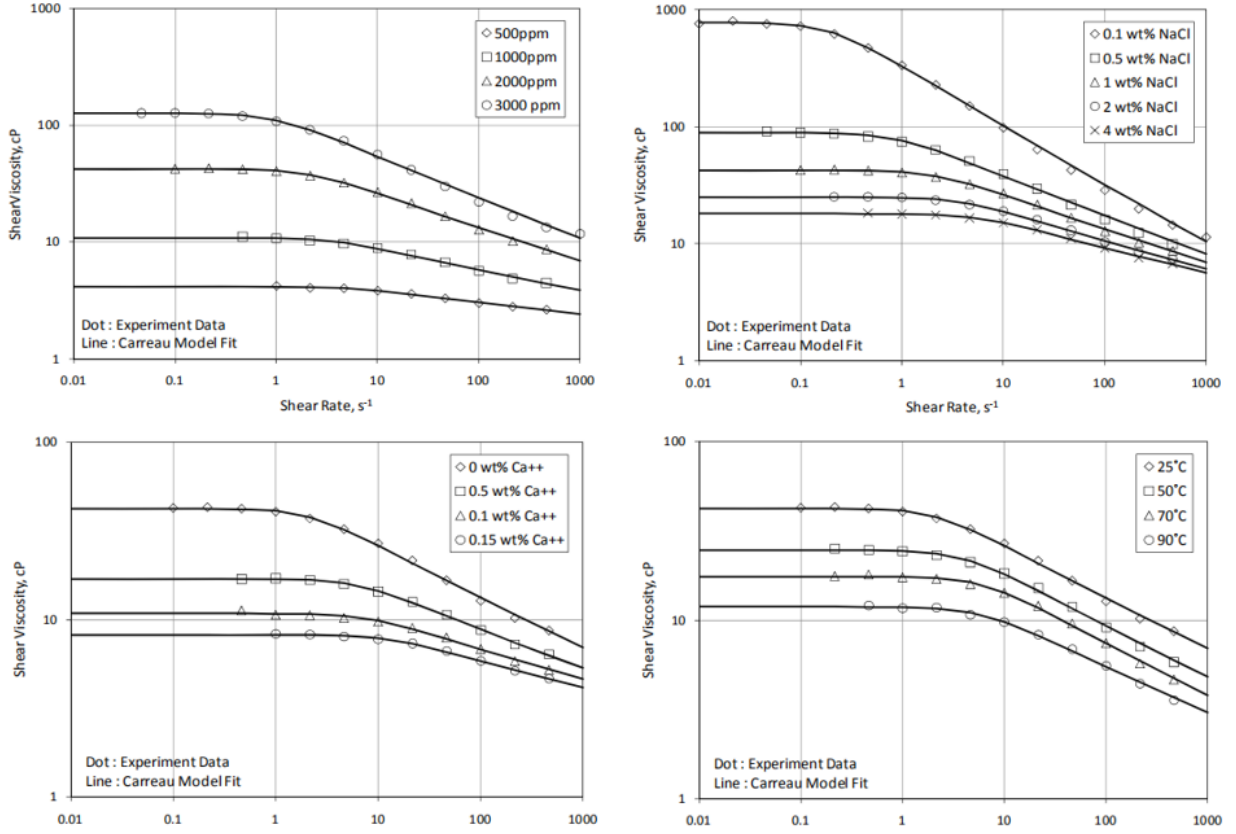


Figure 2.9: (a) Shear viscosity of polymer 3330S at different concentrations (1% NaCl at 25°C); (b) Shear viscosity of polymer 3330S at different salinity (2000 ppm at 25°C); (c) Shear viscosity of polymer 3330S at different hardness (2000 ppm in 1% NaCl at 25°C); (d) Shear viscosity of polymer 3330S at different temperature (2000 ppm in 1% NaCl) [4]

Among the recent literature, piecewise function with a critical concentration partitioning the domain is employed to deal with the zero-shear viscosity of polymers [36, 37], but the Flory-Huggins equation [38] which describes the relationship between the zero-shear viscosity, the polymer concentration, and the intrinsic viscosity is still practical and of wide-spread use for general simulator development[37].

$$[\mu] = \lim_{C_p \rightarrow 0} \frac{\eta_{sp}}{C_p} = (A_{p1} + A_{p2}C_p + A_{p3}C_p^2 + \dots + A_{pi}C_p^{i-1})C_{SEP}^{SP}, \quad (2.10)$$

where  $[\mu]$  is the intrinsic viscosity, the upper limit of the specific viscosity ( $\eta_{sp}$ ) when approaching to zero concentration,  $C_p$  is the polymer concentration and  $A_{p1}, A_{p2} \dots A_{pi}$  are constants fitted by experiments.  $C_{SEP}$  is degree effective salinity and  $S_p$  is exponent to characterize the effect of salinity.

Plugging the expression of  $\eta_{sp}$  (Eq. 2.11) in Eq. 2.10 and regrouping the terms gives Eq. 2.12

we've got

$$\eta_{sp} = \lim_{C_p \rightarrow 0} \frac{\mu_p^0 - \mu_w}{\mu_w}, \quad (2.11)$$

$$\mu_p^0 = \mu_w (1 + (A_{p1}C_p + A_{p2}C_p^2 + A_{p3}C_p^3 + \dots + A_{pi}C_p^i)C_{SEP}^{SP}), \quad (2.12)$$

where  $\mu_p^0$  is the zero-shear viscosity and  $\mu_w$  is the solvent viscosity, which is most commonly the viscosity of pure water. Even though Eq. 2.12 is represented in a form of infinite power series, a finite number of terms with the exponent being no more than 3 is kept for dilute solution [39].

### Salinity & Hardness

Dependence of apparent viscosity on salt concentration under low shear rate condition is revealed in Fig. 2.9(b) (c). The rule is: at fixed shear rate, the apparent viscosity declines along with the enlargement of the salt content. The core cause is that the introducing ions neutralize the charge on the side groups of HPAM. When HPAM is dissolved in water, the  $Na^+$  on the  $COONa^+$  group is ionized to form electronegative repeated subunits, and the  $-COO^-$  group on the polymer chain repels each other, which makes the chain conformation more stretched with larger active volume, and harder to flow. When salt is added, a part of  $Na^+$  is relatively concentrated around  $-COO^-$ , which shields the effective charge and weakens the curling and extension effect of the molecular chain as a result of the repulsion of anions. As a consequence, the size of HPAM solute has diminished to a large extent, and so does the apparent viscosity.

Moreover, the nature of the ions dissociated in the water enables the polyacrylamide molecules to expand or contract via electrostatic repulsion. The hardness of solvent in turn affects the three-dimensional geometry, effective volume and the initial viscosity of the HPAM solution. Zhao, et al. proved through experimental data that the cations occupy a higher position than anions, and their ranking obeys the following order:  $Fe^{2+} > Fe^{3+} > Mg^{2+} > Ca^{2+} > Na^+ > K^+$  [40]. The divalent and trivalent ions such as  $Fe^{3+}$  and  $Mg^{2+}$  have a more significant effect on polymer properties compared to monovalent ions ( $Na^+$  and  $K^+$ ) owing to larger quantity of electric charge and higher-degree polarizability [39].

Reckoning with the dependence on hardness, a modified Flory-Huggins function has been developed empirically [38] in Eq. 2.13

$$\mu_p^0 = \mu_w (1 + (A_{p1}C_p + A_{p2}C_p^2 + A_{p3}C_p^3 + \dots + A_{pi}C_p^i)C_{sep}^{S_p}), \quad (2.13)$$

where  $C_{sep}$  is the effective salinity in unit of meq/ml and  $S_p$  is a constant value less than 1.0 from

laboratory test to ensure a monotonically decreasing trend of  $\mu_p^0$  with the increase of  $C_{sep}$ .  $C_{sep}$  is defined as [41]

$$C_{sep} = \max(C_{anion} + (\beta - 1)C_{d-cation}, C_{SE1}), \quad (2.14)$$

where  $C_{anion}$  and  $C_{d-cation}$  are the concentrations of anions and divalent cations respectively in meq/mL,  $\beta$  quantifies the relative influence of divalent cations on polymer viscosities in comparison with monovalent cations and  $C_{SE1}$  is input as a upper limit to avoid irrational calculation. Hereby  $\beta = 1$  is a midpoint which suggests the same contributes of monovalent and divalent cations; the values larger or smaller than 1 denote a stronger or weaker role of divalent cations than monovalent cations respectively.

### Molecular Weight and Molar Mass Distribution

As depicted in Fig. 2.10, when all other variables keep equal (temperature and concentration), the higher the molecular weight of the polymer, the higher the apparent viscosity would be. This is because the greater the relative molecular mass of the polymer, the longer the molecular chain, the easier it is to originate entanglements between the molecule chains, and ultimately the greater the viscosity.

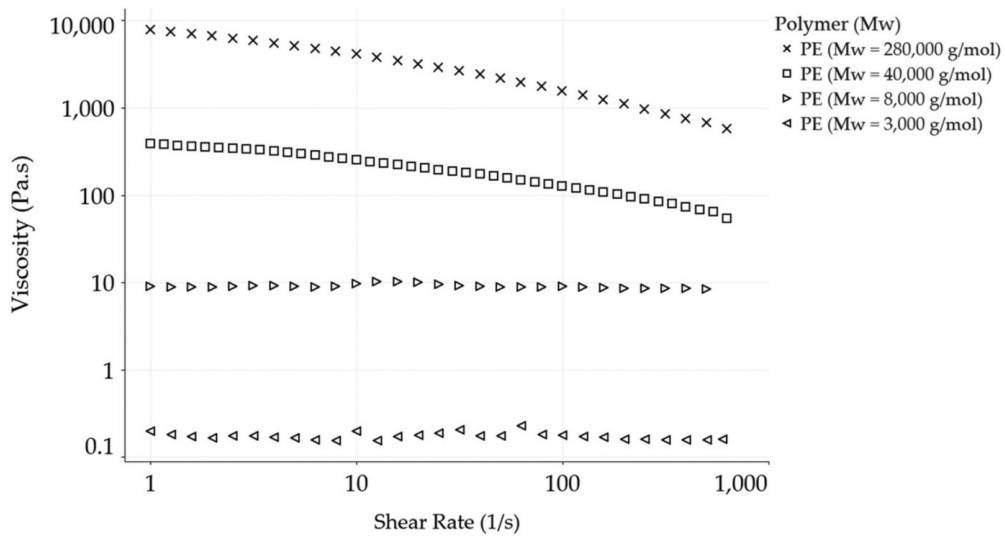


Figure 2.10: Viscosity measurements of polymer melts taken from plate-plate rheometry used in rotary jet spinning (RJS). Four scenarios from high Mw to low Mw of polyethylene has been set up from top to bottom [5]

Carreau et al. [42] defined the intrinsic viscosity as a inherent character of polymer whose value does not vary with concentration. Intrinsic viscosity is quantified contribution (hydrodynamic volume) of individual molecule in a given solvent which is quantitatively related with the

relative molecular mass of the polymer which is defined as

$$[\mu] = \lim_{C_p \rightarrow 0} \frac{\mu_p^0 - \mu_w}{\mu_w C_p} = \lim_{C_p \rightarrow 0} \frac{\eta_{sp}}{C_p}, \quad (2.15)$$

where the value of  $[\mu]$  measured by a capillary viscometer is often used to procure the relative molecular mass utilizing Mark-Houwink relation [43], as Eq.2.16.

$$[\mu] = K' M_w^a, \quad (2.16)$$

where  $[\mu]$  is the intrinsic viscosity,  $M_w$  is termed weight average molar mass,  $K'$  and  $a$  are constants determining by a particular type of polymer and solvent at a given temperature. The value of  $K'$  locates in an great interval of  $3-700 \times 10^{-5} \text{ cm}^3/\text{g}$  and  $a$  has a slight fluctuation within a range from 0.5 to 1 [39]. In this way, for any specific polymer solution, a larger molecular weight will bring to a larger intrinsic viscosity, mathematically corresponding to a steeper slope of  $\frac{\mu_p^0 - \mu_w}{\mu_w}$  versus  $C_p$  and higher climbing speed of  $\mu_p^0$  within fixed polymer concentration change.

Besides, the molecular weight distribution also makes a difference. For monodisperse polymers and polymers with narrow-range distributed molecular weight, the zero shear viscosity of the solution is primarily determined by the weight average molecular weight while the polymer with a wide molecular weight distribution does not hold direct linkage between the solution viscosity and the weight average molecular weight. The maximum value at the tail of the molecular weight distribution curve plays a pivotal part and on this account out of two polymer samples with the same weight average molar mass the one with an extensive range of  $M_w$  may have a higher shear viscosity than the one with a limited range.

### Temperature

As is illustrated in Fig. 2.9(d), the higher the reservoir temperature, the worse the viscosity-increasing effect of the polymer. However, no obvious influence of temperature is noted on the next pseudoplastic stage of the polymer. Temperature comes into play in the thermal motion of molecules, which is a reflection of the intensity of irregular particle movement. Further, intermolecular kinetics need to overcome intermolecular forces (hydrogen bonds among molecules, orienting and twisting of molecular chain, etc.), which have been cited as major reasons for changes in molecular dimensions, and in turn affects the viscosity of the polymer.

The Arrhenius equation delineates the variation of viscosity as a function of temperature in

Eq. 2.17

$$\eta = A_p \exp \frac{E}{RT}, \quad (2.17)$$

where  $A_p$  is the pre-exponential factor,  $E$  is the activity energy,  $R$  is the Regnault gas constant, and  $T$  is the absolute temperature.  $A_p$  and  $E$ , which elucidate the collision frequency of polymers, both rely on the polymer concentration, type of solvent, and the molecular mass distribution [44]. The basic principle is that as the temperature ascends, the intensified movement, loosened twining points between molecules and the isolated macromolecules coils reduce the frictional resistance between the flowing molecules and eventually impair viscosity. Therefore, an appropriate temperature should be selected to maximize the polymer viscosity during the polymerization. Generally, room temperature preferably at 10-18°C would be appropriate.

#### 2.4.5. SHEAR-THINNING MODEL (SECOND STAGE)

The macromolecules have to cross several liquid layers with different flow rates during the flow. This state of different parts of the same macromolecule moving at inhomogeneous speeds is obviously not sustainable. For that reason, each long-chain molecule always makes an effort to enter the same flow rate layer, and the conformation of polymer deviates from the equilibrium and is oriented along the flow direction under the shearing effect. Additionally, it is ordinarily accompanied by the untwisting and separation of molecular chains. The orientation and disentanglement scale down the resistance to mutual molecular motion, thus reducing viscosity.

Mathematical description of pseudoplastic rheology involve Meter, Cross, Carreau, Ellis and Prandtl-Eyring regression models, among which the generally recognized one is the power law model of viscosity versus shear rate [45]

$$\mu = K\gamma^{n-1}, \quad (2.18)$$

where the dual-parameter model contains consistency factor  $K$  and power exponent  $n$  within a range of 0~1. The shortage is that it merely plots a monotonically decreasing function with a quite narrow applicable scope of shear rate. Two limits can be seen, the one is the approximate zero viscosity when the shear rate tends to infinity, and the other one is the infinite viscosity when the shear rate goes to 0. Undeniably, a simple power law is incapable to match the real situation for the Newtonian plateau (the 1st stage) is not taken into consideration.

A more realistic approach integrating the two stage is the Carreau-Yasuda model [46] (see Eq. 2.19) which is most often used in established simulators such as UTCHEM [47]

$$\frac{\mu - \mu_{\infty}}{\mu_p^0 - \mu_{\infty}} = [1 + (\lambda \dot{\gamma})^a]^{\frac{n-1}{a}}. \quad (2.19)$$

This is a five-parameter model, where  $\mu_p^0$  and  $\mu_{\infty}$  represent the viscosity at zero shear rate and infinite shear rate, respectively, and the power index  $n$  reflects the degree of shear thinning. As shown in Fig. 2.11, the width of the transitional region between zero-shear viscosity and shear-thinning part, is in control of the parameter  $a$ , which is well fitted to be 2.  $\mu_p^0$  is proportional to molar mass, and  $a$  is proportional to molar mass distribution (MMD).

And the time constant  $\lambda$  (also known as relaxation time) is physically signified that  $\frac{1}{\lambda}$  corresponds to the characteristic shear rate at which the viscosity leaves the Newtonian fluid regime and turns to the shear-thinning regime.

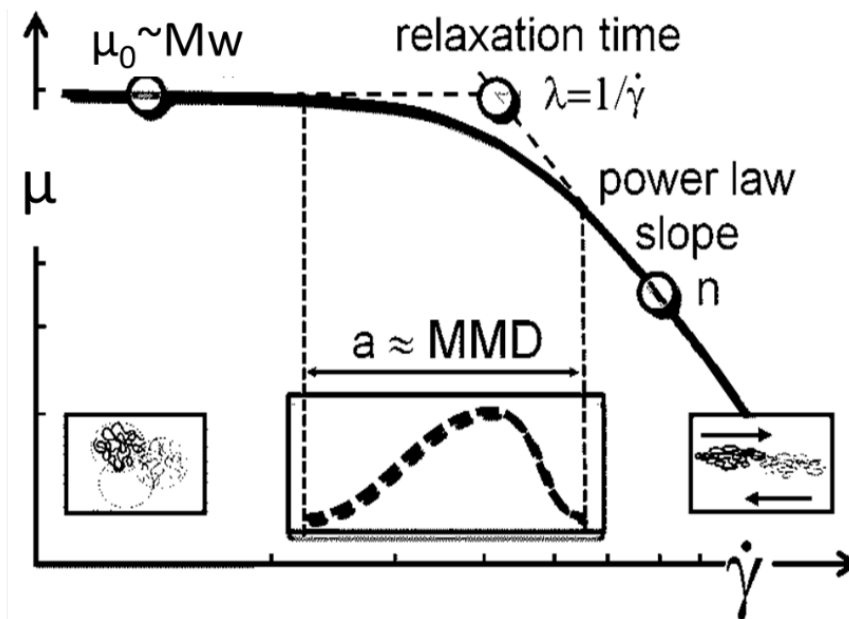


Figure 2.11: Regression model of viscosity-shear rate relationship by Carreau-Yasuda (www.anton-paar.com) [6]

#### 2.4.6. SHEAR-THICKENING MODEL (THIRD STAGE)

In the high-shear zone, the entanglement of macromolecular segments has all been straightened, revealing the properties of Newtonian fluid and minimizing the viscosity. However, the elastic property left it barely maintain a constant. The shear-thickening behaviour is linked to elasticity, which is determined by polymer relaxation time in the porous media. The polymer molecules sit-

uate in numerous channels with converging-diverging geometries in porous material. As a result of the areal change in the cross section, the molecules are susceptible to be accelerated and decelerated. No extensive viscosity occurs if the time interval between two consecutive changes in the diameter of the pore throat (becomes large or small) is long enough for the polymer molecules to return to their previous condition, in this manner shear thinning is maintained. Else, if the polymer relaxation time is longer than the lasting time from one shrinkage to the next shrinkage, for example at a very large superficial velocity, the polymer molecular chain remains prolonged and discrete-distributed and the elongational viscosity is observable.

The models mentioned in Subsection. 2.4.5 all suffer the fact that pure viscosity of fluids is assumed. For assessing the onset node of viscosity enhancement in porous media, Deborah number is a theory-supportive interpretation as well as an imperative factor. The Deborah number is defined as the ratio of the rotational relaxation time  $\tau_r$  to the characteristic period for elongation and contraction in a specific porous media  $\tau_E$  in Eq. 2.20, taking into consideration the effects of both the viscoelasticity of specific polymer and the structure of porous medium [48]

$$N_{DE} = \frac{\tau_r}{\tau_E} = \tau_r \dot{\gamma}_{eff}, \quad (2.20)$$

where it is necessary to estimate the characteristic residence time ( $\tau_E$ ), often considered to be the reciprocal of the stretching rate ( $\dot{\gamma}_{eff}$ ), also known as effective shear rate as specified in Subsection. 2.4.3).

Delshad et al. [49] came up with the following Eq. 2.21 of shear thickening in relation to the Deborah number and effective shear rate

$$\mu_{ex} = \mu_{max}[1 - \exp(-\lambda_2 \tau_r \dot{\gamma}_{eff})^{n_2-1}]. \quad (2.21)$$

Herein  $\mu_{ex}$  is increment of elongational viscosity caused by dilatant behaviour,  $\mu_{max}$ ,  $\lambda_2$ , and  $n_2$  are regression constants determined empirically. The product of  $\tau_r$  for a polymer molecule and  $\dot{\gamma}_{eff}$  for a typical porous material comes to the  $N_{DE}$ .

The shear thickening in polymers occurs not only in intricate media with versatile pore radius but also in area surrounding the wellbore and with poor permeability [50]. The elongated distortion in the vicinity of the well generates an increase in the injection pressure. This would result in a considerable drop in the rate of injection, since areal sweeping efficiency may be reduced with potentially severe risk of fracturing [26].

### 2.4.7. INTEGRATED VISCOSITY MODEL COMBINING THREE STAGES

Delshad et al. [49] reported a comprehensive viscosity model for HPAM solution by combining the shear thickening part with the Newtonian and shear thinning part of the Carreau equation together in Eq. 2.22. Compared to the other models with a focus on local rheology in rheometer, the unified version is capable to correlate the viscosity of HPAM solution with a complete spectrum of Darcy velocity and shear rate. Another aspect is that the highly-merged model has the benefit of simply entailing rheological and petrophysical data regarding typical polymer and porous media of study area respectively

$$\mu_{app} = \mu_w + (\mu_p^0 - \mu_w)[1 + (\lambda\dot{\gamma})^2]^{\frac{n-1}{2}} + \mu_{max}[1 - \exp(-\lambda_2\tau_r\dot{\gamma}_{eff})^{n_2-1}]. \quad (2.22)$$

Here,  $\mu_{app}$  and  $\mu_p^0$  are the polymer viscosity under apparent and zero shear rate, respectively,  $\mu_w$  is viscosity of solvent (hereby water),  $n$ ,  $n_2$ ,  $\lambda_2$  and  $\mu_{max}$  are empirically fitted constants from laboratory,  $\lambda$  and  $\tau_r$  are proven to possess functional relationship with the polymer concentration, and  $\dot{\gamma}_{eff}$ , the dominate variable through the polymer in-situ rheology, is the effective shear rate which is exhaustively written up in Subsection. 2.4.3.

## 2.5. POLYMER RETENTION IN POROUS MEDIA

**D**UE to surface adsorption, mechanical entrapment, and hydrodynamic retention, the flow of polymer solutions in porous media suffers from retention and stagnation, aggravating flow resistance and affecting the pore structure of cores for one thing, and inducing the loss of flowable polymers for another.

### 2.5.1. RETENTION MECHANISM

#### Retention mechanisms

Retention mechanisms are classified as surface adsorption, mechanical entrapment and hydrodynamic retention (in Fig. 2.12). However, with the pore radius ( $R_p$ ) and hydraulic radius ( $R_h$ ) being used as a criteria of classification, in media of low permeability ( $R_p < 3R_h$ ), medium permeability ( $3R_h < R_p < 50R_h$ ) high permeability ( $R_p > 50R_h$ ) [39], the ranking of these three mechanisms is shuffled in order of importance.

- Surface adsorption arises as a result of electrostatic interaction, van der Waals forces, and

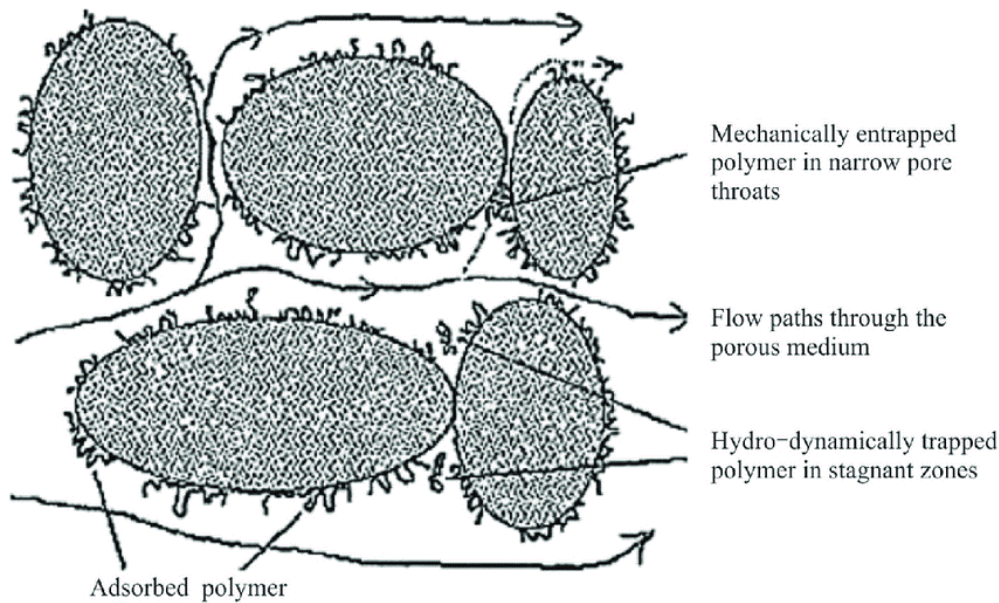


Figure 2.12: Retention mechanisms in porous media [7]

hydrogen bonds formed between polymers and minerals. The adsorption of these groups on the grain surface is solely point contact, with the macromolecular chain floating in solution as coils. Thereby, the amount of surface adsorption is proportional to the size of the rock's surface area. Furthermore, the adsorbed polymer and the polymer in the solution can indeed interact with each other. The hydrophilicity of the amide and carboxyl groups of HPAM enables the huge number of hydrophilic groups at the tail of molecular coils in the solution to trap a large amount of water.

- **Mechanical entrapments:** Retention occurs when the size of the flow channel in a pore media is smaller than the size of the polymer molecules, which typically happens in pore channels that are sizable at the inlet end (large enough for polymer molecules to flow in) but minuscule or closed at the exit end (unsupportive for polymer molecules to flow out). Physical polymer trapping tends to happen in low permeability pore media, as seen in Fig. 2.13, where some of the long chain molecules have been already immobilized at the inner wall of pore throats.
- **Hydrodynamic retention:** As the displacement advances inward, both the flow pressure difference and the pair of shear stress and tensile stress of macromolecules decrease, and the geometric state of macromolecules spontaneously shifts to irregular coil, which is the process of tectonic entropy production. The slowing-down flow due to the reduced differential pressure helps a portion of the stuck molecules to move out and into the water stream. These curled molecules are harder to pass through the pore space than the stretched conformation

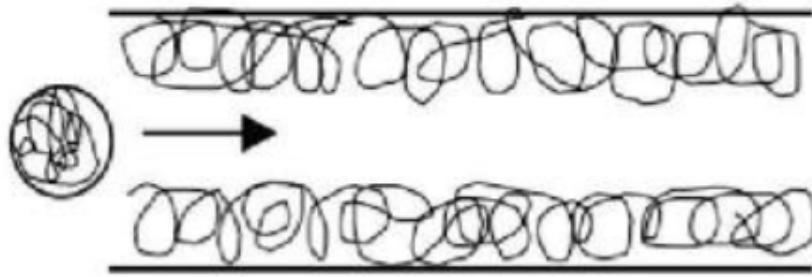


Figure 2.13: The schematic diagram of mechanical entrapment

they had at higher flow velocities when they entered the large core.

Adsorption is a more essential feature of the system with polymer being solute and rock surface being solvent that can't be resolved unless a different polymer is attempted, which is the most crucial mechanism to investigate when evaluating a polymer flood program. For most practical treatments, mechanical entrapment should be viewed as a screening variable and inhibited, while hydrodynamic retention is minor and may be ignored. From all circles, the remainder of this chapter will be primarily concerned with adsorption [39].

### Static & Dynamic adsorption

The level of static adsorption plainly reflects the interaction between polymer molecules and the rock surface, without considering the retention produced by mechanical and hydrodynamic trapping. The hysteresis induced by the polymer during its flow is referred to as dynamic adsorption. All three retention mechanisms are involved in dynamic adsorption, while the static adsorption is restricted to the first form of adsorption at the surface.

The static adsorption volume is substantially bigger than dynamic adsorption volume for the same core. The former one do not adequately characterize the adsorption pattern of the actual reservoir, thus they must be corrected by the dynamic data. The inaccessible volume and unconnected pores of the core underlies the mismatch. With regard to the static adsorption, the polymer cannot flow through the pores filled by oil and water under a given driving force. As polymers travel through the accessible spaces in the rock, the contact surface will become smaller. What's more, the washing out process when testing the adsorption dynamically erodes the rock and alter the physical traits of the core.

### 2.5.2. ADSORPTION OF HPAM

There are several factors associated with the degree of static adsorption of polymer. Firstly, it is the properties of the polymer itself, such as polymer type, molecular weight, degree of hydrolysis, polymer concentration, etc.; in the second place, it is the properties of solvent that configures the polymer solution, in particular the salt content, ion types, etc.; the third factor is the reservoir conditions, for instance the mineral composition of rock particles, surface properties, and reservoir temperature. Generally speaking, low salinity of the aqueous solution and the rise in temperature is not conducive to adsorption, and the surface of carbonates is easier to adsorb than the surface of sandstone. Prior to the critical value of adsorption capacity, the adsorption amount mounts up with the polymer concentration.

The static adsorption of diverse variations of polyacrylamide have been researched in depth by Mungan [51], Smith [52], Schamp et al. [53] and their findings are summarized as follows:

1. Langmuir-type adsorption isotherms can be used to interpret the adsorption of unhydrolyzed and partially hydrolysed polyacrylamide on assorted adsorbents.
2. The adsorption is of great irreversibility due to hydrogen bonding and chemical bonding between the carboxyl groups and the surface groups of the adsorbent.
3. The wettability of the rock surface strongly impacts the adsorption capacity of HPAM. HPAM has a massively higher adsorption capability on water-wet rocks than on oil-wet rocks.
4. The amount of HPAM adsorption loss is primarily determined by the number of carboxyl groups on the molecular chain, to that end the degree of hydrolysis has the strongest influence, followed by the average molecular weight. This is indicative of the fact that the coil swells as the average molecular weight and hydrolysis level get up, the polymer begins to be sparsely distributed with less density, and further less effective retention.
5. The inorganic electrolytes gives a strength to the ability of adsorbing HPAM. The single-displacement reaction lies behind where monovalent ions (i.e. sodium, potassium, etc.) dissociated from the carboxyl group of HPAM are replaced by the metal divalent ions in the clay minerals. The shield between the carboxyl groups formed by divalent cations is exacerbated which compresses the structure of the coil.
6. The adsorption capacity measured in static and dynamic settings differs markedly. This is on the ground that the area of the rock surface that the HPAM solution touches is non-identical.

### 2.5.3. TYPES OF ISOTHERM ABSORPTION AND CALCULATION OF POLYMER RETENTION

Scholars have formulated a series of isotherm adsorption theories based on various physical interpretations, including the Langmuir and Freundlich equations stemmed from the dilute solution system [54], the Slibergerg model [55] discussed with the adsorption membrane structure and the BET theory assuming a multi-molecular-layers adsorption [56], and so on.

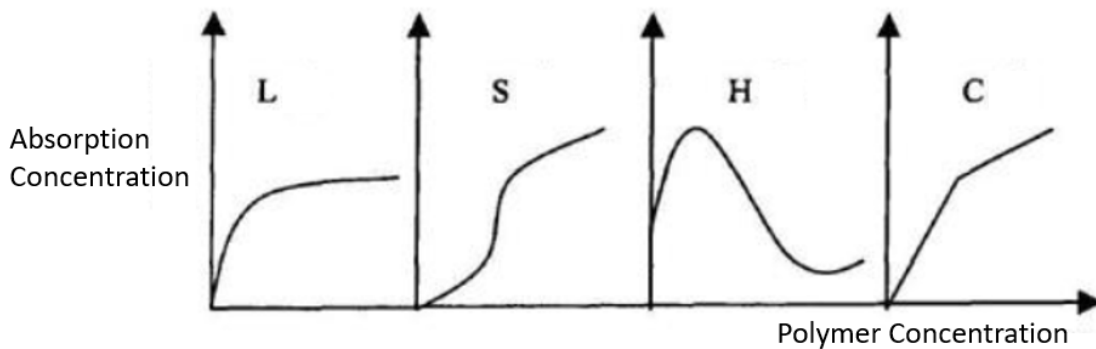


Figure 2.14: Types of adsorption isotherms in solid-dilute solutions system.

Giles et al. [57] inspected the adsorption of a huge group of dilute solutions and labelled them into four categories based on the slope of the initial part of the isotherm and subsequent changes, as sketched in Fig. 2.14. In dilute solutions, the Langmuir isotherm is the most prevalent form of adsorption isotherm. Solutes in dilute solutions are more likely to adhere than solvents with negligible competitiveness. Adsorbates are linear or planar molecules that are attached parallel to the surface along their long axis or plane.

#### Basic Assumptions:

1. The adsorbent's surface properties are uniform, where each molecule or atom with residual valence adsorbs a polymer molecule;
2. The polymer molecules are adsorbed in a single layer on the solid surface;
3. The adsorption process and the desorption process is analogous to gas condensation and liquid evaporation respectively. The moment adsorption equilibrium is achieved, the adsorption speed equals the desorption speed;
4. There is no force between the molecules adsorbing on the solid.

### Equation of Langmuir-type:

Eq. 2.23 and Fig. 2.15 are empirical representations of physical observations from Langmuir.

$$C_a = \frac{aC_p}{1 + bC_p}. \quad (2.23)$$

Here  $C_p$  and  $C_a$  [ $g/m^3$ ] are the species concentrations in the aqueous and on the rock phases.

The portion of retention monotonically increases with injected HPAM concentration, as shown in the Fig. 2.15, but by a very small margin. Typical polymer adsorption isotherms are quite steep; that is, they attain their plateau value at very low  $C_p$ . More concentrated polymers prop up higher occupancy of the adsorption sites, in which the number of molecules retained increases.

The scenarios while the rock is non-absorbed, partially-absorbed and fully-absorbed are considered and nicely integrated into one expression of Eq. 2.23.

- Zero absorption:  $C_p = 0, C_a = \frac{a}{1/C_p + b} = 0$ ;
- Partial absorption: at a certain  $C_p, C_a = \frac{a}{1/C_p + b} < 0$ ;
- Complete absorption:  $C_p \rightarrow \infty, C_a = \frac{a}{1/C_p + b} \rightarrow \frac{a}{b}$

From Fig. 2.15, the  $b$  in Eq. 2.23 governs the curvature of the isotherm, with the initial angle of the isotherm being more acute as the value of  $b$  rises and the ratio  $a/b$  determines the plateau value for adsorption. The sensitivity study of the constants of  $a$  and  $b$  has been organized exhaustively in Subsection. 4.3.3.

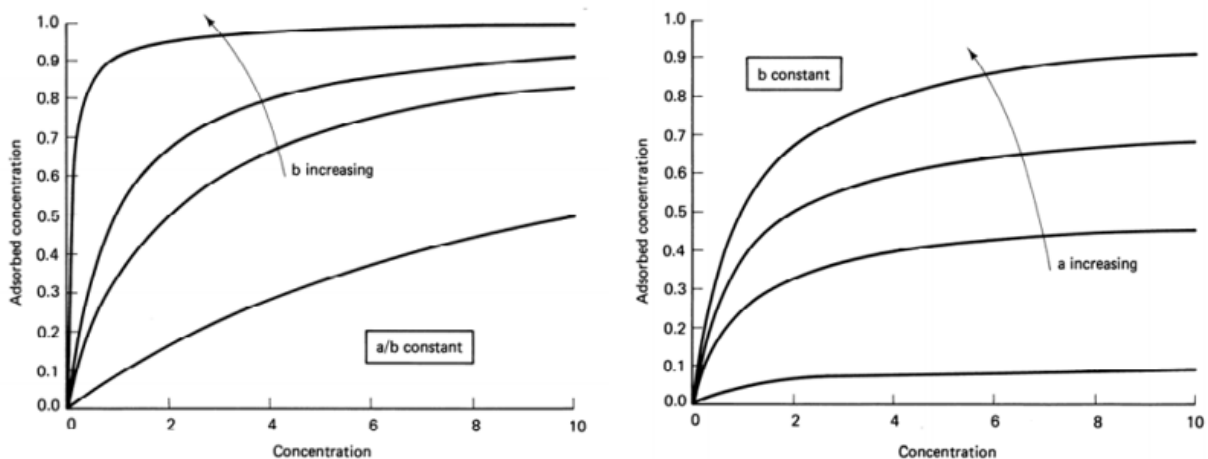


Figure 2.15: Typical shapes of Langmuir isotherm curves [8]

## Discussion

On account that the Langmuir isotherm was always untrue with the respect of mechanics that the majority of polymer retention is irreversible, the argument could be made that it should never have been headed for. Nevertheless, embedding the Langmuir model into the previous polymer-flooding simulator could be beneficial. If the Langmuir plateau is reached with a very low level of polymer, the polymer front is sharp enough and the injected polymer is relatively sufficient, applying Langmuir isotherm will not culminate in very inaccurate statements [58].

### 2.5.4. EFFECT OF POLYMER RETENTION ON POROSITY

#### Effect of Static Adsorption on Porosity

The upsurge in the polymer's resistance factor at high speeds is primarily due to the polymer's elasticity. At low speeds, the polymer flows in a more viscous behaviour due to its relatively high adsorption retention. Surface adsorption plus other methods of retention rely on rock surface and structure of pore network, impairing polymer concentration and viscosity by means of clogging the cross section of pores (see Fig. 2.16).

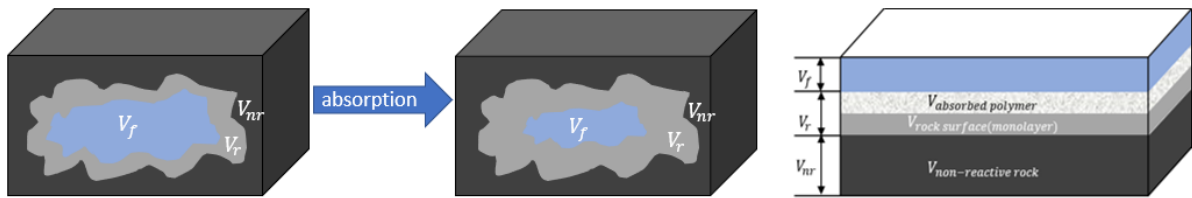


Figure 2.16: Porosity reduction process due to polymer adsorption. The domain consists of three distinct regions with the volume changing through the adsorption, particularly the fluid volume ( $V_f$ ) which is occupies by all the mobile phases (aqueous and oleic phase in the case of two phase flow), the reactive volume ( $V_r$ ) which consist of solid phases that can adsorb, and finally the nonreactive volume ( $V_{nr}$ ).

The treatment of porosity is an essential part of the simulator. The actual porosity depending on the amount of adsorbed polymer can be expressed as a function of the injected polymer concentration, as the sequence of derivations in Eq. 2.24

$$\begin{aligned}
 \frac{\text{Mass of adsorbed polymer}}{\text{solid volume}} &= C_{ps}, \\
 \frac{\text{Mass of adsorbed polymer}}{\text{bulk volume}} &= C_{ps}(1 - \phi_{ini}), \\
 \frac{\text{Volume of adsorbed polymer}}{\text{bulk volume}} &= \frac{C_{ps}(1 - \phi_{ini})}{\rho_p}, \\
 \phi_{new} &= \phi_{ini} - \frac{C_{ps}(1 - \phi_{ini})}{\rho_p} = \phi_{ini} - \frac{aC_p(1 - \phi_{ini})}{(1 + bC_p)\rho_p}.
 \end{aligned} \tag{2.24}$$

### Inaccessible pore volume

It is challenging for high molecular weight polymers to access some of the reservoir's smaller pores due to their large volume, which is referred as inaccessible pore volume (IPV). IPV is affected by the fluid kinetics and petrophysics, which is the hydrodynamic radius of the polymer as well as the permeability, porosity, and pore size distribution of the medium. It gets more prominent under higher molecular weight and less permeability-to-porosity ratio (characteristic pore size) [59].

Conversely, this does not imply a reduction in the polymer's effective porosity. This IPV is filled with pure brine (polymer-free solvent), which empowers polymer solution to spread faster through porous media than water, resulting in an earlier production well breakthrough [60]. The IPV-induced speed-up and adsorption-induced hysteresis of the polymer displacement can cancel each other out, as proved in Fig. 2.17. In most cases, the inaccessible void volume is less than 30% [61].

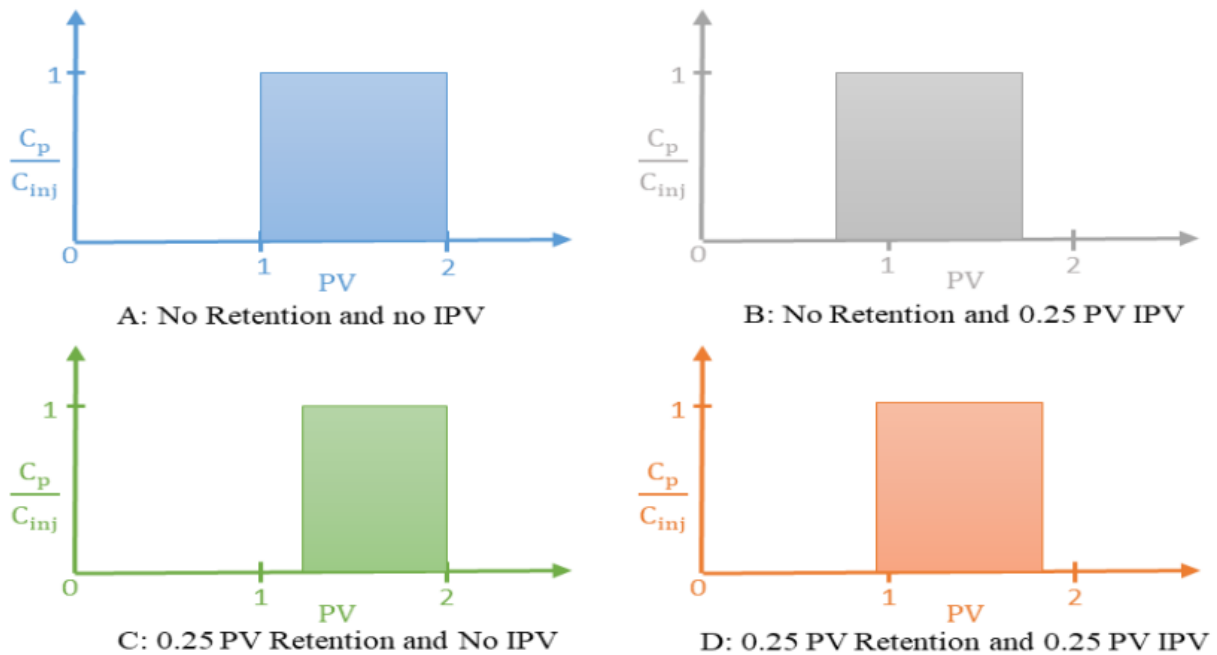


Figure 2.17: Ideal breakout curves in different conditions.

### 2.5.5. EFFECT OF POLYMER RETENTION ON PERMEABILITY

The permeability is reduced to different degrees when polymer molecules percolate and partly maintain in the pore medium, and the fluid is subject to greater resistance to flow. For a certain oil layer, the recovery rate of the polymer flooding is directly linked to the ability of the polymer

solution to improve the mobility ratio and reduce the permeability, that is, the resistance factor and the residual resistance factor, respectively.

The resistance factor is used to quantify mobility-lowering contribution, which is defined as the ratio of the mobility of injected water to the mobility of the single-phase polymer solution in Eq. 2.25

$$R_f = \frac{\lambda_w}{\lambda_p} = \frac{k_w \mu_w}{k_p \mu_p} = \frac{\Delta p_p u_w}{\Delta p_w u_p}, \quad (2.25)$$

where  $\Delta p_p$  and  $\Delta p_w$  are the pressure drop of single-phase water and polymer solution, respectively;  $u_w$  and  $u_p$  is the species flow rate of single-phase water and polymer solution, respectively.

The permanent loss of permeability of porous media due to polymer solution is represented by the residual reduction factor (also known as permeability reduction factor) in Eq. 2.26. It is a benchmark for the advancement of imbibition profile of the reservoir during polymer flooding and a measure of the polymer solution's ability to obstruct pore channels. The definition is the mobility ratio of the water before and after the injection of the polymer solution, and can alternatively be written as the ratio of the permeability of the brine before and after the injection of the polymer. The permeability reduction factor is contingent on the ratio of the layer thickness to the vertical pore diameters

$$RRF = \frac{\lambda_{wa}}{\lambda_{wb}} = \frac{\Delta p_{wa} u_{wa}}{\Delta p_{wb} u_{wb}} = \frac{k_{wi}}{k_{wa}}. \quad (2.26)$$

Here  $\lambda_{wa}$ , and  $\lambda_{wb}$  indicate the brine mobility before and after the polymer flowing-in;  $\Delta p_{wa}$ , and  $\Delta p_{wb}$  refer to the pressure drop of the brine before and after the polymer flooding;  $u_{wa}$ , and  $u_{wb}$  are the flowing velocity of brine before and after the polymer solution introducing;  $k_{wi}$ , and  $k_{wa}$  represent the effective permeability of brine before and after polymer injection.

The term  $R_{k,max}$  is the permeability reduction factor at its apex (equal to  $RRF$  for many cases) when the adsorption rate is at its highest, that is to say, when a single-layer polymer film has completely soaked the rock surface. Pope and Hirasaki [26] derived an expression of  $R_{k,max}$  based on the Poiseuille's Law from the perspective of radius diminution in the capillary tubes, similar to how we calculated the reduction of porosity from the perspective of volume shrinkage in Subsection. 2.5.4. According to experimental measurements, the thickness of polymers adsorbed on the solid surface as a monolayer has the identical value with the diameter of the dissolved molecular coil pointed to a particular solvent. As an outcome, the diameter of the molecular coil in solution will be used to model the thickness of the adsorbed layer.  $R_{k,max}$  is associated to the properties of the rock medium (such as porosity, permeability, tortuosity, etc.) as well as the

properties of the polymer (such as relative molecular weight, intrinsic viscosity, and so on), which is expressed as Eq. 2.27

$$R_{k,max} = \min \left( \left[ 1 - \frac{c_{rk}(A_{p1}C_{sep}^{Sp})^{\frac{1}{3}}}{\left(\frac{k}{\phi}\right)^{\frac{1}{2}}} \right]^{-4}, rkcut \right). \quad (2.27)$$

Here  $c_{rk}$  is another permeability reduction parameter, and  $rkcut$  is set to be 10 for normal polymer flood applications while it is adjustable for processes involved with gel or lower permeability rocks. Here,  $A_{p1} C_{sep}^{Sp}$  is equivalent to the intrinsic polymer viscosity,  $[\mu_p]$  (in  $wt\%^{-1}$ ).

In the numerical approach, permeability reduction factor ( $R_k$ ) is set to be of linear relation with the adsorption rate of polymer, as Fig. 2.18, with the slope of  $\frac{R_{k,max}-1}{\hat{C}_{p,max}}$  and the intercept of 1 at Y-axis [59]. The matched model states as Eq. 3.30

$$R_k = 1 + (R_{k,max} - 1) \frac{\hat{C}_p}{\hat{C}_{p,max}}, \quad (2.28)$$

where  $R_{k,max}$  is the maximum permeability reduction factor,  $\hat{C}_p$  is the in-situ adsorption level ( $gmole/m^3$ ) and  $\hat{C}_{p,max}$  is the maximum adsorption capacity ( $gmole/m^3$ ).

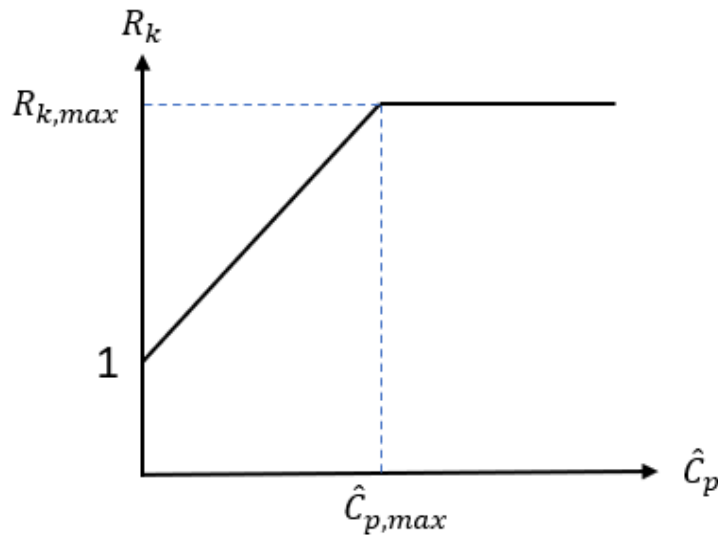


Figure 2.18: The plot of permeability reduction factor versus adsorbed polymer concentration.

# 3

## METHODOLOGY

### 3.1. DARTS SIMULATOR

**I**N this study, the Operator-Based Linearization (OBL) technique [62] developed in Delft Advanced Research Terra Simulator (DARTS) is deployed to handle the nonlinear problem for modeling of polymer flooding. DARTS is developing in DARSim research group since 2017 at Delft University of Technology. The simulator is implemented combining C++ and python, and visualization is exported as vtk file in Paraview. DARTS is a one-of-a-kind, highly customizable and extensible simulation platform, the full details of which are documented in [63].

OBL provides a straightforward linearization strategy that simplifies the construction of the Jacobian matrix and residuals by decoupling the state-dependent operators and the individual extraction of simulation loop and property computation. The reliability of physical representation is manipulated by the property-related block while the simulation loop bears the brunt of the computational load. This approach offers advantages over the shortening of simulation time and the boosting of simulation computational efficiency while also streamline and flexibilize the source code that must be restructured when transforming to a brand-new computational architecture is deemed necessary.

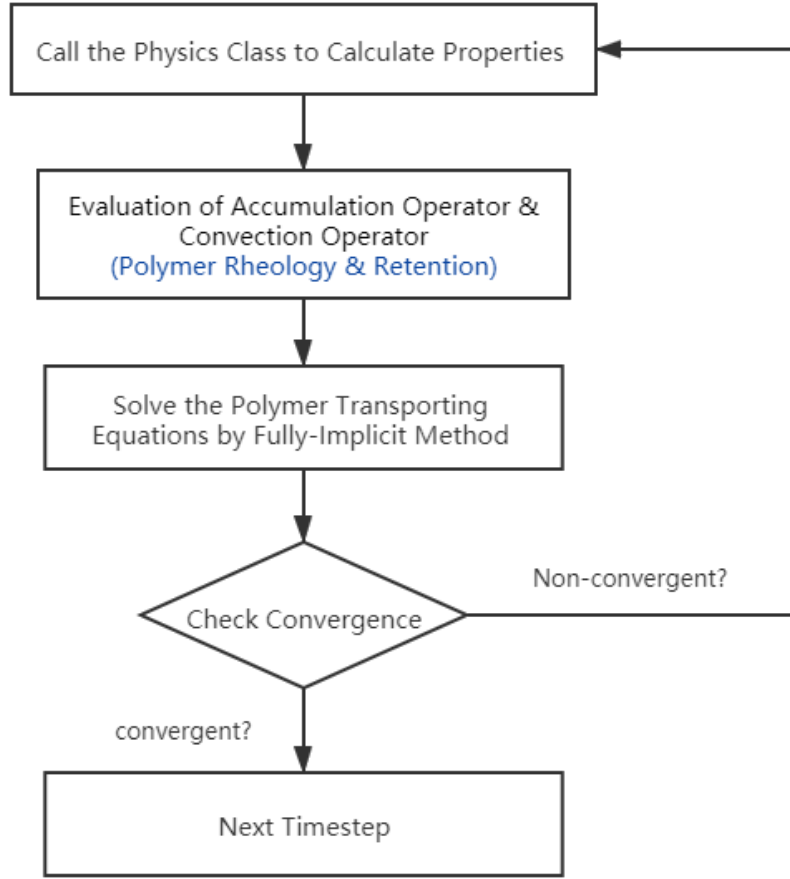


Figure 3.1: A outline of the OBL approach for a single time step is provided. The colored steps were newly implemented for this study.

## 3.2. BASIC CONSERVATION EQUATIONS

THE compositional equations obey the following simplified form of the conservation equation over all phases. The result obeys the mass conservation equation stated as Eq. 3.1 for component  $i$  in volume  $V$

$$(\text{Accumulation rate of } i \text{ in } V) = (\text{Net flow in rate of } i \text{ in } V) + (\text{Source term}). \quad (3.1)$$

The general mass balance equation can be rewritten in Eq. 3.2

$$\frac{\partial}{\partial t} \left( \phi \sum_j x_{cj} \rho_j s_j \right) + \nabla \cdot \sum_j (x_{cj} \rho_j \vec{u}_j) + \sum_j x_{cj} \rho_j \tilde{q}_j = 0, \quad (3.2)$$

where the subscript  $j$  and  $c$  refers to the phases and components respectively,  $x_{cj}$  is the mole fraction of component  $c$  in phase  $j$ . The convection speed of each phase,  $\vec{u}_j$  is described by

Darcy's law (Eq. 3.3)

$$\vec{u}_j = -K_{abs} \frac{k_{rj}}{\mu_j} (\nabla p_j - \rho_j g \nabla D), \quad (3.3)$$

where  $K_{abs}$  is the absolute permeability within the porous media,  $K_{rj}$  is the relative permeability of phase  $j$  which is a given function of saturation, and  $D$  is the reservoir depth.

The goal is to create a three-dimensional numerical model of polymer flooding consisting of aqueous and oleic phases (hereby abbreviated as  $aq$  and  $o$  respectively), and oil, water, polymer components (hereby abbreviated as  $o$ ,  $w$  and  $p$  respectively). In the accumulation term, the mass concentration of each component ( $z_c$ ) and total density ( $\rho_T$ ) would be applied instead of phase saturation and phase density. Hereby, the total density  $\rho_T$  states as a function of phase saturation in Eq. 3.4

$$\rho_T = \rho_{aq} S_{aq} + \rho_o S_o. \quad (3.4)$$

Thereby the mass conservation law of each component is derived as the following series of equations (from Eq.3.5 to Eq.3.7).

Polymer:

$$\frac{\partial}{\partial t} (\phi \rho_T z_p) + \nabla (x_{p,aq} \rho_{aq} K_{abs} \frac{K_{r,aq}}{\mu_{aq}} \nabla p) + x_{p,aq} \rho_{aq} q_{aq} = 0, \quad (3.5)$$

Water:

$$\frac{\partial}{\partial t} (\phi \rho_T z_w) + \nabla (x_{w,aq} \rho_{aq} K_{abs} \frac{K_{r,aq}}{\mu_{aq}} \nabla p) + x_{w,aq} \rho_{aq} q_{aq} = 0, \quad (3.6)$$

Oil:

$$\frac{\partial}{\partial t} (\phi \rho_T z_o) + \nabla (\rho_o K_{abs} \frac{K_{r,o}}{\mu_o} \nabla p) + \rho_o q_o = 0. \quad (3.7)$$

Additional global constraints are required to solve the mass balance equation with all its unknowns as stated in Eq. 3.8, Eq. 3.9, and Eq. 3.10.

(1) Phase-related saturation:

$$s_{aq} + s_o = 1, \quad (3.8)$$

(2) Mass fraction of components:

$$z_p + z_w + z_o = 1, \quad (3.9)$$

(3) Mole concentration of components:

$$\sum_{c=1}^{N_c} x_{c,j} = 1, \quad (3.10)$$

where  $N_c$  is a number of components.

### 3.3. OPERATOR-BASED LINEARIZATION APPROACH

THE expressions of all variables in Eq. 3.11 can be regrouped into product of state-dependent ( $\omega$ ) and space-dependent ( $\xi$ ) operators, keeping in line with the OBL approach. To tackle the given governing equation (Eq. 3.11), the fully-implicit method (FIM) is put into operation. To arrange the terms in residual form, the mass-conservation equation can be discretized by backward Euler

$$R_i(\xi, \omega, u) = a(\xi)(\alpha_c(\omega) - \alpha_c(\omega_n)) - \sum_{l \in L} \beta_{c_j}^l(\omega) b_j^l(\xi, \omega) + \theta_c(\xi, \omega, u). \quad (3.11)$$

Hereby  $\omega$  and  $\omega_n$  are physical states ( $p$  and  $z_c$ ) for a current and previous timesteps, respectively;  $l$  is one of the interfaces in a control volume with  $L$  interfaces.

Considering the possibility of miscible flooding, summation of each phase should be created in a loop with all the phases  $j$  present. The operators that break up the cumbersome nonlinear function are defined as the following set of equations (from Eq. 3.12 to Eq. 3.16)

$$\alpha_c(\omega) = (1 + c_r(p - p_{ref}))z_c\rho_T, \quad (3.12)$$

$$a(\xi) = V(\xi)\phi_0(\xi), \quad (3.13)$$

$$\beta_{c_j}^l(\omega) = \sum_{j=1}^2 x_{c_j} \rho_j \frac{k_{r,j}}{\mu_j}, \quad (3.14)$$

$$b_j^l(\xi, \omega) = \Delta t T_{ab}(\xi)(p^b - p^a), \quad (3.15)$$

$$\theta_c(\xi, \omega, u) = \Delta t \sum_{j=1}^2 x_{c_j} \rho_j q_j(\xi, \omega, u). \quad (3.16)$$

From Eq. 3.12 to Eq. 3.16,  $c_r$  is rock compressibility,  $V$  is the control volume,  $T_{ab}$  is the transmissibility between neighbouring grid-blocks  $a$  and  $b$ , the vector  $u$  comprises variables that are well-controlled,  $\omega$  is the bundle of state-related unknowns and  $\xi$  are the spatial distribution-related variables.

Operators have been distinguished as,  $\alpha_c$ , which is the operator controlling accumulation term,  $\beta_c$ , which is the flux operator controlling convection term and  $\theta_c$ , which is the rate operator. Spatial distributed properties like porosity are stored in operator  $a$  and information related to discretization is stored in operator  $b$ . For a generic isothermal polymer flooding problem with  $n_c$  components and  $n_p$  phases, the approach requires computing  $2n_c + n_p$  operators, whose values

are entirely determined by the set of  $n_c$  independent variables  $p, z_p, z_o$ . The pressure ranges within the bound of injection pressure and producing pressure which are typically dictated by well conditions. The composition over each component is inherently constrained by the upper limit of 1 and the lower limit of 0.

### 3.4. MATHEMATICAL DESCRIPTION OF POLYMER RECOVERY MECHANISM

**T**HE description of the main physical and chemical parameters involved in polymer flooding are given below. In the description, it is usually carried out under the conditions of a reservoir-scale medium, so that the influence caused by the pore-scale structure and properties can be temporarily ignored. The coefficients or parameters in the data sheet and expressions need to be obtained from experimental data. The model takes into account the flow properties of the polymer and the influence of the polymer on the stationary phase.

#### 3.4.1. POLYMER MODULE

##### 3.4.1.1 Polymer Rheology

**Physics Background:** The viscosity of the flowing polymer solution is the direct target of shear rate and shear stress, two principle parameters that typify the rheological features of the system. At a certain temperature (such as reservoir temperature), the viscosity of polymer solution ( $\mu_{aq}$ ) mainly varies with polymer concentration ( $C_p$  [ppm]), and shear rate ( $\dot{\gamma}$  [ $s^{-1}$ ]) as Eq. 3.17

$$\mu_{aq} = \mu_{aq}(C_p, \dot{\gamma}). \quad (3.17)$$

Also expressed as Eq. 3.18

$$\mu_{aq} = \mu_{aq}(\mu_{aq}^0, \dot{\gamma}), \quad (3.18)$$

where  $\mu_{aq}^0$  is viscosity of polymer solution at zero shear rate ( $\mu_{aq}^0 = \mu_{aq}|_{\dot{\gamma} \rightarrow 0}$ ) that depends on  $C_p$ ).

**Numerical strategy:** We deliver an explicit discretization method for addressing the viscosity in polymer flooding, in which the sequential simulation of subproblems is placed outside the entire Newton scheme yet wrapped in the full time loop. See Fig. 3.2, the basic logic is depicted in a streamline flow. To simulate the reservoir robustly, plenty of the publications in the literature adopt fully implicit method (FIM) with a governing equation composed of more variables. This

is ineffective at the vicinity of the wellbore, when shorter computational and physical times are required.

The implementation of the forward Euler algorithm based on the velocity field at previous timestep instead of the implicit methodology, is equipped with short physical time steps between iterations, aiming to slash the computational and increase the robustness and reliability. The flaws in the explicit format are also readily apparent. Although the math is easily-understandable, the timestep size is typically quite limited. The stability and convergence are not as good as the implicit format that does not require the step size.

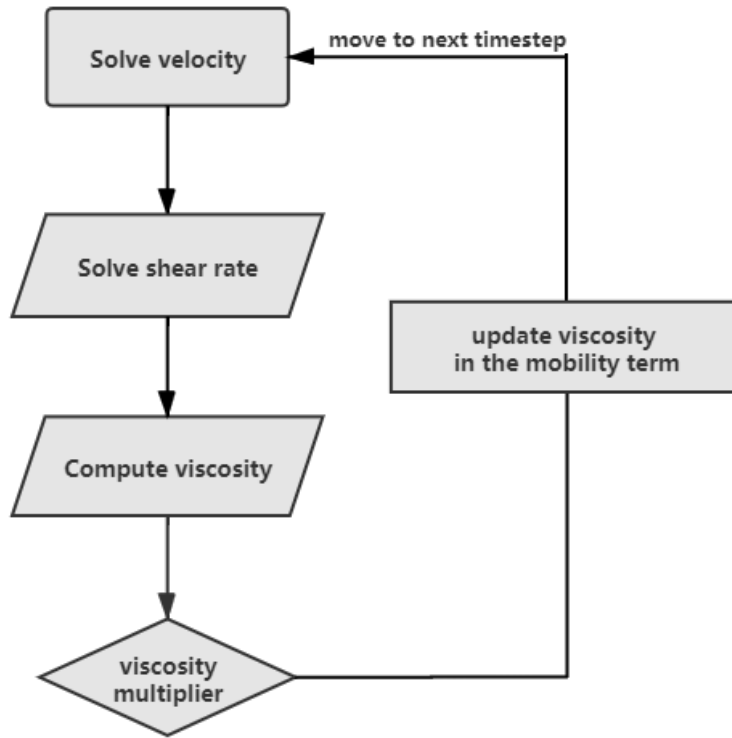


Figure 3.2: Flow chart of viscosity calculation.

- a. Compute  $u_{aq}$  at timestep  $v$  in Eq.3.19

$$u_{aq}^v = -\frac{k_{abs}k_{r,aq}^v}{\mu_{aq}^0 M^v} \nabla p^v. \quad (3.19)$$

Here the state-dependent properties  $k_{r,aq}^v$ ,  $\mu_{aq}^0$  and  $M^v$  and spatial variable ( $\nabla p$ ) are all calculated in  $v_{th}$  timestep,  $M$  is a array of viscosity multiplier, defined in Eq. 3.23.

b. Compute  $\dot{\gamma}$  and  $\mu_{aq}^{0 \ v}$  in Eq. 3.20

$$\dot{\gamma}^v = C \left( \frac{3n+1}{4n} \right)^{\frac{n}{n-1}} \frac{u_{aq}^v}{\sqrt{K k_{r,aq}^v S_{aq}^v \phi}}. \quad (3.20)$$

Here  $u_{aq}^v$  and  $k_{r,aq}^v$  are the Darcy velocity and relative permeability of aqueous phase respectively,  $S_{aq}^v$  is the aqueous saturation, and  $C$  is the shear correction factor. When  $C$  is equal to 6, it is claimed that the Eq. 3.20 matches a wide variety of core flood data. The zero-shear viscosity can be expressed in Eq.3.21

$$\mu_{aq}^{0 \ v} = \mu_w (1 + (a_1 C_p^v + a_2 C_p^{v2} + a_3 C_p^{v3}) C_{SEP}^{SP}), \quad (3.21)$$

where  $\mu_w$  is the water viscosity;  $a_1$ ,  $a_2$ ,  $a_3$  and  $S_p$  are coefficients obtained from experiments.

c. Compute  $\mu_{aq}^v$  at timestep  $v$  based on Eq. 3.22

$$\mu_{aq}^v = \mu_w + (\mu_{aq}^{0 \ v} - \mu_w) [1 + (\lambda \dot{\gamma}^v)^2]^{\frac{n-1}{2}} + \mu_{max} [1 - \exp(-\lambda_2 \tau_r \dot{\gamma}^v)^{n_2-1}]. \quad (3.22)$$

where the 8-parameter Delshad's model [49], captures the Newtonian plateaus at low, shear-thinning behaviour at intermediate shear rates, and shear-thickening uplift at high shear rate. The other elements are all constant parameters exclusive of the only variable  $\dot{\gamma}$ .  $\mu_{aq}^{0 \ v+1}$  and  $\mu_{aq}^{0 \ v}$  are the polymer viscosity under apparent and zero shear rate, respectively,  $\mu_w$  is viscosity of water,  $\lambda$ ,  $n$ ,  $n_2$ ,  $\lambda_2$ ,  $\mu_{max}$  and  $\tau_r$  are experiment fitted constants from laboratory.

d. Compute  $M$  at timestep  $v$  (Eq. 3.23). Viscosity multiplier is defined as a ratio of apparent viscosity at timestep  $v+1$  to the zero shear-rate viscosity at timestep  $v$  as Eq. 3.23. The  $M$  is set to be 1 as the original state, namely 0 timestep

$$M^v = \frac{\mu_{aq}^v}{\mu_{aq}^{0 \ v}}. \quad (3.23)$$

e. Update the  $u_{aq}$  at timestep  $v+1$  employing Eq. 3.24

$$u_{aq}^{v+1} = - \frac{k_{abs} k_{r,aq}^{v+1}}{\mu_{aq}^{0 \ v+1} M^v} \nabla p^{v+1}. \quad (3.24)$$

As the simulation keeps iterating, the zero-shear viscosity at the current step will be updated by multiplying with the viscosity multiplier in previous timestep.

### 3.2.1.2 Polymer Retention Model

The level of polymer retention in porous media depends on (a) the type of polymer and the specific properties of the molecule (HPAM or xanthan, molecular weight, hydrodynamic size, charge density), (b) the solvent conditions (pH, salinity, hardness, temperature) and (c) the surface chemistry of the adsorbing substrate (silica sand, clay, sandstone, carbonate).

#### Adsorption Rate:

A Langmuir isotherm is the most common type in the polymer flooding simulators of great abundance [26]. Langmuir makes the assumption of a uniform surface of the adsorbent, and the energy of adsorption is equal in all the spots. Monolayer adsorption is expected, that is, as soon as the adsorbent surface is saturated with adsorbates maximum adsorption capacity will be reached. Whereby, the adsorbed concentration of polymer is given by a function of polymer concentration as Eq. 3.25

$$C_a = \min\left(C_p, \frac{aC_p}{1 + bC_p}\right), \quad (3.25)$$

where  $C_p$  and  $C_a$  [ $g/m^3$ ] are the polymer concentrations flowing at the pores and trapped on the stationary phases, with the units in wt%. The placement of minimum in Eq. 3.25 is taken to guarantee the mass balance in case the adsorption amount (2nd term) surpasses the injected polymer amount (1st term) after 100% saturation. The Langmuir's coefficient  $a$  and  $b$  is specified input coefficients fitted from the experiments, which vary with the salinity and permeability change. But the effect of ions and permeability is not going to be discussed in this project.

#### Porosity Treatment:

In order to accurately treat interphase transfer between flowing and stationary phase at the continuous level, the treatment of the rock porosity should be carried out. The control volume (also known as bulk volume) is ordinarily split into two sections: void space (which encompasses all mobile phases: aqueous and oleic) and superficial solid skeleton (consisted of film-like immobile species where polymer is adsorbed).

Using the density of the polymer as a bridge, the adsorption concentration can be converted to volume of the adsorbed polymer and update the porosity as following Eq. 3.26

$$\phi_{new} = \phi_{ini} - \frac{aC_p(1 - \phi_{ini})}{(1 + bC_p)\rho_p}, \quad (3.26)$$

where  $\phi_{ini}$  is the post-compressed porosity at subsurface pressure,  $C_p$  is the flowing polymer concentration,  $\rho_p$  is the polymer density.

The another fraction of total pore volume known as *IPV* (Inaccessible Pore Volume), which is not available for polymer penetration due to its size and exclusion of the wall, had to be taken account in this case. At the opposite end, the polymer spreads in a higher speed than other components under the same injection rate, since the reservoir rock's effective porosity in relation to polymer components is lower than its effective porosity in relation to other components.

With the exception of water and oil, the porosity in the mass conservation equation should be corrected especially for polymer by the effective pore volume fraction ( $\phi_e$  as an input constant as a ratio of *APV*(Accessible Pore Volume) and original porosity), which states as Eq. 3.27 and Eq. 3.28

$$\phi_e = APV/\phi, \quad (3.27)$$

$$\frac{\partial}{\partial t} (\phi\phi_e\rho_T z_p) + \nabla(x_{p,aq}\rho_{aq}K_{abs}\frac{K_{r,aq}}{\mu_{aq}}\nabla p) + x_{p,aq}\rho_{aq}q_{aq} = 0. \quad (3.28)$$

Next, the piece-wise operators need to be adjusted by a porosity multiplier. The revised version is tabulated in Table. 3.1:

Table 3.1: Extensions of Operator-Based Linearization adapted to polymer flooding.

Components	Alpha Operator	Beta Operator
Polymer	$(1 + C_r(p - p_{ref}))z_p\rho_T\phi_{new}\phi_e/\phi_{ini} + \rho_p(\phi_{ini} - \phi_{new})\phi_e/\phi_{ini}$	$x_{p,aq}\rho_{aq}k_{r,aq}/\mu_{aq}$
Oil	$(1 + C_r(p - p_{ref}))z_o\rho_T$	$\rho_o k_{r,o}/\mu_o$
Water	$(1 + C_r(p - p_{ref}))z_w\rho_T$	$x_{w,aq}\rho_{aq}k_{r,aq}/\mu_{aq}$

### Permeability Reduction:

The decrease in permeability is believed to be owing to the shrinking of the effective size of the pores caused by adsorption and retention of the polymer molecular coils. In order to define the permeability reduction quantitatively, two dimensionless quantities, the permeability reduction factor ( $R_k$ ) and the residual resistance factor ( $R_{rf}$ ) which primarily act on the aqueous phase has been formulated.  $R_k$  is the ratio of effective permeability of aqueous phase before and after polymer injection.  $R_{rf}$  stands for the ratio of the size of the polymer molecular coil to the effective pore diameter of the porous medium, which is formulated to correlate the reduction of permeability with rock properties [59].

Under the presumption of irreversible scenario of polymer adsorption the  $R_{k,max}$  and  $R_{rf}$  are

the almost equal, as stated in Eq. 3.29

$$R_{k,max} \simeq R_{rf}. \quad (3.29)$$

The permeability reduction factor is linearly proportional to the degree of polymer adsorption, and both of the two climb to a max amount all together as shown in Eq. 3.30

$$R_k = 1 + (R_{k,max} - 1) \frac{\hat{C}_p}{C_{p,max}}. \quad (3.30)$$

Where  $R_{k,max}$  is the maximum permeability reduction factor,  $\hat{C}_p$  is the adsorbed level of polymer ( $gmole/m^3$ ) and  $C_{p,max}$  is the maximum adsorption capacity ( $gmole/m^3$ ).

For a homogeneous capillary-tube model (regardless of the anisotropy of permeability), the permeability change is analogous to the reduction of the capillary radius on the basis of the Hagen-Poiseuille law, which is derived as Eq. 3.31

$$R_{k,max} = \min \left( \left[ 1 - \frac{c_{rk} [\mu_p]^{\frac{1}{3}}}{\frac{k^{\frac{1}{2}}}{\phi}} \right]^{-4}, rkcut \right), \quad (3.31)$$

where  $c_{rk}$  is the input parameter obtained from laboratory,  $[\mu_p]$  is the intrinsic polymer viscosity and  $rkcut$  acts as the upper bound of permeability reduction.

As an additional parameter to lower mobility besides viscosity increase, the viscosity of aqueous phase will be multiplied by  $R_k$  to involve the effect of channel blocking during the simulation.

### 3.4.2. FLUID & ROCK PROPERTIES

#### 3.4.2.1 Compressibility of flowing and stationary phase

The compressibility of each phase is defined in Eq. 3.32

$$C_j = -\frac{1}{v_j} \frac{dv_j}{dp} = \frac{1}{\rho_j} \frac{d\rho_j}{dp}. \quad (3.32)$$

Since it is an isothermal model, the densities of specific components (water and oil) are only considered as a function of pressure. The measured curve of  $\rho_i-p$  can be directly given as Eq. 3.33

$$\rho_i = \rho_i(p). \quad (3.33)$$

Only retaining the first two terms of the Taylor series of exponential function comes to Eq. 3.34 and Eq. 3.35

$$\rho_i = \rho_i^0 e^{C_i(p-p_0)} = \rho_i^0(1 + C_i(p - p_0)), \quad (3.34)$$

$$\rho_j^0 = \sum_i^{nc} x_{ij} \rho_i^0. \quad (3.35)$$

Here  $\rho_i$ ,  $\rho_i^0$  are the component densities corresponding to the in-situ pressure  $p$  and reference pressure  $p_0$  respectively;  $x_{ij}$  is the molar fraction of the components in each phase;  $\rho_j^0$  is the density of the phase  $j$  at the pressure  $p$ .

Similarly, the porosity of the reservoir under rock compression factor  $C_r$  can be expressed in Eq. 3.36

$$\phi = \phi^0 e^{C_r(p-p_0)} = \phi^0(1 + C_r(p - p_0)), \quad (3.36)$$

where  $\phi$ ,  $\phi^0$  are the rock porosities corresponding to the pressures  $p$  and  $p_0$  respectively.

### 3.4.2.2 Relative Permeability Model

Relative permeability is a function of water saturation. Two options to input relative permeability data are available in DARTS: 1) table lookup, and 2) function calling. The table of relative permeability data over the saturation range of  $(S_{wr}, 1 - S_{or})$  is given in the input file. During the initialization, an array is then generated to store data calculated by specified interpolation scheme (linear). Table-lookup is efficient and robust, though it has one down side: when the porous media is of high heterogeneity, multiple tables corresponding to different lithologies may be expected. At the first stage without specific geological benchmark, we implemented a two phase Brooks-Corey model in DARTS. The imbibition relative permeability curve for water/oil flow is given by Eq. 3.37

$$k_{r\alpha} = k_{r\alpha}^0 (S_{n\alpha})^{n_\alpha}, \quad \alpha = aq, o, \quad (3.37)$$

where  $k_{r\alpha}$  is the relative permeability endpoint for phase  $\alpha$ ,  $n_\alpha$  is the relative permeability exponent, and  $S_{n\alpha}$  is the normalized phase saturation defined by Eq. 3.38

$$S_{n\alpha} = \frac{S_\alpha - S_{\alpha r}}{1 - S_{wr} - S_{or}}, \quad \alpha = w, o. \quad (3.38)$$

Here  $S_{wr}$  and  $S_{or}$  are residual water and oil saturations respectively.  $k_{r\alpha}^0$ ,  $n_\alpha$ ,  $S_{wr}$  and  $S_{or}$  are input parameters for Brooks-Corey model.

### 3.4.3. WELL MODULE

The flow equations treat injection and production wells as source or sink terms. A connection-based well module is established where the transmission between well blocks and reservoir blocks is processed in the same way as between reservoir blocks. Along these lines, wells can be completed vertically in multi-segments of the reservoir and can be controlled via pressure or rate constraints. In this model, BHP control is implemented by fixed injection and production pressure. In order to maintain target pressure  $p^{target}$ , the following series of equations (Eq. 3.39, Eq. 3.40 and Eq. 3.41) is applied to the  $w_0$  control volume (the top well head)

$$p - p^{target} = 0, \quad (3.39)$$

$$z_c - z_c^t = 0, \quad c = 1, \dots, n_c - 1, \quad (3.40)$$

$$z_c^t = \begin{cases} z_c^{inj} & \text{for injector} \\ z_c^{w_1} & \text{for producer.} \end{cases} \quad (3.41)$$

Here  $w_1$  is the well control volume connecting with the ghost control volume  $w_0$  and the reservoir volume.

# 4

## RESULTS

In this chapter we conduct research into the physical phenomena in order to replicate a more realistic image of polymer flooding. A comparison between various circumstances is performed to analyse what effect of each variable is on the polymer flooding. For clarity, we offer the research in the form of a basic 1D conceptual flooding model. In this setup the injection well to the left and production well to the right are regulated by the bottom-hole pressure (BHP).

### 4.1. TWO-PHASE FLOW IN TERTIARY SYSTEM

**W**E start from conventional two-phase flow in tertiary system representing water, oil and polymer component. Hereby only viscosity dependency of water phase based on polymer concentration is considered. From the images in Fig. 4.1, there is clear dependency of polymer concentration and shock positions for components. In contrast, the tertiary system's compositional profiles at the injected concentration of  $1e^{-12}$  are identical to that of the binary system in Fig. 4.2.

This results make sense in terms of numerical theory and physical significance. When the viscosity of injecting fluid ascends, the mobility ratio will go up accordingly. Hence, owing to the larger denominator, the water fraction will drop, resulting in a decrease in the derivative (i.e.  $df_w/dS_w$  as well as the dimensionless velocity (i.e.  $dx_D/dt_D$ ). Moreover, slicing through diagram at fixed time ( $t_D$  is constant),  $dx$  becomes larger due to the higher speed of propagating saturation. On the other hand, from the physical standpoint, if more viscous flooding substance

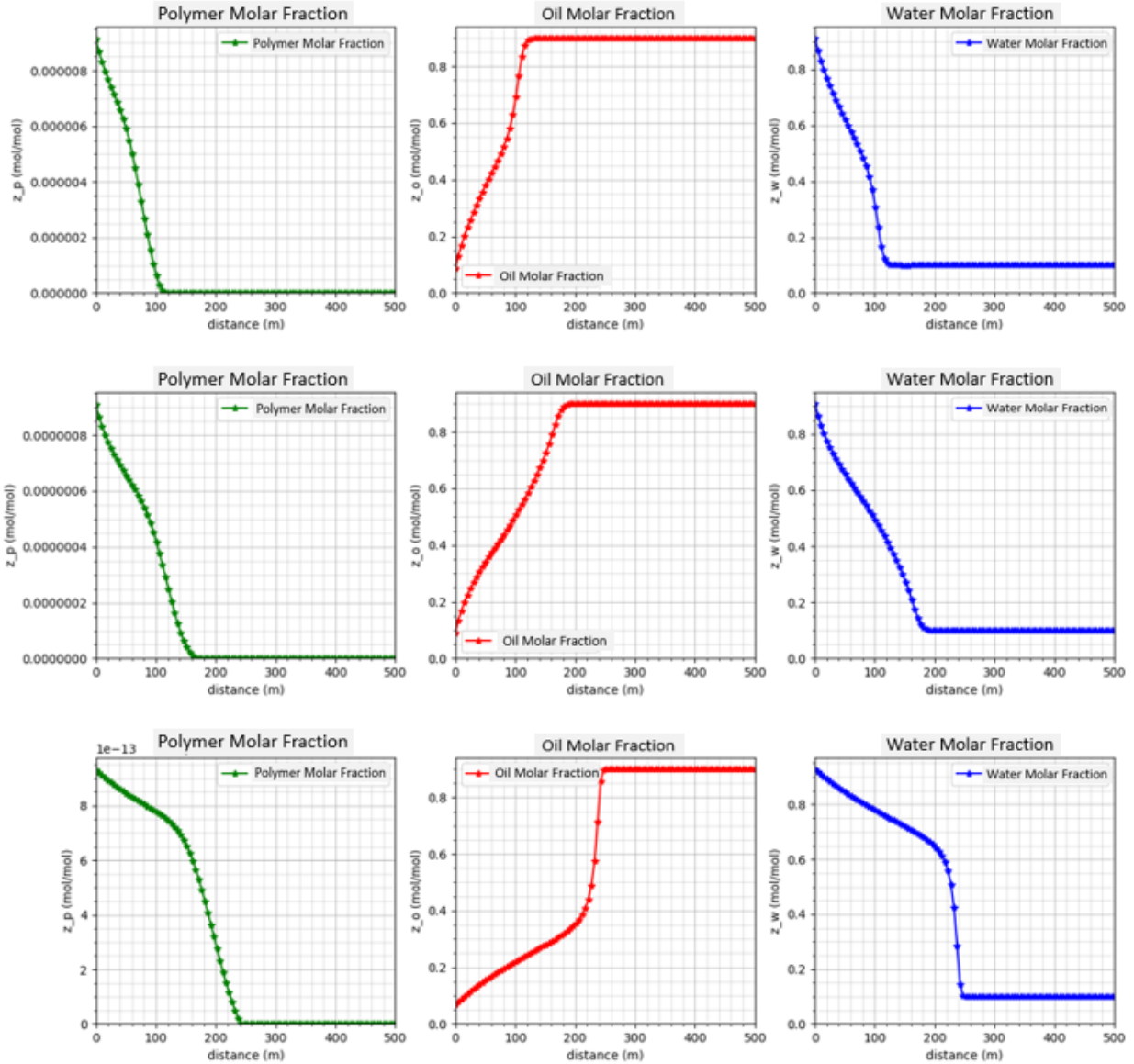


Figure 4.1: The molar fraction profiles of polymer (in green), oil (in red) and water (in blue) are plotted after 400 days and at different injected polymer concentration. The first, second and third row are at concentration of  $1e^{-5}$  mol/mol,  $1e^{-7}$  mol/mol and  $1e^{-12}$  mol/mol.

is chosen, the mobility of water phase will occupy less position in total mobility, which accelerate the shocking speed to a large extent. The aftermath is that while displacement efficiency will be considerably improved, sweeping efficiency will be adversely affected if large viscosity differences occur between the displacing and displaced fluids.

## 4.2. SHEAR-THINNING

**T**HE shear rate in the simulation is far from reaching the critical value for shear thickening since its magnitude is even less than  $10 \text{ s}^{-1}$ . Thus in the following rheological numerical simulations, only the phenomenon of shear thinning can be captured and fixed attention to.

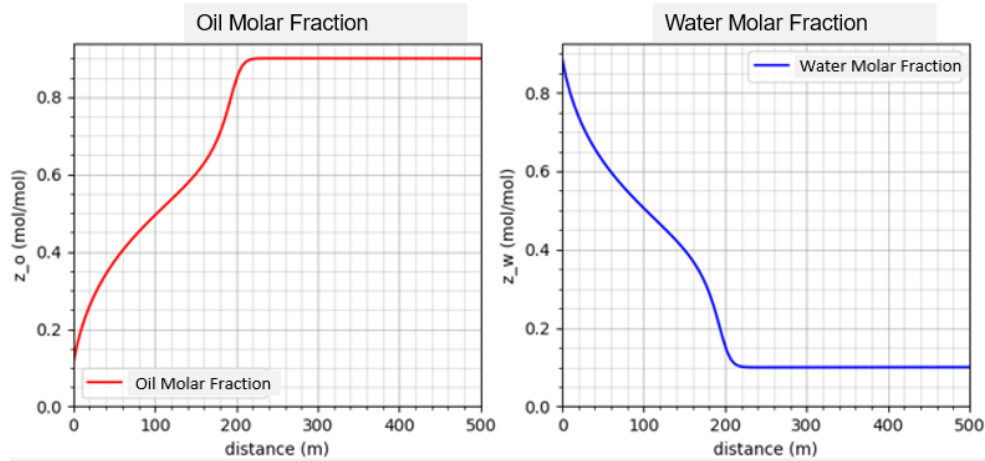


Figure 4.2: The propagation of oil molar fraction (the left) and water molar fraction (the right) in binary system after 400 days.

### 4.2.1. EFFECT OF INJECTED POLYMER CONCENTRATION

Fig. 4.3 transfers the mole concentration of polymer (mol/mol) into mass concentration (ppm), which is the key unit that dominated the polymer-related computation. The effect of injected polymer concentration on zero shear viscosity can be perceived intuitively. The zero-shear viscosity curve is basically consistent with the polymer concentration distribution, and both have witnessed a flattening at the front end, a sharp drop in the middle and then another flattening after hitting the minimum. Comparing the rheological curve of Fig. 4.4 (b) to Fig. 4.3, it is discovered that the first stage of the viscosity curve is flat, and the second stage of the sharp drop is slightly shorter than the composition curve. This is because the terms limited with an exponent of less than three have been chosen in the Eq. 3.21. The quadratic term will bring about the early appearance and a faster rate of decline of the second stage, in addition to the simple linear relationship led by the first term.

For the purpose of facilitating the comparison of the effect of shear thinning caused by shear rate, a viscosity reduction factor has been proposed, which is defined as the ratio of the difference between zero-shear viscosity and solvent viscosity to the difference between apparent viscosity and solvent viscosity. At lower shear rates, the shear force is too small to break the entanglements, but at this time the viscosity reduction factor is the largest, indicating that the thinning effect of the shear rate has been taken to extremes. As the shear rate rises rapidly to the plateau and remains still, polymers are entirely disentangled and the viscosity plateaus at the infinite shear viscosity, at which time the viscosity reduction factor touches the bottom implying the ignorable effect of the shear rate on lessening viscosity. The abovementioned performance in viscosity reduction

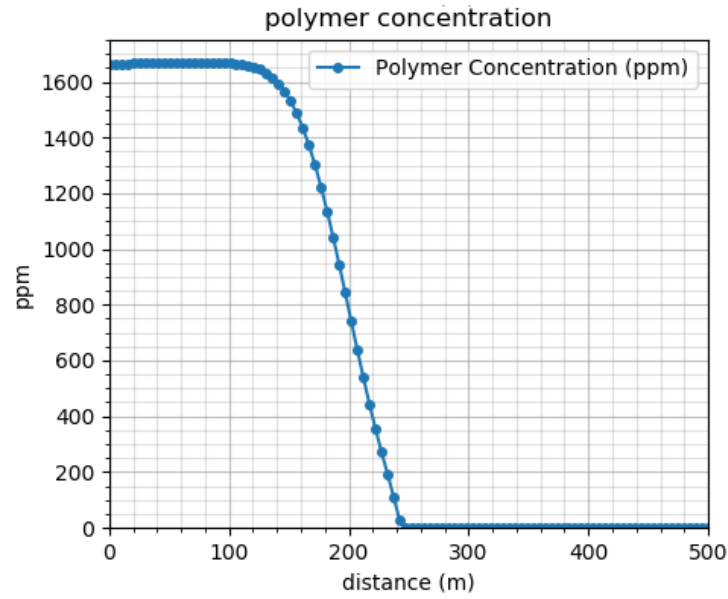


Figure 4.3: Polymer concentration throughout the porous media after 400 days when a polymer with a concentration of 1664 ppm ( $1e^{-8}$  mol/mol) is introduced.

factor is compatible with Eq. 2.19 as the shear rate is inversely proportional to the multiplier of  $(1 + (\lambda\dot{\gamma})^2)^{\frac{n-1}{2}}$ .

Reading Fig. 4.4 from left to right, it can be seen that the injecting polymer concentration impacts the magnitude of zero-shear viscosity and apparent viscosity as well as the propagation length of the shear-thinning in the porous medium. The thickening effect becomes more prominent as the polymer concentration rises. Adversely, the higher the polymer concentration, the slower the displacement rate becomes.

#### 4.2.2. EFFECT OF PLUGGING LOCATION

The surge in zero-shear viscosity and apparent viscosity attributes to the soaring concentration of the middle section, as shown in the Fig. 4.5. As a result of the excessively high polymer concentration, the mobility ratio of the aqueous phase in the middle section falls, the displacing speed and shear rate comes down, whereas the thinning level of viscosity goes up. Correspondingly, an increase in the viscosity reduction factor indicates that the peak of shear-thinning degree, which also suggests that the valley of viscosity multiplier has been reached.

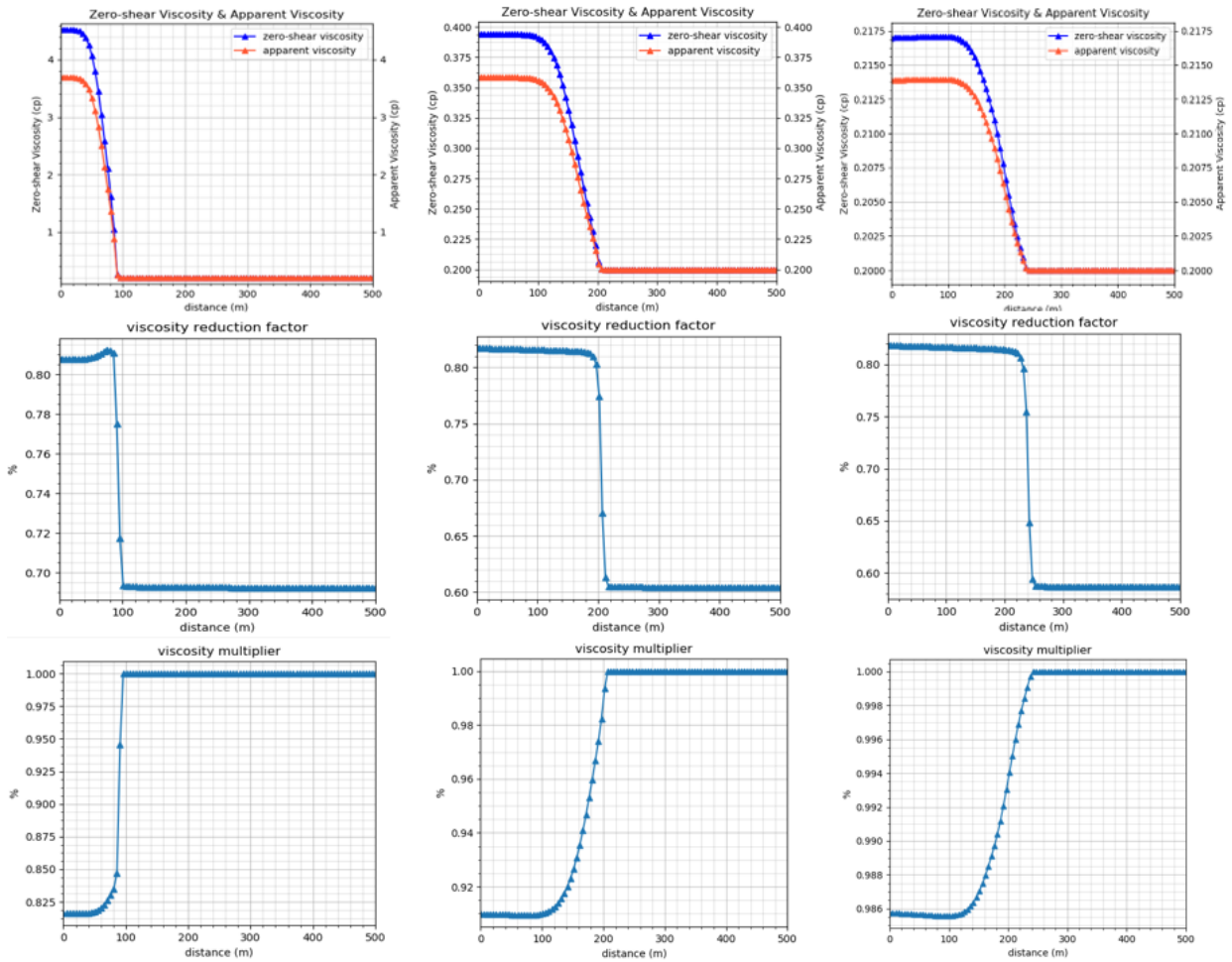


Figure 4.4: The zero-shear viscosity (in blue) and apparent viscosity (in red) of polymer solution after 400 days is plotted in the first row. The viscosity reduction factor and viscosity multiplier are plotted in the second and the third row respectively with the polymer being injected at the injection well. Different injected polymer concentration of a) 16441 ppm ( $1e^{-7}$  mol/mol), b) 1664 ppm ( $1e^{-8}$  mol/mol), and c) 166.4 ppm ( $1e^{-9}$  mol/mol) serves as the only variable.

### 4.2.3. EFFECT OF TIME DURATION

By implementing the slug method of polymer injection in between the injection and production well, the impact of time on polymer flooding can be distinguished conspicuously. As time passes, while the spike continues to move to the right with the displacement, the wave shifts to a more and more smooth form with its width expanding and amplitude shrinking. The viscosity reduction factor and viscosity multiplier exhibit the same trend (see Fig. 4.6). The bulge of the viscosity reduction factor faded over time, and finally integrated with the ambient curve at 800 days.

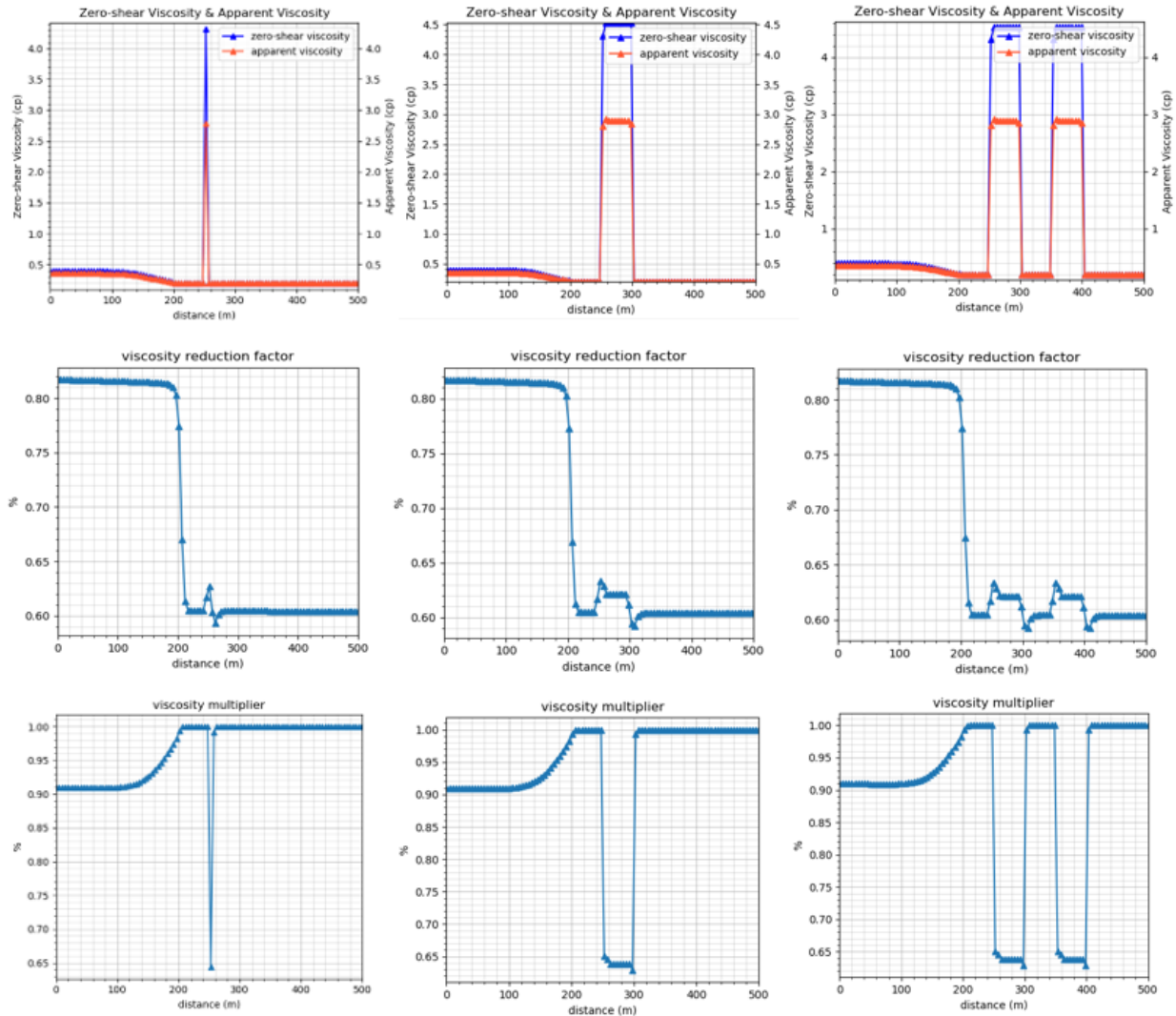


Figure 4.5: The zero-shear viscosity (in blue) and apparent viscosity (in red) of polymer solution after 400 days is plotted in the first row and the corresponding viscosity reduction factor and viscosity multiplier are plotted in the second and the third row respectively at injected polymer concentration of 1664 ppm ( $1e^{-8}$  mol/mol). Different plugging treatment is controlled as the only variable, which is injecting in the a) middle point (250m), b) one ten-meter-long section (250-300m), and c) two ten-meter-long section (250-300m and 350-400m).

### 4.3. POLYMER RETENTION

**T**HE polymer retention affects the polymer levels in the flux phase, reducing the effective polymer flood concentration considerably. At the same time, the polymer attached to the rock surface influences porosity, which will be explored further in the following analysis.

#### 4.3.1. EFFECT OF INJECTED POLYMER CONCENTRATION

The first sensitivity factor is injected polymer concentration, which is tightly bound up with the adsorbed polymer concentration and the physical properties of the porous medium. Fig. 4.7 ren-

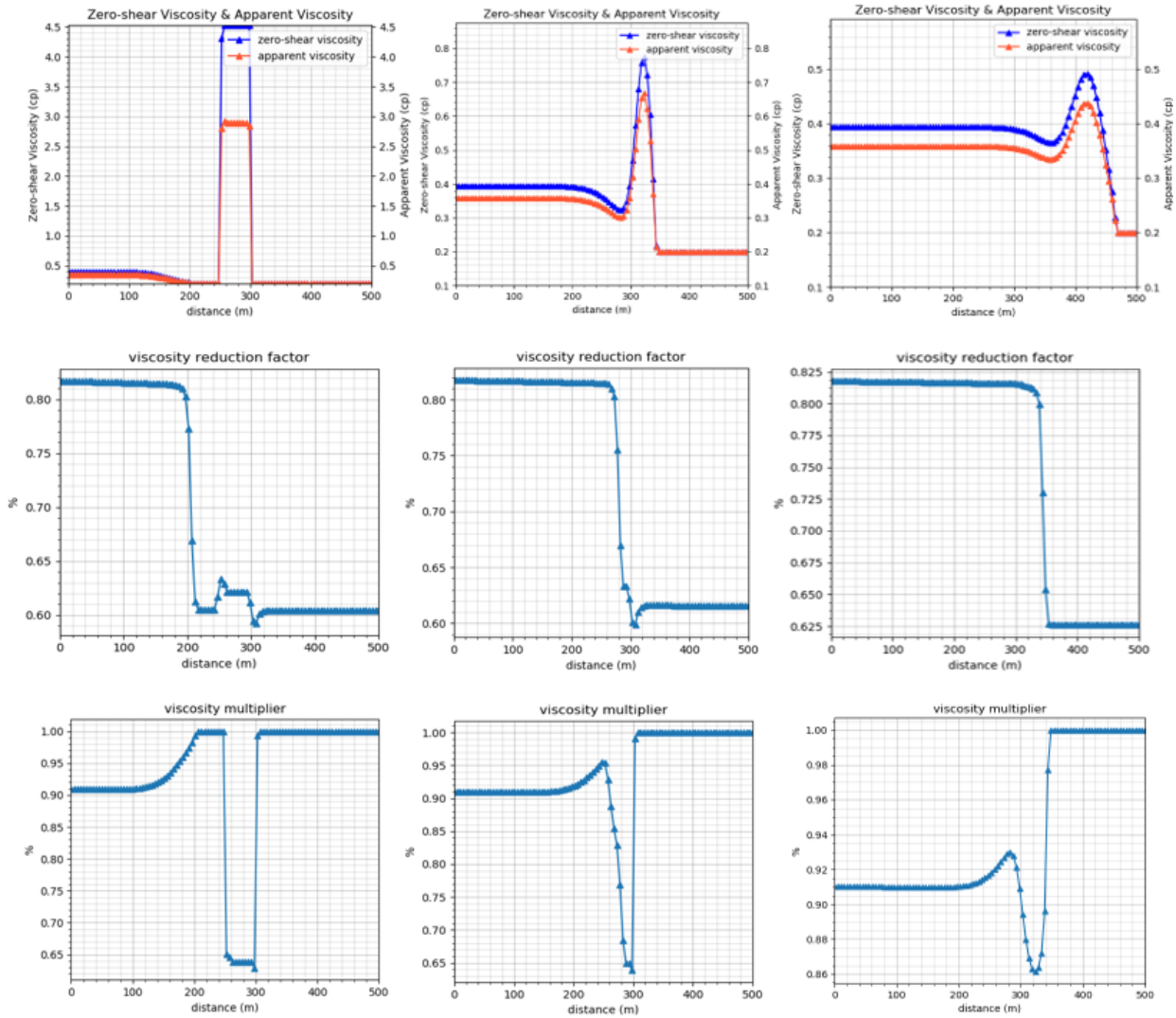


Figure 4.6: The zero-shear viscosity (in blue) and apparent viscosity (in red) of polymer solution is plotted in the first row and the corresponding viscosity reduction factor and viscosity multiplier are plotted in the second and the third row respectively at injected polymer concentration of 1664 ppm ( $1e^{-8}$  mol/mol). Hereby plugging along a ten-meter-long section (250-300m) is selected as a sample. The only variable initiated is the timespan, lasting for a) 400 days, b) 600 days, and c) 800 days.

ders the results that when the injected polymer concentration amounts to 1664 and 16.6 ppm, the adsorbed polymer concentration remains the same, which evinces that the polymer concentration has exceeded the critical value to make the rock surface saturated. But when the polymer concentration is 0.166 ppm, the leveling-off period at the beginning has disappeared and a much smaller amount of adsorption is replaced. At this time, the curves of polymer concentration and the adsorbed concentration almost coincide, indicating that the current state has not yet reached saturation.

To visualize the effect of polymer retention on porosity, we bring in a porosity reduction factor, defined as the ratio of porosity reduction over the original porosity. Take the porosity reduction

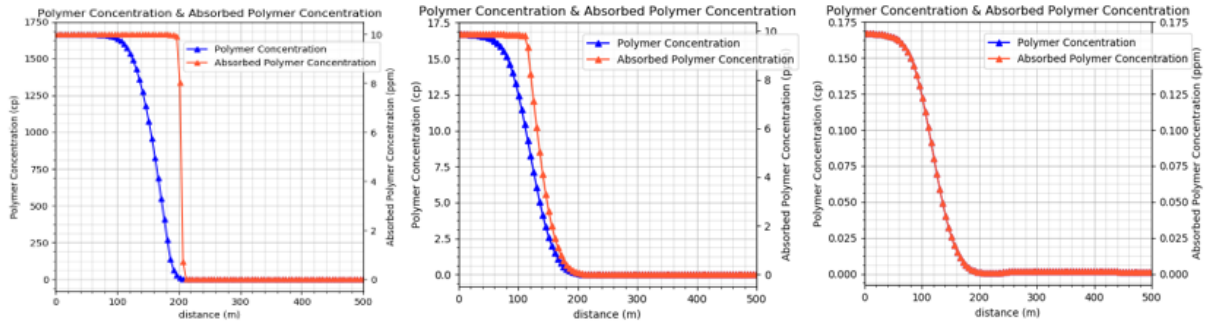


Figure 4.7: Polymer concentration and adsorbed polymer concentration versus distance after 400 days when a polymer with a concentration of a) 1664 ppm ( $1e^{-8}$  mol/mol), b) 16.6 ppm ( $1e^{-10}$  mol/mol), and c) 1.66 ppm ( $1e^{-12}$  mol/mol) is introduced. The upper bound of polymer retention is set to be 10, with a and b set to be 50 and 5, respectively.

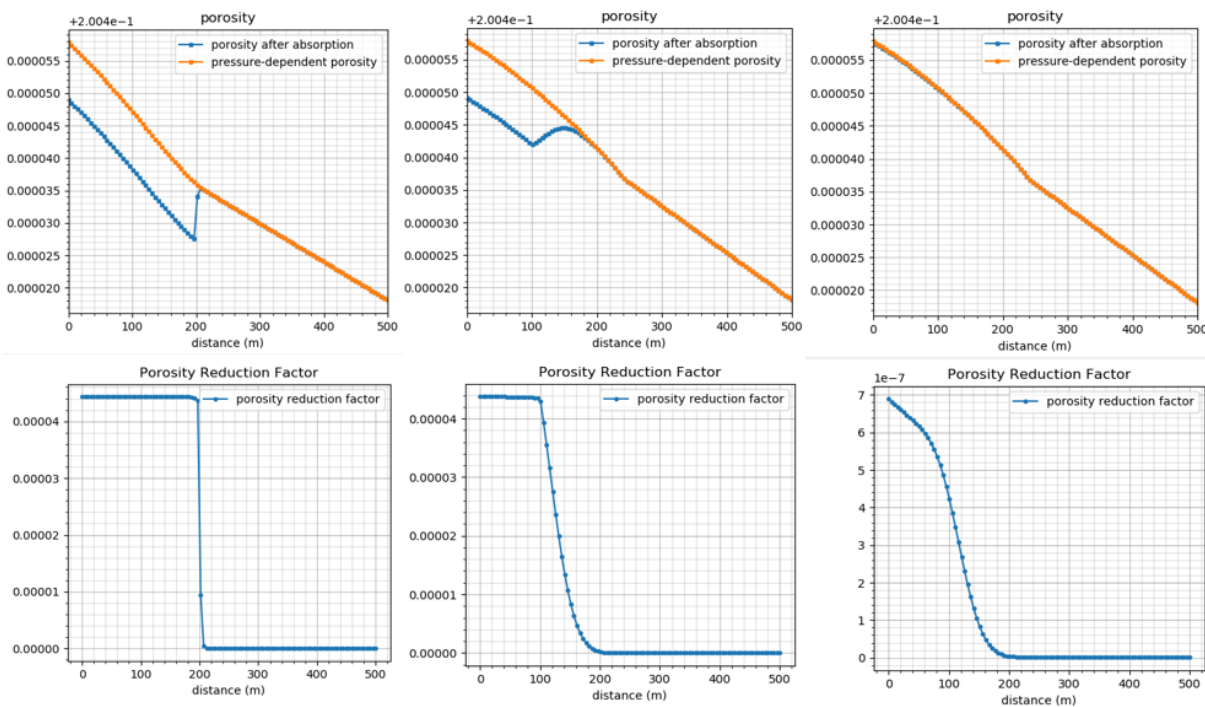


Figure 4.8: The porosity after adsorption (in blue) and original porosity (in red) in compressible porous media after 400 days is plotted in the first row. The porosity reduction factor is plotted in the second row with the polymer being injected at the injection well. The upper bound of polymer retention is set to be 10, with a and b set to be 50 and 5, respectively. Different injected polymer concentration of a) 1664 ppm ( $1e^{-8}$  mol/mol), b) 16.6 ppm ( $1e^{-10}$  mol/mol), and c) 1.66 ppm ( $1e^{-12}$  mol/mol) serves as the only variable.

curve for example, when injecting 1664 ppm polymer, the upper bound of polymer retention is reached at the beginning, followed by a sharp plunge until it comes to zero. Coupling the three developing stages of porosity can harvest an interpretation from a physical point of view (see Fig. 4.8):

- The first stage presents a marginal decrease of apparent porosity which is in tune with the constant line in the adsorbed concentration. In this stage, despite the flowing polymer concentration drops in a big scale, the adsorbed concentration experiences a small scale de-

crease and still approaches to the upper bound;

- The second stage is a rapid climbing of porosity, corresponding to the sudden jump in the adsorbed concentration. During this stage, less and less percentage of polymer can flow and more and more percentage of polymer is retained;
- The third stage takes place as all of the polymer is retained in a undersaturated stage with no further change.

By contrast of the different strategies of polymer flooding, the porosity reduction factor is found to increase as the injected polymer concentration increases. This outcome matches both the conceptual mathematical model and the experimental data.

#### 4.3.2. EFFECT OF TIME DURATION

As the simulation moves forward in time, the polymer accounts for more and more percentage of the voids, so that more and more pores have been fully saturated, achieving the minimum porosity and afterwards staying stable (see Fig. 4.9). Simultaneously, the second phase contains an increasing number of interpolation points, thus the length of intermediate zone expands. This is due to the fact that as time passes, the shock front has been smeared out, resulting in an elevation in the quantity of pores between the fully saturated concentration and the zero concentration after the shock.

#### 4.3.3. EFFECT OF UPPER BOUND OF POLYMER RETENTION

##### **a/b increasing, b constant**

It can be seen from the Fig. 4.10 that the porosity curves before and after adsorption in the completely-adsorbed region are getting farther and farther away from each other. With higher upper limit of adsorption, the upper boundary of polymer retention has been heightened. In parallel, the porosity reduction factor rises from  $1e^{-6}$  to  $1e^{-4}$  as the maximum adsorbed concentration is amplified from 1 to 100.

##### **a/b constant, b increasing**

As is depicted in Fig. 4.11, the smaller the value of  $b$ , the smaller the porosity reduction factor, which provides a picture of the partial-saturated situation of polymer. When  $b$  is set to be larger and gradually close to infinity, the porosity reduction factor at the injection end approaches 0.0007,

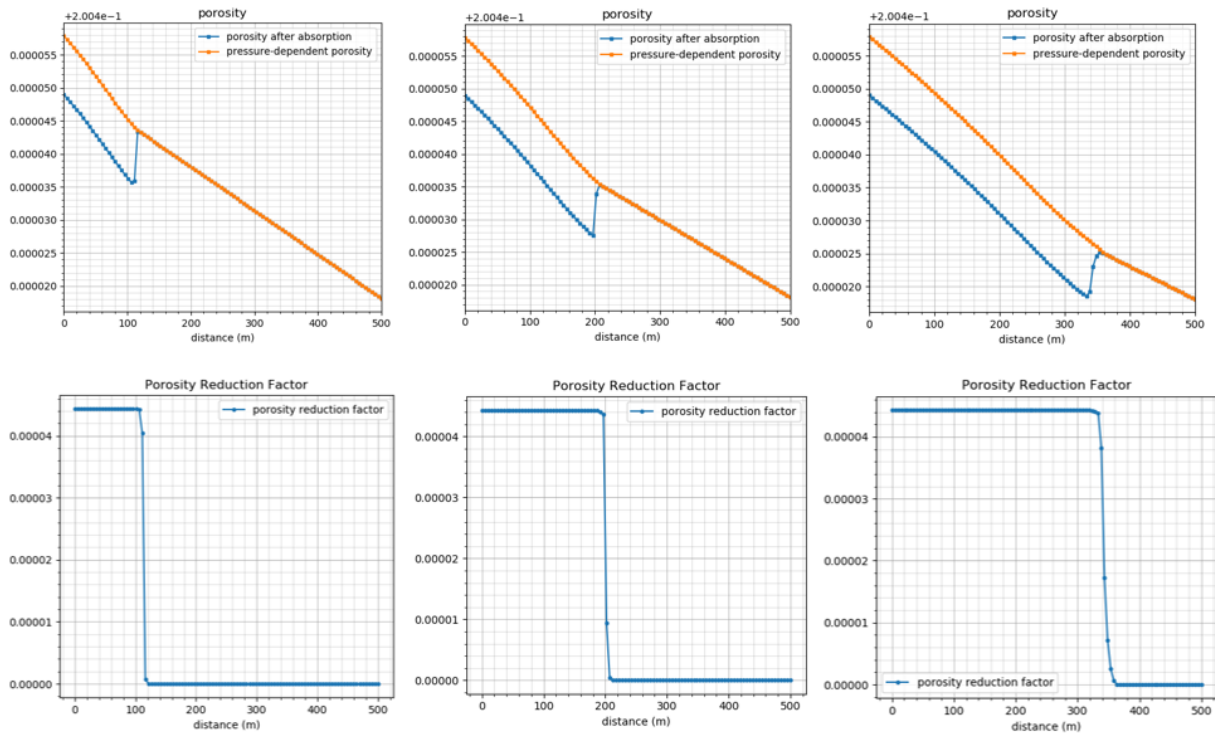


Figure 4.9: The porosity after adsorption (in blue) and original porosity (in red) in compressible porous media is plotted in the first row. The porosity reduction factor is plotted in the second row with the polymer being injected at the injection well at a concentration of 1664ppm ( $1e^{-8}$ mol/mol). The upper bound of polymer retention is set to be 10, with a and b set to be 50 and 5, respectively. A time period of a) 400 days, b) 600 days, and c) 800 days are only variable initiated.

which portrays the fully-saturated state. All the evidence justifies a conclusion that even though the upper bound is the same in all three scenarios, the value of  $b$  makes a difference.

From a mathematical standpoint, this reproduces the graphs in Fig. 2.15, where a larger  $b$  forms a steeper slope towards the upper bound. The Langmuir kinetics allow that at the same concentration of injected polymer, the value of  $b$  which is equal to  $1e^{-4}$  leads to a partial saturation while a larger  $b$  enables the full saturation to come about.

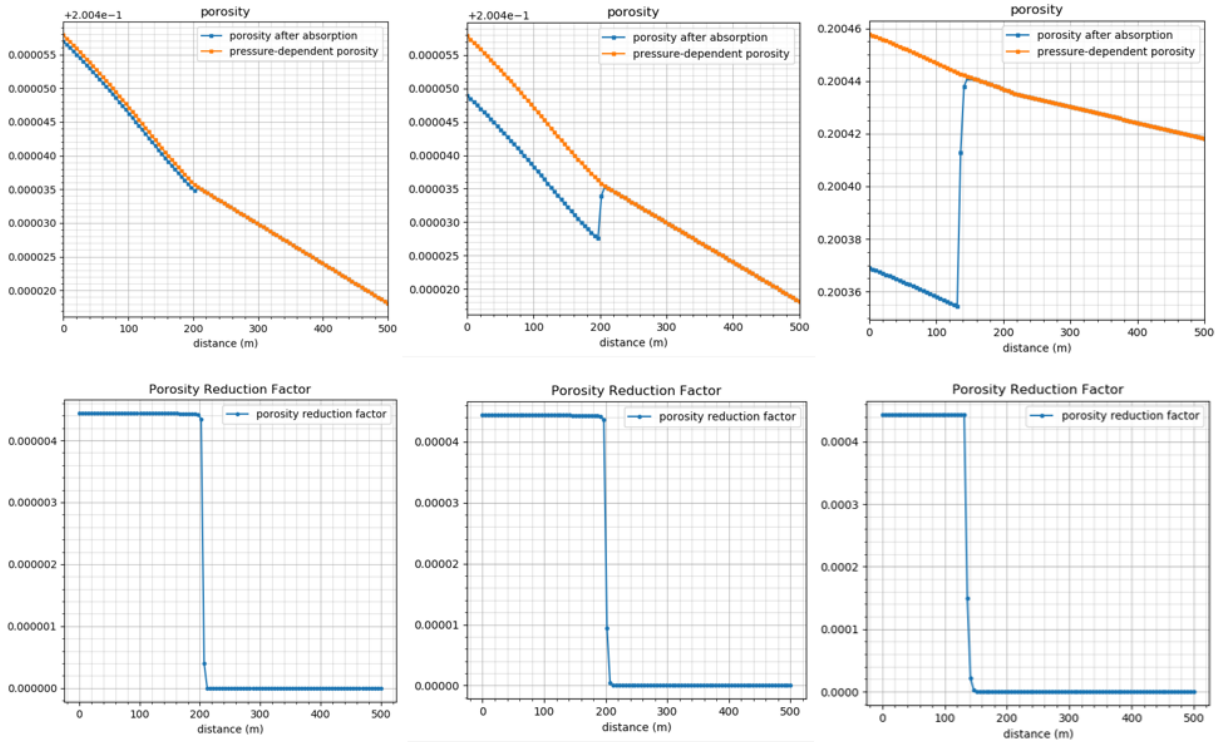


Figure 4.10: The porosity after adsorption (in blue) and original porosity (in red) in compressible porous media after 400 days is plotted in the first row. The corresponding porosity reduction factor is plotted in the second row with the polymer being injected at the injection well at a concentration of 1664ppm ( $1e^{-8}$  mol/mol). The upper bound of polymer retention is adjusted under a constant  $b$  but a varying  $a$ , achieved by three groups of parameters, which is a)  $a = 5, b = 5$ ; b)  $a = 50, b = 5$ ; c)  $a = 500, b = 5$ .

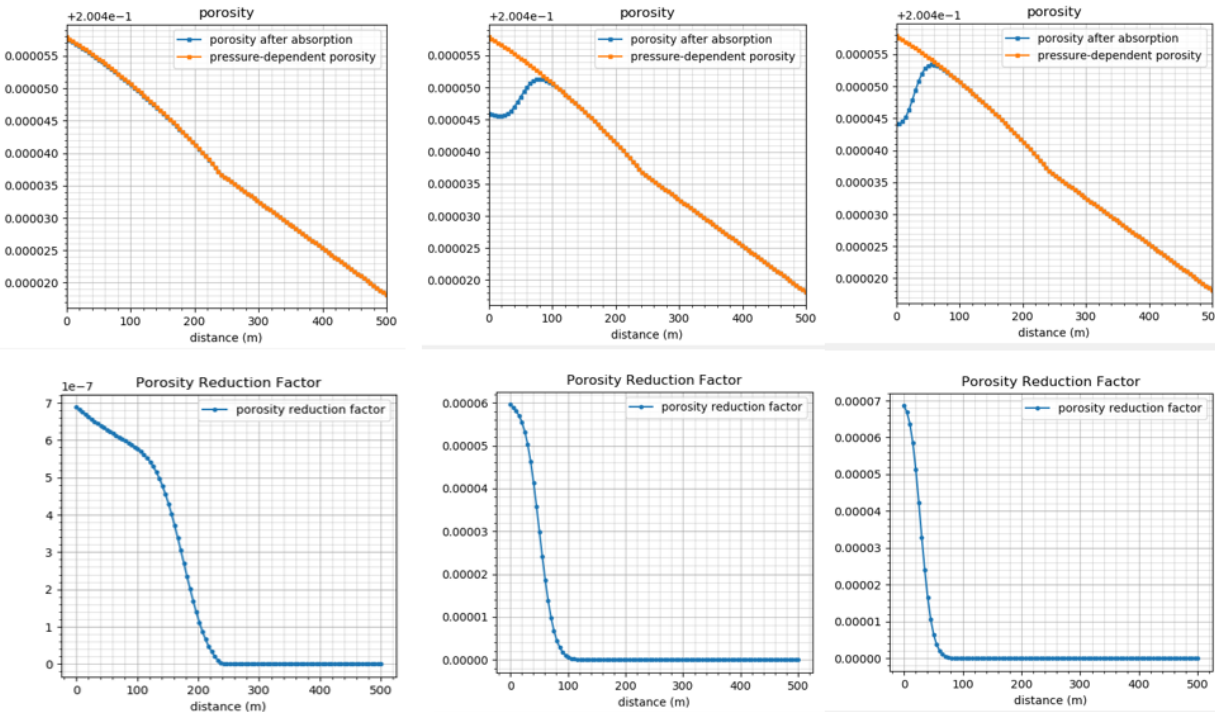


Figure 4.11: The porosity after adsorption (in blue) and original porosity (in red) in compressible porous media after 400 days is plotted in the first row. The corresponding porosity reduction factor is plotted in the second row with the polymer being injected at the injection well at a concentration of 16.6ppm  $1e^{-10}$  mol/mol). The upper bound of polymer retention remains invariable but the values of  $a$  and  $b$  change simultaneously, which can be accomplished by three sets of parameters, i.e. a)  $a = 0.01, b = 0.0001$ ; b)  $a = 1, b = 0.01$ ; c)  $a = 100, b = 1$ .

# 5

## VALIDATION

### 5.1. VALIDATION WITH UTCHEM RESULTS

The correctness of the DARTS for polymer flooding in this paper is validated by UTCHEM, a well-known chemical flooding numerical simulator in the academia [64]. UTCHEM is a chemical flooding compositional simulator developed by researchers at the University of Texas at Austin. This simulator has a comprehensive description of the chemical flooding mechanism and can simulate various chemical flooding processes such as polymer flooding, surfactant flooding, alkaline flooding and composite flooding. It is ideal for modeling of small reservoirs and core displacement experiment.

The comparison findings suggest that the numerical results of DARTS in this paper and the analytical model by UTCHEM are highly comparable, with a minor error, indicating that this model is convincing and valid. Here attached the basic setup for the validation stage in Table. 5.1.

#### 5.1.1. COMPARISON OF DARTS AND UTCHEM

UTCHEM is a three-dimensional chemical flooding simulator that is evolved from IMPES scheme. The common ground is to decouple the set of differential equations and solve the pressure equations implicitly while explicitly solving the equations for the other variable in sequence. As for UTCHEM, it's the concentration rather than saturation is then solved in a flash workflow [65].

Table 5.1: Simulation settings for HPAM rheology validation

	<b>Parameter</b>	<b>Values</b>
Reservoir Property	Depth of the top layer	1000 m
	X-direction permeability for each grid block	100 mD
	Y-direction permeability for each grid block	100 mD
	Z-direction permeability for each grid block	10 mD
	Porosity	0.2, dimensionless
	Rock compressibility	1e-5, 1/bar
Initial & Injection Condition	Initial composition for oleic phase	0.9 mol/mol
	Initial composition for aqueous phase	0.1 mol/mol
	Injected composition for polymer	1e-8 mol/mol
Well Module	Well radius	0.1524 m
	Pwf in injection well	230 bar
	Pwf in production well	210 bar
Fluid Property	Crude oil viscosity	1.8 cp
	Water viscosity	0.2 cp
	Endpoint relative permeability of oleic phase	1
	Endpoint relative permeability of aqueous phase	0.6
	Phase relative permeability exponent of oleic phase	1.8
	Phase relative permeability exponent of aqueous phase	2
	Compressibility of oleic phase	1e-3 1/bar
	Compressibility of aqueous phases	1e-11 1/bar

Contradictorily, the FIM (Fully Implicit Method) developed in DARTS is a synchronous strategy that solves pressure and saturation at the same time. Both methods are double-edged, the pros and cons of which are summarized in Table. 5.2

Table 5.2: Pros and cons of DARTS and UTCHEM algorithm.

	<b>DARTS</b>	<b>UTCHEM</b>
Pros	Of more stability and robustness; Time steps can locate in a wider range	Simplifies the complexity of non-linear equation and less computationally expensive
Cons	Higher computing cost due to FIM formulation	To stay stable, small-size time steps are necessary to be strict-controlled; Sometimes pricey and burdensome, particularly long-term integration problems and treatments with small control volumes, like the local grid refining (LGR) reservoir simulations in the wellbore-neighbouring area.

### 5.1.2. VALIDATION OF HPAM RHEOLOGY MODEL IN POROUS MEDIA

The verification logic is to gain and compare the analytical solution of UTCHEM and numerical solutions of DARTS of the rheological relationship (viscosity and shear rate) for different injected polymer concentrations rooted on the unified model in Eq. 3.22. The analytical solution is adapted to both simulators at the same time since DARTS and UTCHEM share the same unified model.

The analytical solution possesses the upper hand that its  $x$  variable can be shear rate in a all-inclusive range, allowing the rheological behaviour to be captured continuously and comprehensively. Viewing Fig. 5.1 from left to right, the viscosity grows smaller due to shear thinning and then grows up owing to shear thickening for all three curves under varied injected polymer. However, the numerical solution obtained with a limited number of grids and degree of interpolation accuracy will be relatively narrowed down. For example, it is incredibly hard to obtain a shear rate of 0.0001 and 10,000 at the same time in a Cartesian grid reservoir.

Therefore, three different pressures in the injection well are implemented to collect three different shear rate intervals (Table. 5.3), as shown in the blue and red coloured blocks in the Fig. 5.1. In this way, the pseudoplasticity of the polymer (the viscosity decreases as the shear rate increases) and the viscoelasticity (the viscosity rebounds as the shear rate increases within the relaxation time) are captured. Through comparison, it is found that the numerical solution and the analytical solution maintain a high degree of agreement, which is in line with expectations.

Zooming into the shear thinning stage of the first stage, which is shown in the Fig. 5.1, we can

Table 5.3: Simulation settings for HPAM rheology validation.

Parameter	Values
Injected polymer concentration	$2e^{-8}, 1e^{-8}, 1e^{-9}$ mol/mol (3330 ppm, 1667 ppm, 167 ppm) (set for triple)
Bottomhole Pressure at injection well	500 bar, 300 bar and 230 bar (set for triple)
Zero-shear viscosity parameters $Ap1, Ap2, Ap3$	40, 0, 0
The parameters considering the effect of salinity $C_{SEP}, S_p$	1, 0
Shear thinning model parameters $\beta_1, \beta_2, n_1$	0.25, 0.5, 0.9
Shear thickening model parameters $AP_{11}, AP_{22}, \tau_0, \tau_1, n_2,$ and $\lambda_2$	0.1, 0.01, 3000, 1500, 2, $1e^{-7}$

see the effect of the injected polymer concentration and salinity on the apparent polymer viscosity

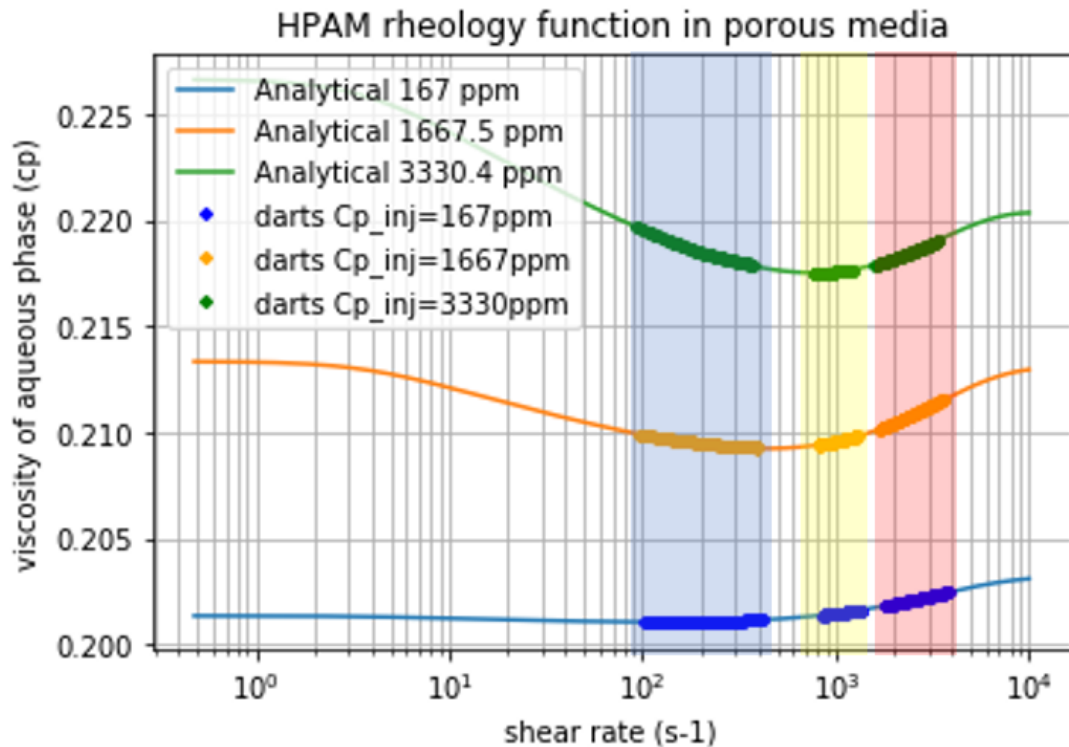


Figure 5.1: Analytical solution and numerical solution of HPAM rheology in porous media at different concentrations of 167ppm, 1667ppm and 3330ppm. The continuous curves present the unified analytical model while the discretised points present the numerical results implemented by DARTS. The two blocks in light blue, yellow and red mark the three intervals of shear rates when the pressure at injection well is 230bar, 300bar and 500bar respectively.

more distinctly. In correspondingly, small range of bottomhole pressure has been adjusted to reach a low level of shear rate.

In Fig. 5.2, the lower the mass concentration of polymer molecules, the fewer molecules in the aqueous solution, the lower the likelihood of molecular chains or coils intertwining and permeating each other, and thus there is no perceived increase in the viscosity of the polymer at a lower injection concentration. When the salinity degree is rising, and intramolecular and intermolecular hydrogen bonds are forming between positive and negative ion groups (resulting in the decrease of the solubility of the polymer in water). At the same time, the additional ion from salt shields the positive and negative charges, allowing them to scatter. The formation of salt bonds is destroyed when negative ions come together (resulting in an increase in the solubility of the polymer in water). These two actions cancel each other out, hence the polymer's viscosity-increasing impact at higher salt concentrations is zero as observed in Fig. 5.3. That is, the apparent viscosity of the polymer solution flattens out and is infinitely close to the solvent viscosity.

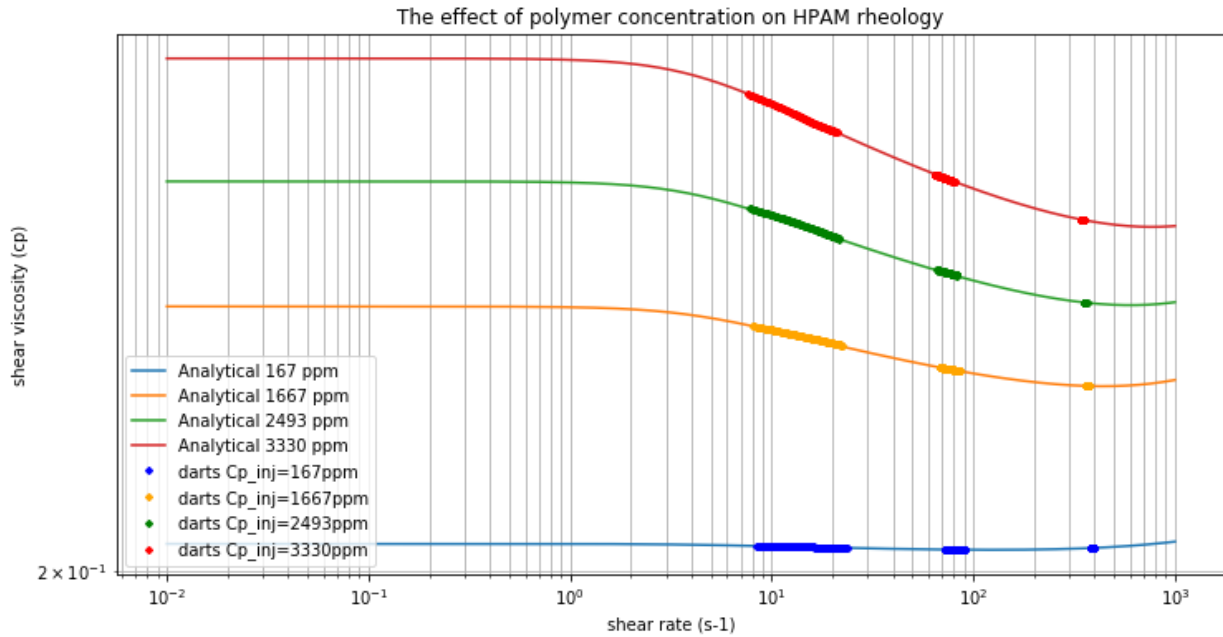


Figure 5.2: Analytical solution and numerical solution of HPAM rheology in porous media affected by different concentrations of 167ppm, 1667ppm and 3330ppm. The continuous curves present the unified analytical model while the discretised points present the numerical results implemented by DARTS. The three intervals of shear rates when the pressure at injection well is 215bar, 230bar and 300bar respectively.

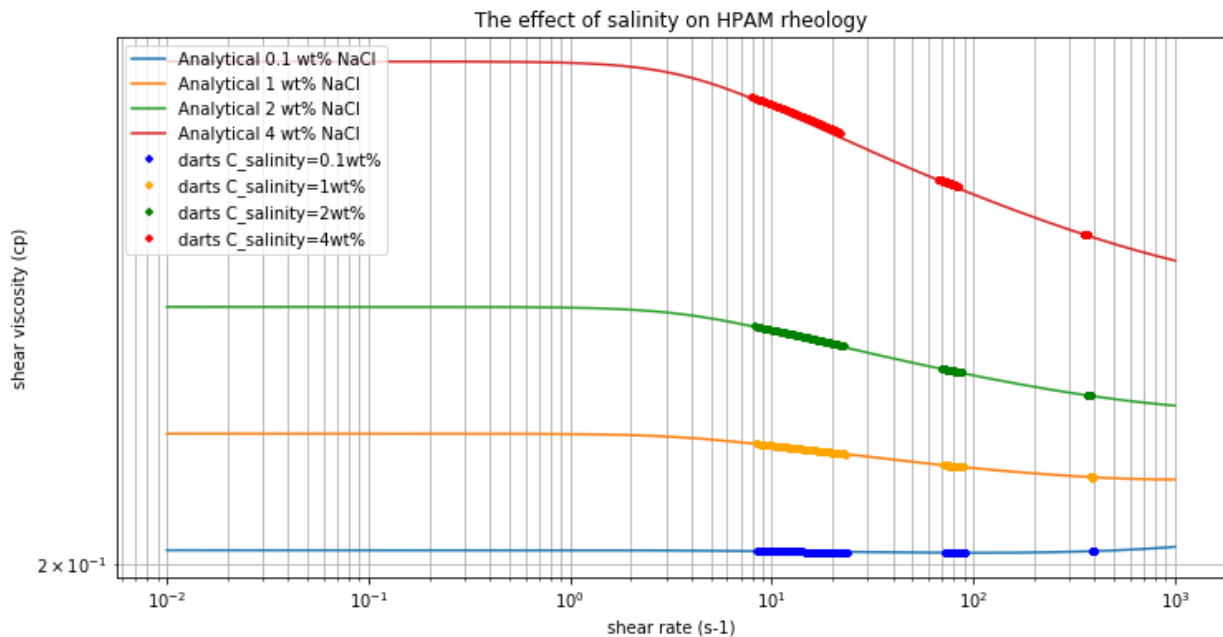


Figure 5.3: Analytical solution and numerical solution of HPAM rheology in porous media affected by different salinity of 0.1wt%, 1wt%, 2wt% and 4wt%. The continuous curves present the unified analytical model while the discretised points present the numerical results implemented by DARTS. The three intervals of shear rates when the pressure at injection well is 215bar, 230bar and 300bar respectively.

## 5.2. VALIDATION WITH BUCKLEY-LEVERETT SOLUTION

Fig. 5.4 illustrates the fractional flow curve for water flooding and polymer flooding. All the parameters remained as in Table. 5.4, and the aqueous viscosity with the polymer is 0.4 cP. The

initial condition is  $S_{w,iw}=0.1$ , and the boundary condition is continuous polymer injection,  $f_w=1$  and  $\mu_p=0.4$  cP.

Table 5.4: Corey model parameters for water–oil two-phase relative permeability in the presence and absence of polymer.

Water-Oil Two-Phase Relative Permeability in the Absence of Polymer							
$k_{rw}^0$	$k_{ro}^0$	$S_{w,iw}$	$S_{oi}$	$n_w$	$n_o$	$\mu_w$	$\mu_o$
0.6	1.0	0.1	0.05	2.0	1.8	0.2	0.4
Water-Oil Two-Phase Relative Permeability in the Presence of Polymer							
$k_{rw}^0$	$k_{ro}^0$	$S_{w,iw}$	$S_{oi}$	$n_w$	$n_o$	$\mu_p$	$\mu_o$
0.6	1.0	0.1	0.05	2.0	1.8	0.4	0.4

The construction of the shock front and saturation profile at 0.33 PV are exhibited in Fig. 5.4 (a) and (b). Two shocks form are developed, which is the oil bank front behind which the initial water in the system displaces oil and the chemical front behind which the injected chemical pushes the oil toward the outlet. Behind the polymer shock, it is a region of spreading waves with constant polymer concentration. A clear oil bank still can be formed due to the increase of the aqueous phase viscosity during continuous polymer injection.

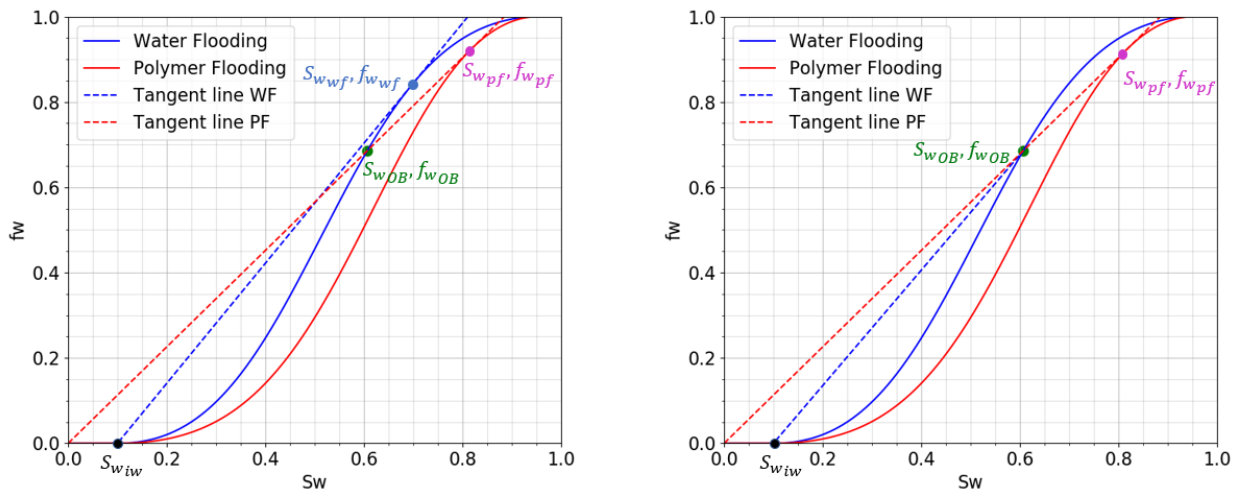


Figure 5.4: (a) Comparison of water front by water flooding and polymer flooding. (b) Construction of water front during polymer flooding. Hereby  $S_{w_{wf}}$  and  $f_{w_{wf}}$  are the water saturation and fractional flow at the shock of water flooding,  $S_{w_{pf}}$  and  $f_{w_{pf}}$  are the water saturation and fractional flow at the shock of polymer flooding and  $S_{w_{OB}}$  and  $f_{w_{OB}}$  are the water saturation and fractional flow in the oil bank.

As Fig. 5.5 is shown, the difference between the secondary recovery and tertiary recovery is that the water saturation jumps from water saturation in the oil bank ( $S_{w_{OB}} = 0.49$ ) to connate water saturation ( $S_{w_{iw}} = 0.1$ ) in the secondary case and from  $S_{w_{pf}}$  to  $S_{w_{OB}}$  in the tertiary case. It should be noted that for the example case,  $S_{w_{OB}}$  is smaller than  $S_{w_{wf}}$ , as shown in Fig. 5.4 (b). If it is not the case, there will be a spreading wave between ( $S_{w_{OB}}$ ) and ( $S_{w_{wf}}$ ).

The oil saturation ( $1-S_{wOB}$ ) and oil fractional flow ( $1-f_{wOB}$ ) in the oil bank are 0.61 and 0.68, respectively. Moreover, we can see that the time required to reach residual oil saturation is significantly shortened at augmented aqueous viscosity with the help of the polymer.

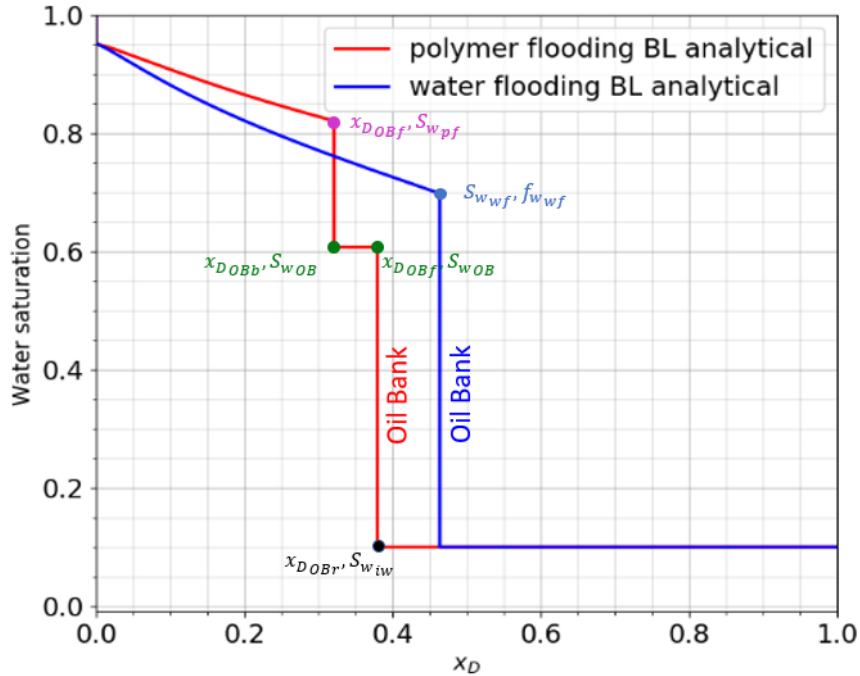


Figure 5.5: Analytical water saturation profile at  $t_d = 0.33PV$  during polymer flooding (in red) and water flooding (in blue). Where,  $x_{DOBb}$  and  $x_{DOBf}$  are named to differentiate the transporting distance at the back and front of the oil bank.

Next step is to validate the numerical results obtained by DARTS with the above stated Buckley-Leverett solution. As the harmonic mean is the key factor causing the smoothness in inflection point. In contrast, there will be a sudden variance instead of a median between two different fluid properties (i.e. mobility and transmissibility) in realistic condition. In response, the corresponding segment on curve for transition area shortened on account of diminished  $dx$ . Thereby, with more and more grids introducing, the curve in red combined with numerous points will be much smoother and close to the analytical result marked by solid line step by step. The second segment started from the shock location will jump to zero perpendicularly.

In order to get as close as possible to the analytical solution, two kinds of high-resolution settings with respect to the space (Fig. 5.6) and the time (Fig. 5.7) have been plotted. For both Fig. 5.6 (a) and (b) and Fig. 5.7 (a) and (b), the numerical slope of the shock rises to a much sharper angle and gets more proximity to analytical level.

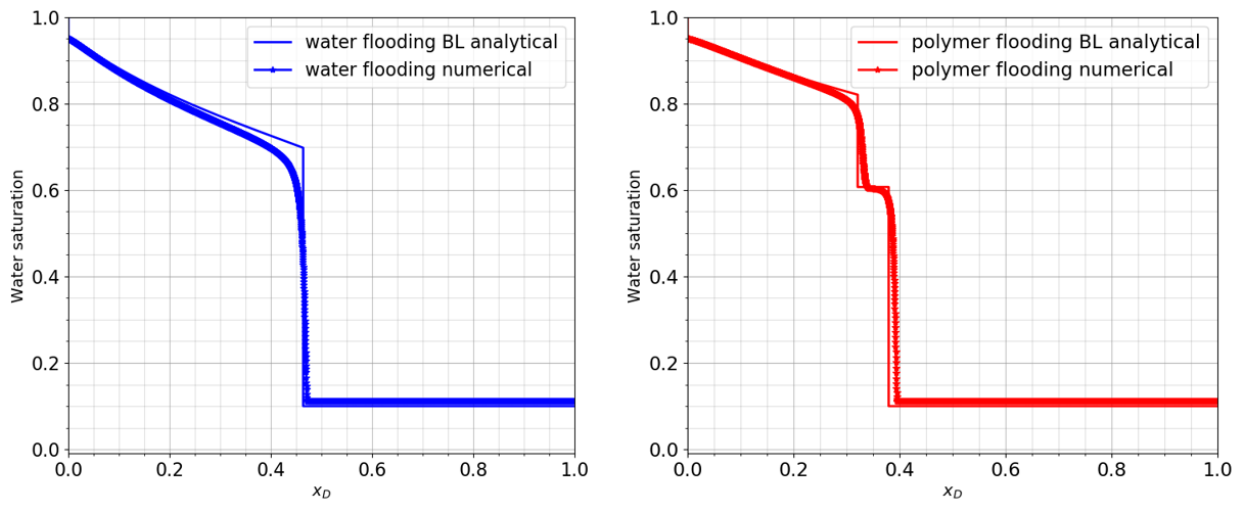


Figure 5.6: Comparison of (a) analytical water saturation profile and (b) numerical water saturation profile by DARTS at  $td = 0.33PV$  and the numerical solution is obtained at 400 days in a 500m-length 1D reservoir ( $dt=5$ days,  $dx=0.1$ ) during water flooding (in blue) and polymer flooding (in red).

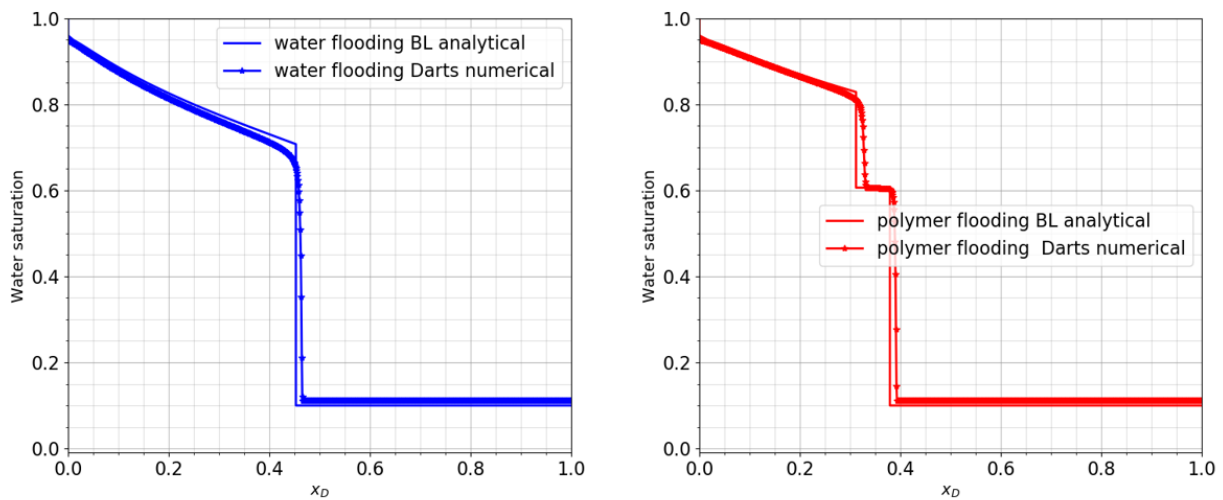


Figure 5.7: Comparison of (a) analytical water saturation profile and (b) numerical water saturation profile by DARTS. The analytical solution is obtained at  $td = 0.33pv$  and the numerical solution is obtained at 400 days in a 500m-length 1D reservoir ( $dt=1$ days,  $dx=1$ ) during water flooding (in blue) and polymer flooding (in red).

# 6

## COREFLOOD SIMULATION

In this work, the purpose was to test if the OBL approach can effectively capture the physical mechanism of polymer flooding by a more tangible coreflood, which is unable to be predicted precisely by the homogeneous model under steady state. We employ the CT coreflood model used in [66, 67] for foam displacement, and the general properties of the core are listed in Table. 6.1.

Table 6.1: Core and experimental fluid properties for experiment

<b>Rock Type</b>	Bentheimer Sandstone
<b>Absolute Permeability (<math>mD</math>)</b>	2820
<b>Porosity (%)</b>	0.22
<b>Diameter (<math>cm</math>)</b>	4
<b>Length (<math>cm</math>)</b>	40
<b>Area (<math>cm^2</math>)</b>	12.57
<b>Bulk Volume (<math>cm^3</math>)</b>	502.65
<b>Pore Volume (<math>cm^3</math>)</b>	110.58

### 6.1. 3D CT COREFLOOD AND RESERVOIR CONSTRUCTION

A 3D heterogeneous simulation grid is established based on the CT images, as is presented in Fig. 6.1(b). The porosity of each pixel and each CT slice has been corrected by use of the following

formula [68].

$$\phi = \frac{CT_{water} - CT_{air}}{CT_w - CT_a} \quad (6.1)$$

where  $CT_{water}$  and  $CT_{air}$  are the CT values of a core completely soaked with water and a unsaturated core filled with air respectively;  $CT_w$  and  $CT_a$  are CT values of water and air, respectively.

In this way porosity of each triangular grid block can be obtained. As the slice shown in Fig. 6.1 (a), the porosity is distributed in an unstructured network composed of 1,080 grids with an average area of  $1.16 \text{ mm}^2$ . Correspondingly, the permeability can be computed using the Kozeny-Carman equation (Eq. 6.2)

$$k = \alpha \frac{\phi^3 D_p^2}{(1 - \phi)^2}, \quad (6.2)$$

where  $k$  refers to the absolute permeability in  $md$ ;  $D_p$  denotes the average diameter of sand grains in  $mm$ ;  $\phi$  symbolizes the porosity of the core, with the unit in fraction and  $\alpha$  stands for the combined proportionality and unity factor in unit of  $md/mm^2$ .

The permeability is assumed to share the same distribution pattern and frequency with the porosity. This assumption allows the overall permeability and porosity distribution to be solved applying the group of  $\alpha$  and  $D_p^2$  extracted from the relationship between the known average porosity and average permeability.

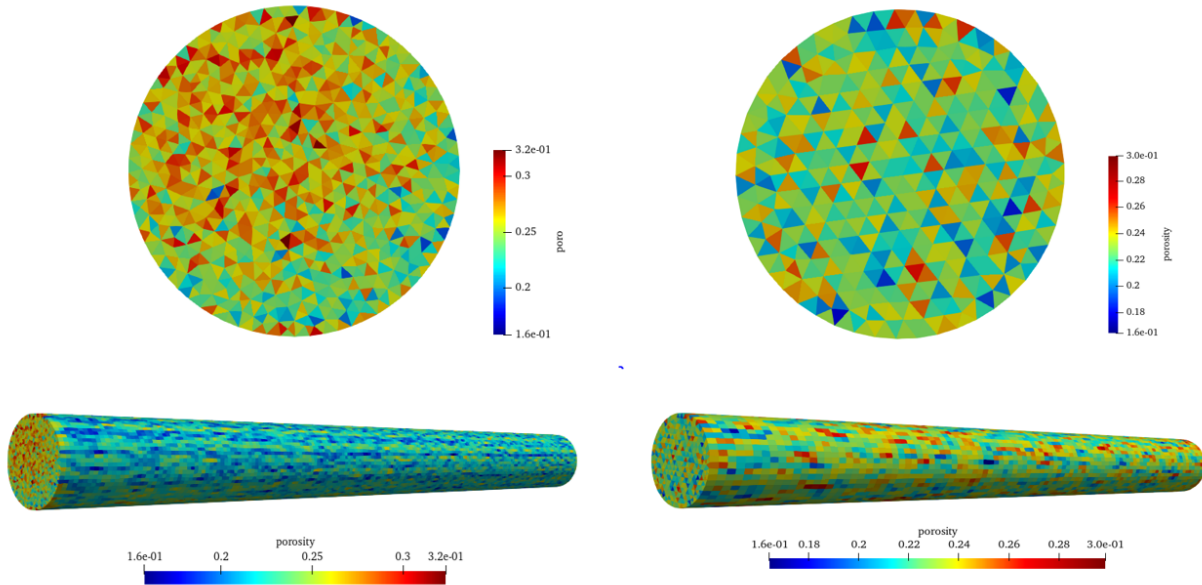


Figure 6.1: Porosity profile of Bentheimer sandstone at a slice and along the core a) before coarsening and b) after coarsening.

Because of the expensive computation cost while solving a global mass conservation equation, the original models ( $1080 \times 198$ ) are then coarsened in the following dynamic flow simulation as

shown in Fig. 6.1 (b).

## 6.2. MODELLING OF TWO-PHASE FLOW IN TERTIARY SYSTEM

As the core length is only 40 cm, only 0.82 PV of injection is simulated (equivalent to  $3 \times 10^{-5}$  days). The injection inlet and the production outlet locate at the far left and right ends respectively of the core and all unstructured grids at the two ends of the slice are connected with them. The Fig. 6.3 show that the water molar fraction when the polymer is injected is far smaller than when polymer is not injected. This displays that the polymer flood slows down the propagation of the water in the core due to the increased water viscosity. Likewise, in Fig. 6.4 the oil molar fraction at the production well with polymer is higher than the oil molar fraction of the case without injection of polymer, confirming once again the physical properties of polymer injections which aims to increase swept surfaces and reduce the displacement rate.

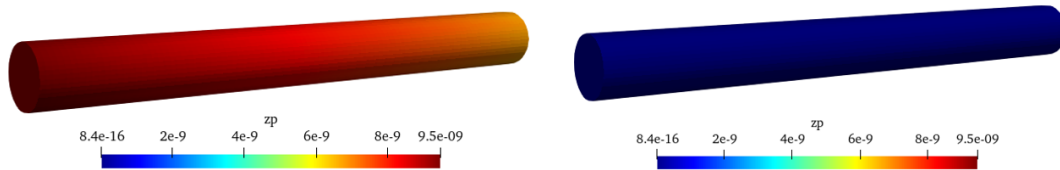


Figure 6.2: The molar fraction of polymer when injecting a)  $1 \times 10^{-8}$  mol/mol (1667ppm) and b) no polymer at  $3 \times 10^{-5}$  days.

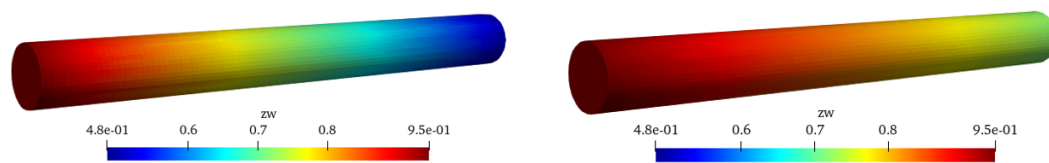


Figure 6.3: The molar fraction of water when injecting a)  $1 \times 10^{-8}$  mol/mol (1667ppm) and b) no polymer at  $3 \times 10^{-5}$  days.

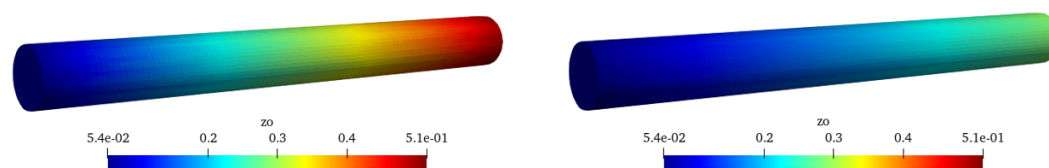


Figure 6.4: The molar fraction of oil when injecting a)  $1 \times 10^{-8}$  mol/mol (1667ppm) and b) no polymer at  $3 \times 10^{-5}$  days.

### 6.3. THE EFFECT OF INJECTED POLYMER CONCENTRATION ON POROSITY

Except for the obvious effect of the concentration of injected polymer as the flowing retardation of water stated in Section. 6.2, the injected polymer concentration also exerts a non-ignorable effect on polymer adsorption and porosity reduction.

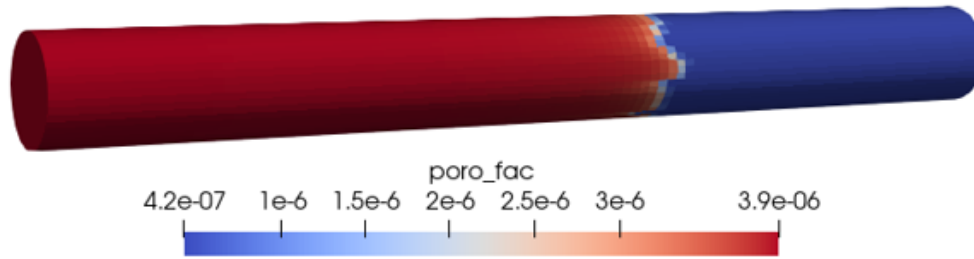


Figure 6.5: The porosity reduction factor distribution at injected polymer concentration of 1664 ppm ( $1 \times 10^{-8}$  mol/mol) serves as the only variable. Hereby the upper bound of polymer retention is set to be 1, with a and b both set to be 5.

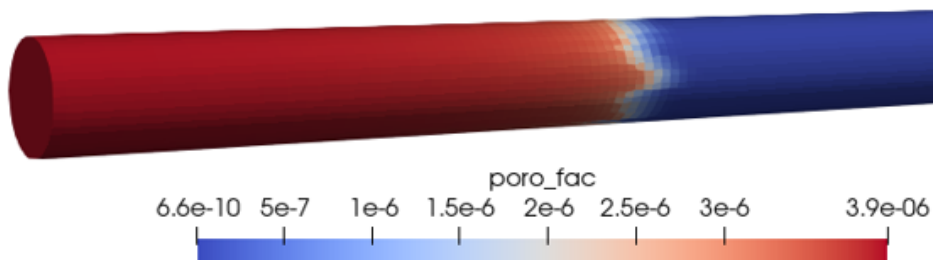


Figure 6.6: The porosity reduction factor distribution at injected polymer concentration of 16.6 ppm ( $1 \times 10^{-10}$  mol/mol) serves as the only variable. Hereby the upper bound of polymer retention is set to be 1, with a and b both set to be 5.

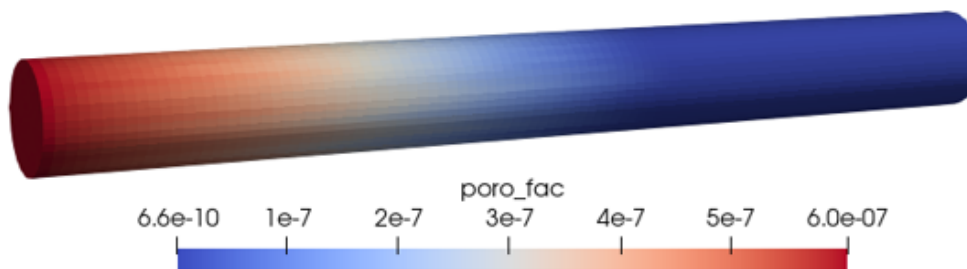


Figure 6.7: The porosity reduction factor distribution at injected polymer concentration of 1.66 ppm ( $1 \times 10^{-12}$  mol/mol) serves as the only variable. Hereby the upper bound of polymer retention is set to be 1, with a and b both set to be 5.

Observing the Fig. 6.5, Fig. 6.6 and Fig. 6.7, it can be seen that as the injected polymer concentration decreases, the constant part with larger porosity, where polymer solution sweeps (i.e., inlet side), gradually becomes shorter, while the transition zone and the another constant part with relatively smaller porosity become longer. This 3D result is exactly identical with the previous 1D result in subsection. 4.3.1. It can be regarded as three stages: the first stage occurs when the polymer concentration is injected at its maximum, resulting in over-saturated state and a maximum porosity reduction factor, and the second stage occurs when the polymer shock appears, causing the increasing percentage of retained polymer to all of the injected polymer which lasts until the third stage where polymer is undersaturated.

As the polymer concentration drops, it is no longer possible for the polymer to maintain the upper bound of adsorption, resulting in a gradual increase in the transition period between oversaturation (first stage) and undersaturation (third stage). Simultaneously, the critical point (between the second and the third stage) will be achieved earlier, leading to a longer third stage of undersaturation.

# 7

## CONCLUSION AND RECOMMENDATIONS

In this chapter we present and discuss our results and recommend how to keep improving these results.

### 7.1. CONCLUSION

In this work, we first extend the simple two-phase two components model to two-phase three components model for the EOR-based polymer flooding simulation. Whereby, the conservation equation is solved by Fully Implicit Method using the Operator-Based Linearization framework, a more stable and less costly approach to deal with the associated physics of polymer.

The obtained model achieves to present the phenomenon of rheological behaviour and retention of polymer. To better present the nature of shear-viscosity and elongational viscosity, a unified viscosity model for field-scale polymer flooding projects involving a full spectrum of Newtonian, shear-thinning, and shear-thickening flowing behaviour of polymer solutions has been successfully implemented in the DARTS polymer module. For polymer retention, the influence of retained polymer macromolecules on porosity reduction besides permeability reduction has been investigated and has a perfect response with the principle of Langmuir isotherm adsorption.

Referring to complex variables during the flooding process, an exhaustive sensitivity study has been conducted to analyse the displacement mechanism of polymer with respect to a comprehen-

sive consideration of fluid properties and subsurface structure. Each variable is adjusted for both polymer rheology and retention, and the impact caused by different variables is evaluated.

To test the robustness of the proposed DARTS model, the analytical model from UTCHEM is selected as the first benchmark with our numerical results. According to these comparisons, we demonstrate the full physics can be accurately predicted with invisible error. In addition, the shear-viscosity relationship gained numerically nicely match the experimental data shown in the Fig. 2.9 in Chapter. 2. Next, a Buckley-Leverett solution is applied to verify the reliability of our model. The analytical and numerical saturation profiles perfectly coincide with each other with only a tiny discrepancy caused by discretization.

Through the 3D CT core flood modelling, the polymer flooding simulation has been put into practice under a heterogeneous scenario. In this way, a more close-to-reality scenario has been constructed which ultimately demonstrates the correctness and feasibility of our polymer flood simulator in the field application.

## 7.2. RECOMMENDATION

In the future, numerous work can be done to extend the polymer flooding capabilities in DARTS.

- Integrate more physics for field scale polymer flood including all kinds of degradation, chemical reaction, diffusion, etc.;
- Model temperature and pH effect on polymer viscosity and polymer/oil/brine phase behavior;
- Simulate composite ASP (alkaline/surfactant/polymer) flooding;
- The undermining polymer injectivity near the wellbore and the effect of induced hydraulic fractures on injectivity.

# BIBLIOGRAPHY

- [1] Abass A Olajire. Review of asp eor (alkaline surfactant polymer enhanced oil recovery) technology in the petroleum industry: Prospects and challenges. *Energy*, 77:963–982, 2014.
- [2] Ali Goudarzi, Mojdeh Delshad, and Kamy Sepehrnoori. A critical assessment of several reservoir simulators for modeling chemical enhanced oil recovery processes. In *SPE Reservoir Simulation Symposium*. OnePetro, 2013.
- [3] Guy Chauveteau et al. Molecular interpretation of several different properties of flow of coiled polymer solutions through porous media in oil recovery conditions. In *SPE Annual Technical Conference and Exhibition*. Society of Petroleum Engineers, 1981.
- [4] Seungjun Lee, Do Hoon Kim, Chun Huh, Gary Arnold Pope, et al. Development of a comprehensive rheological property database for eor polymers. In *SPE Annual Technical Conference and Exhibition*. Society of Petroleum Engineers, 2009.
- [5] James J Rogalski, Lorenzo Botto, Cees WM Bastiaansen, and Ton Peijs. A study of rheological limitations in rotary jet spinning of polymer nanofibers through modeling and experimentation. *Journal of Applied Polymer Science*, 137(33):48963, 2020.
- [6] Basics of rheology. <https://wiki.anton-paar.com/nl-en/basics-of-rheology/>, 2020.
- [7] Ali Mohsenatabar Firozjahi and Hamid Reza Saghafi. Review on chemical enhanced oil recovery using polymer flooding: Fundamentals, experimental and numerical simulation. *Petroleum*, 6(2):115–122, 2020.
- [8] Larry W Lake. *Enhanced oil recovery*. Old Tappan, NJ; Prentice Hall Inc., 1989.
- [9] Guangzhi Liao, Qiang Wang, Hongzhuang Wang, Weidong Liu, and Zhengmao Wang. Chemical flooding development status and prospect. *Acta Petrolei Sinica*, 38(02):196–207, 2017.

- [10] Vladimir Vishnyakov, Baghir Suleimanov, Ahmad Salmanov, and Eldar Zeynalov. *Primer on Enhanced Oil Recovery*. Gulf Professional Publishing, 2019.
- [11] Demin Wang, Lanshui Zhao, Jiecheng Cheng, Junzheng Wu, et al. Actual field data show that production costs of polymer flooding can be lower than water flooding. *Society of Petroleum Engineers*, 2003.
- [12] FC CRAIG. The reservoir engineering aspects of waterflooding. *Monograph Series, Society of Petroleum Engineers of AIME*, 1971.
- [13] Laila Dao Saleh, Mingzhen Wei, Baojun Bai, et al. Data analysis and updated screening criteria for polymer flooding based on oilfield data. *SPE Reservoir Evaluation & Engineering*, 17(01):15–25, 2014.
- [14] Alain Hill, Françoise Candau, and Joseph Selb. Properties of hydrophobically associating polyacrylamides: influence of the method of synthesis. *Macromolecules*, 26(17):4521–4532, 1993.
- [15] Behruz Shaker Shiran and Arne Skauge. Similarities and differences of low salinity polymer and low salinity lps (linked polymer solutions) for enhanced oil recovery. *Journal of dispersion science and technology*, 35(12):1656–1664, 2014.
- [16] Shiyi Yuan, Puhua Yang, Zhongqiu Dai, Kuiyou Shen, et al. Numerical simulation of alkali/surfactant/polymer flooding. In *International Meeting on Petroleum Engineering*. Society of Petroleum Engineers, 1995.
- [17] Wan-lu Liu, De-sheng MA, Qiang WANG, and Zhao-xia Liu. Numerical simulation for chemical flooding [j]. *Journal of Daqing Petroleum Institute*, 3, 2012.
- [18] Kevin C Taylor and Hisham A Nasr-El-Din. Water-soluble hydrophobically associating polymers for improved oil recovery: A literature review. *Journal of Petroleum Science and Engineering*, 19(3-4):265–280, 1998.
- [19] J.E Peterson. Coalinga polymer demonstration project, final report. *No.DOE/SAN/1556-5, US DOE, Washington DC*, 1981.

- [20] Randall S Seright et al. The effects of mechanical degradation and viscoelastic behavior on injectivity of polyacrylamide solutions. *Society of Petroleum Engineers Journal*, 23(03):475–485, 1983.
- [21] Alireza Rostami, Mahdi Kalantari-Meybodi, Masoud Karimi, Afshin Tatar, and Amir H Mohammadi. Efficient estimation of hydrolyzed polyacrylamide (hpam) solution viscosity for enhanced oil recovery process by polymer flooding. *Oil & Gas Sciences and Technology–Revue d’IFP Energies nouvelles*, 73:22, 2018.
- [22] Sandeep Rellegadla, Ganshyam Prajapat, and Akhil Agrawal. Polymers for enhanced oil recovery: fundamentals and selection criteria. *Applied microbiology and biotechnology*, 101(11):4387–4402, 2017.
- [23] Dag Chun Standnes and Ingun Skjevrak. Literature review of implemented polymer field projects. *Journal of Petroleum Science and Engineering*, 122:761–775, 2014.
- [24] A. H. P. Skelland. *Non-Newtonian Flow and Heat Transfer*. John Wiley Sons, Inc. New York, London, and Sydney, 1967.
- [25] Yu-Shu Wu. Theoretical studies of non-newtonian and newtonian fluid flow through porous media. Technical report, Lawrence Berkeley Lab., CA (USA), 1990.
- [26] GJ Hirasaki and GA Pope. Analysis of factors influencing mobility and adsorption in the flow of polymer solution through porous media. *Society of Petroleum Engineers Journal*, 14(04):337–346, 1974.
- [27] J Heemskerk, R Rosmalen, R Janssen-Van, RJ Holtslag, D Teeuw, et al. Quantification of viscoelastic effects of polyacrylamide solutions. In *SPE Enhanced Oil Recovery Symposium*. Society of Petroleum Engineers, 1984.
- [28] Yoshihiro Masuda, Ke-Chin Tang, Masashi Miyazawa, Shoichi Tanaka, et al. 1d simulation of polymer flooding including the viscoelastic effect of polymer solution. *SPE reservoir engineering*, 7(02):247–252, 1992.
- [29] Jirui Hou Yongqiang Tang, Chengyuan Lyu. Shear rate algorithm of power-law fluid based on pore distribution. *Science Technology and Engineering*, 16(02):43–46+68, 2016.

- [30] Yongpeng Sun, Laila Saleh, and Baojun Bai. Measurement and impact factors of polymer rheology in porous media. *Rheology, InTech*, pages 187–202, 2012.
- [31] Josef Kozeny. Uber kapillare leitung der wasser in boden. *Royal Academy of Science, Vienna, Proc. Class I*, 136:271–306, 1927.
- [32] Phillip C Carman. Fluid flow through granular beds. *Chemical Engineering Research and Design*, 75:S32–S48, 1997.
- [33] WJ Cannella, C Huh, RS Seright, et al. Prediction of xanthan rheology in porous media. In *SPE annual technical conference and exhibition*. Society of Petroleum Engineers, 1988.
- [34] Dwight L Dauben, DE Menzie, et al. Flow of polymer solutions through porous media. *Journal of Petroleum Technology*, 19(08):1–065, 1967.
- [35] P Zitha, G Chauveteau, A Zaitoun, et al. Permeability~ dependent propagation of polyacrylamides under near-wellbore flow conditions. In *SPE International Symposium on Oilfield Chemistry*. Society of Petroleum Engineers, 1995.
- [36] Masayoshi Yamaguchi, Michio Wakutsu, Yoshiaki Takahashi, and Ichiro Noda. Viscoelastic properties of polyelectrolyte solutions. 1. zero-shear viscosity. *Macromolecules*, 25(1):470–474, 1992.
- [37] Bo Nystroem. Zero-shear viscosity properties of solutions of flexible polymers in light of renormalization group theories. *Macromolecules*, 26(15):3784–3790, 1993.
- [38] Paul J Flory. *Principles of polymer chemistry*. Cornell University Press, 1953.
- [39] Kenneth S Sorbie. *Polymer-improved oil recovery*. Springer Science & Business Media, 2013.
- [40] Zhao Xiutai, Wang Zengbao, Qiu Guangmin, et al. Study on influence factors of the initial viscosity of hpam solution. *Chemical engineering of oil & gas*, 3, 2009.
- [41] Changli Yuan. *Commercial scale simulations of surfactant/polymer flooding*. PhD thesis, 2012.
- [42] D.C.R.De Kee P.J.Carreau and R.P.Chhabra. *Rheology of Polymeric Systems. Principles and Applications*. Hanser/Gardner Publications, 1997.

- [43] Abdulwahab Saeed Alqahtani. *New polymer rheology models based on machine learning*. PhD thesis, 2019.
- [44] PP Shah and PH Parsania. Zero-shear viscosity of dilute to moderately concentrated solutions of poly [2-methoxy-4, 6-di-(p, p-isopropylidene diphenyloxy)-s-triazine]. *Journal of Macromolecular Science, Part B*, 23(4-6):363–372, 1984.
- [45] Robert Byron Bird, Edwin N Lightfoot, and Warren E Stewart. *Notes on Transport Phenomena. Transport Phenomena. By RB Bird, Warren E. Stewart, Edwin N. Lightfoot. A Rewritten and Enlarged Edition of "Notes on Transport Phenomena"*. John Wiley & Sons, 1960.
- [46] Pierre J Carreau. Rheological equations from molecular network theories. *Transactions of the Society of Rheology*, 16(1):99–127, 1972.
- [47] Yiwei Ma et al. *Diagnosis of induced hydraulic fractures during polymer injection*. PhD thesis, 2015.
- [48] Nematollah Zamani, Igor Bondino, Roland Kaufmann, and Arne Skauge. Effect of porous media properties on the onset of polymer extensional viscosity. *Journal of Petroleum Science and Engineering*, 133:483–495, 2015.
- [49] Mojdeh Delshad, Do Hoon Kim, Oluwaseun Adedeji Magbagbeola, Chun Huh, Gary Arnold Pope, Farhad Tarahhom, et al. Mechanistic interpretation and utilization of viscoelastic behavior of polymer solutions for improved polymer-flood efficiency. In *SPE Symposium on Improved Oil Recovery*. Society of Petroleum Engineers, 2008.
- [50] Robert Byron Bird, Robert Calvin Armstrong, and Ole Hassager. Dynamics of polymeric liquids. vol. 1: Fluid mechanics. 1987.
- [51] Necmettin Mungan et al. Rheology and adsorption of aqueous polymer solutions. *Journal of Canadian Petroleum Technology*, 8(02):45–50, 1969.
- [52] FW Smith. Behavior of partially hydrolyzed polyacrylamide solutions in porous media. Technical report, Sinclair Oil Corp, 1969.
- [53] N Schamp and J Huylebroeck. Adsorption of polymers on clays. In *Journal of Polymer Science: Polymer Symposia*, volume 42, pages 553–562. Wiley Online Library, 1973.

- [54] Herbert kindly. *Capillary chemistry: a presentation of the chemistry of colloids and related fields*. academic publishing company, 1922.
- [55] Zhao G. Zhu, B. *Fundamentals of Interface Chemistry*. Chemical Industry Press, 1996.
- [56] Stephen Brunauer, Paul Hugh Emmett, and Edward Teller. Adsorption of gases in multi-molecular layers. *Journal of the American chemical society*, 60(2):309–319, 1938.
- [57] Charles H Giles, David Smith, and Alan Huitson. A general treatment and classification of the solute adsorption isotherm. i. theoretical. *Journal of colloid and interface science*, 47(3):755–765, 1974.
- [58] Guoyin Zhang and RS Seright. Effect of concentration on hpam retention in porous media. *SPE Journal*, 19(03):373–380, 2014.
- [59] ByungIn Choi, Jinsuk Choi, and Kun Sang Lee. Integrated analysis of permeability reduction caused by polymer retention for better understanding polymer transport. *Journal of Chemistry*, 2015, 2015.
- [60] Rapier Dawson, Ronald B Lantz, et al. Inaccessible pore volume in polymer flooding. *Society of Petroleum Engineers Journal*, 12(05):448–452, 1972.
- [61] Monrawee Pancharoen, Marco Roberto Thiele, Anthony Robert Kavscek, et al. Inaccessible pore volume of associative polymer floods. In *SPE Improved Oil Recovery Symposium*. Society of Petroleum Engineers, 2010.
- [62] Denis V Voskov. Operator-based linearization approach for modeling of multiphase multi-component flow in porous media. *Journal of Computational Physics*, 337:275–288, 2017.
- [63] Mark Khait. *Delft Advanced Research Terra Simulator: General Purpose Reservoir Simulator with Operator-Based Linearization*. PhD thesis, Delft University of Technology, 2019.
- [64] Mojdeh Delshad, Kazuhiro Asakawa, Gary A Pope, Kamy Sepehrnoori, et al. Simulations of chemical and microbial enhanced oil recovery methods. In *SPE/DOE improved oil recovery symposium*. Society of Petroleum Engineers, 2002.
- [65] Taisa Beatriz Pacheco, António Fábio Carvalho da Silva, and Clovis R Maliska. Comparison of impes, sequential, and fully implicit formulations for two-phase flow in porous media with

